Observed Convective and Moist Dynamics in Extratropical and Tropical Synoptic-scale Circulation during Boreal Summer

by

Haochang Luo

A dissertation submitted in partial fulfillment
of the requirements for the degree of
Doctor of Philosophy
(Climate and Space Sciences and Engineering)
in the University of Michigan
2024

Doctoral Committee:

Assistant Professor Ángel F. Adames-Corraliza, University of Wisconsin, Co-Chair
Professor Richard B. Rood, Co-Chair
Professor Brian K. Arbic
Professor Christiane Jablonowski

Haochang Luo

hcluo@umich.edu

ORCID iD: 0009-0003-2872-115X

Dedication

To the unknown.

Acknowledgements

Up to this moment, my mind has been storming by the gratefulness to those who helped make this thesis possible, turning my goals into reality. Throughout my graduate school, many people have been supporting me against the hardships and obstacles of life. Among them, I would like to give my deepest gratitude to my mentors/advisors, Professors Richard B. Rood and Ángel F. Adames-Corraliza, who have been guiding me and inputting their wisdom during the past five years. Their patience, knowledge and encouragement, their ways of doing science, have tremendous impacts on shaping me into a qualified scholar. It was a great honor to learn and work under their supervision. Special thanks are given to our funding source: the National Science Foundation and the University of Michigan. And providers of GPCP and ERA5 data.

I would also like to acknowledge my research group for creating a friendly and supportive environment. Rosa, Victor, Chelsea, Kayleen, Qiao-Jun, Becca, you are the best group of people I've ever met. Thank you for all the good memories we created and the help you provided. It is my fortune to be friends with you.

Also, I give my thanks to friends outside our group, Chongxing Fan, Vijit, Yifan Guan, Daiya Chen, Qing Niu, Nuo Chen, Ruby and Karimar, who also helped me a lot in my journey. I also would like to appreciate the faculty and staff members in CLaSP (UMichigan) and AOS (UWisconsin) departments, especially Dr. Mayra Oyola-Merced, Dr. Hannah Zanowski, Claire Miller and Pete Pokrandt, who provided either technical or emotional support in the best of their professions.

Most importantly, I want to thank my family, for the 27 years of unwavering support. Your love is always kept in my heart. My grandfather, granduncle and grandaunt, who passed away in the past five years will always be remembered.

I want to give my special thanks to my partner, Youjun, for her commitment to this long-distance relationship. I don't know what is waiting for us ahead but thank you for showing up in my life. Meeting you is the best thing I've ever dreamt of.

Lastly, I would like to thank myself for making choices that I never regret.

Table of Contents

List of Figures

List of Constants and Variables

Names	Descriptions	Values/Units
A	Moisture mode activity	$J \cdot m^{-1}$
a	Radius of Earth	6371 km
c	Phase speed of free gravity wave	$\sim 50\ m \cdot s^{-1}$
C_b	Horizontal barotropic energy conversion	$W \cdot kg^{-1}$
C_{bv}	Vertical barotropic energy conversion	$W \cdot kg^{-1}$
C_p	Specific heat capacity of dry air under constant pressure	$1004\ J \cdot K^{-1} kg^{-1}$
c_p	Phase speed of a wave	$m \cdot s^{-1}$
E	Mean total evaporation rate	$mm \cdot day^{-1}$
f	Coriolis parameter/planetary vorticity	$\sim 10^{-4}\ s^{-1}$
g	Gravitational acceleration	$9.8\ m \cdot s^{-2}$
J	Diabatic heating rate	$W \cdot kg^{-1}$
K	Kinetic energy	$J \cdot kg^{-1}$
K_s	Stationary wavenumber	$-$
L	Horizontal scale of a system	m
L_H	Half-width of the MLPS activity region	m
L_v	Specific latent heat of vaporization	$2.5 \times 10^6\ J \cdot kg^{-1}$
LW	Longwave radiation flux	$W \cdot m^{-2}$

m	Moist static energy	$J \cdot kg^{-1}$
P	Mean total precipitation rate	$mm \cdot day^{-1}$
p	Pressure	Pa
Q_1	Diabatic heating rate	$W \cdot kg^{-1}$
Q_r	Radiative heating rate	$W \cdot kg^{-1}$
q	Specific humidity	$\mathrm{kg} \cdot kg^{-1}$
R_o	Rossby number	$-$
SH	Surface sensible heat flux	$W \cdot m^{-2}$
SW	Shortwave radiation flux	$W \cdot m^{-2}$
s	Dry static energy	$J \cdot kg^{-1}$
T	Temperature	K
U	Zonal wind speed scale	$m \cdot s^{-1}$
u	Zonal wind speed	$m \cdot s^{-1}$
v	Meridional wind speed	$m \cdot s^{-1}$
v	Horizontal wind speed	$m \cdot s^{-1}$
z	Geopotential height	gpm
β	Meridional gradient of planetary vorticity	$2 \times 10^{-11}\ m^{-1}s^{-1}$
τ_c	Convective moisture adjustment time scale	hrs
τ_D	Time scale of adjustment to quasi-equilibrium	hrs
τ_g	gravity wave adjustment time scale / WTG adjustment time scale	hrs
τ_ω	Temporal time scale of a wave	hrs
Φ	Geopotential	$J \cdot kg^{-1}$

φ	Latitude	∘
Ω	Earth rotation rate	$0.73 \times 10^{-4}\ s^{-1}$
ω	Vertical velocity	$Pa \cdot s^{-1}$

List of Acronyms

Abbreviations	Full names
ALE	Available latent energy
avg	average
BH	Bermuda High
BHI	Bermuda High index
BOB	Bay of Bengal
DSE	Dry static energy
ECMWF	European Centre for Medium-Range Weather Forecasts
ENSO	El-Nino Southern Oscillation
EOF	Empirical orthogonal function
ERA5	Fifth reanalysis product from the ECMWF
GPCP	Global Precipitation Climatology Project
ITCZ	Inter Tropical Convergence Zone
JA	July and August
JJAS	June, July, August and September
MCA	Maximum covariance analysis
MJO	Madden-Julian Oscillation
MLPS	Monsoon low pressure system
MSE	Moist static energy
MVI	Moisture-vortex instability

NASH	North Atlantic Subtropical High
PC	Principal component
PKE	Perturbation kinetic energy
QG	Quasi-geostrophic
res	residual
SEUS	Southeastern US
SLP	Sea-level pressure
std	Standard deviation
WTG	Weak-temperature gradient

Abstract

This dissertation focuses on the propagation and growth of tropical and extratropical waves during boreal summer by incorporating views based on vorticity and moisture. They are applied to two different synoptic-scale systems that are located in the mid-latitudes and tropics.

The first case is the Bermuda High (BH). Its expansion and contraction can be quantified by a Bermuda High Index (BHI). The composites of precipitation based on the phase of BHI show an enhanced (suppressed) rainfall over the southeastern US (SEUS) when BH contracts (expands).

Linear regressions of anomalous geopotential height and winds at 200 hPa onto BHI show an eastward-propagating Rossby wave train over the North Hemisphere, with the mid-latitude jet stream being its waveguide. Anomalous troughing over the SEUS associated with this wave train is linked to the contraction of the Bermuda High during July and August. The enhanced precipitation is associated with anomalous ascent to the east and south of this trough where anomalous warm advection is observed. Based on these results, it is hypothesized that this Rossby wave train may partially explain the occurrence of suppressed precipitation tied to midsummer drought in the SEUS.

Tropical systems differ from the ones in the mid-latitudes and subtropics because of the high concentration of moisture and weak temperature tendency. The second case focuses on the tropical Indian Ocean.

The Indian summer monsoon low pressure systems (MLPSs), as one of the most vigorous systems over the Indian Ocean, have been studied comprehensively over the past decades.

However, the dynamics that control the westward movement and growth of the MLPSs remain controversial.

According to the analysis of the column-integrated moist static energy (MSE) and perturbation kinetic energy (PKE) budgets, we propose that the MLPSs grow from the moisture-vortex instability (MVI) and barotropic instability. MVI also contribute to the wave propagation. MVI refers to a process in which the strong horizontal MSE advection leads to a moisture tendency. The vortex grows through the enhanced convection brought about by the moisture tendency. The results show a vertically upright structure and, the moisture, precipitation and vorticity have an in-phase component. The meridional mean MSE advected by anomalous winds is the main contributor to anomalous MSE growth and propagation. The tendency and maintenance of PKE are led by the barotropic energy conversion.

The moisture in MLPSs plays a central role in their energetics. We used three criteria and a dimensionless number (N_{mode}) to measure the importance of moisture: if (i) the precipitation anomalies and the column water vapor anomalies are highly correlated; (ii) the weak-temperature gradient (WTG) is satisfied; (iii) the latent heat is dominating MSE. The results show that all three criteria were satisfied and $N_{mode} \ll 1$ for MLPSs over the tropical oceans. The "moisture mode" governs the thermodynamics of MLPSs.

Using reanalysis products, we examined the moisture mode activity and the meridional eddy moisture flux of MLPSs when they grow from MVI. The available latent energy (ALE) of the Indian monsoon was also calculated. The results show that the meridional eddy moisture flux equals to the tendency of moisture mode activity. The tendency of ALE is coherent with the inverse of meridional eddy moisture flux. The results indicate that the Indian monsoon is weakened through the equatorward eddy moisture flux when MLPSs grow from MVI.

Chapter 1 Introduction

Observation, theory and modeling have been shaping our science for centuries. The observations of the atmosphere can be traced back to millions of years ago when our ancestors were inspired to use fire when a lightning struck a tree. Thousands of years ago, in the east, China, people formulated a lunisolar calendar based on the position of the sun and the moon. The 24 solar terms, also known as the 24 Jie-Qi, were then invented. As a guide to agricultural production, their names are explicit[1]: Beginning of Spring, Rain Water, Awakening of Insects, Spring Equinox, Pure Brightness, Grain Rain, Beginning of Summer, Grain Buds, Grain in Ear, Summer Solstice, Minor Heat, Major Heat, Beginning of Autumn, End of Heat, White Dew, Autumn Equinox, Cold Dew, Frost's Descent, Beginning of Winter, Minor Snow, Major Snow, Winter Solstice, Minor Cold and Major Cold. It is worth noting that the temperature and precipitation occur most frequently in their names as they are directly related to the timing of seeding, reaping and irrigation as well as the other activities. The modern-day atmospheric discovery started with the measurement of the pressure, however. With the creation of a glass of column mercury, people in Europe were able to measure the air pressure. The thirst of knowledge and exploration was not stranded at the bottom of the atmosphere, the balloons were then utilized to detect the vertical profile of temperature and pressure, even the stratosphere. With the development of radio and electromagnetic technologies during the past two centuries, we entered the era of remote sensing, and we were able to view the full picture: the global general circulation. Nowadays, enormous data from radars and satellites are reshaping our cognition of the atmosphere by observing every corner

[1] source: official opening ceremony of Beijing Winter Olympic Games 2022

of our Earth. However, if we want to know tomorrow's temperature, observations alone are far from enough.

How to predict the future? That is the question for everyone who works in the field and the ultimate goal for all our work. And that is when the other two essences of science come into play. Before the concept of general circulation, Edmund Halley summarized the findings of the trade winds and proposed that solar radiation provides energy for atmospheric motion, which later laid a foundation for George Hadley's general circulation model. Hadley's model not only denoted that the air rises at the equator and descends at the poles, but also introduced the friction and the prototype of the east-west branch of the Coriolis force. Hadley's simple model was then compared with the observations and proved to be incorrect at the mid-latitudes. Ferrel then amended the model by incorporating centrifugal force and the north-south branch of Coriolis force (Lorenz 1983). After that, with the overall development in fluid dynamics and thermodynamics, more complicated models were proposed and compared with observations. Such iteration lasted for centuries until World War II. The modern development of atmospheric science was pushed forward by the need for more precise weather prediction, especially for battlefields. Following Newton's laws of motion, we now had a set of equations picturing the momentum of the air by combining the pressure and winds. When fusing the law of thermodynamics, the gas law and the continuity equation, a basic model of our atmosphere can be obtained. Solving the model, however, was never an easy task. Although the idea of numeric weather prediction was brought about in the early 1900s, it was until the end of World War II that Jule Charney, Klara Dan von Neumann and their team were able to calculate the equations by a digital computer. Nowadays, atmospheric research is becoming more like a data-based science. With the help of massive observational and modeling data, scientists can loop efficiently between theory and experiments.

As we mentioned above, the first ever general circulation model was proposed by Hadley in the 1730s, but too rough as in its nature. Our latest view is to analyze the attributes of the atmosphere through statistics in four dimensions: three in space and one in time. In this thesis, we will see the distinctions between the mid-latitudes and tropics, transient eddies and climatological mean flow, zonal variations and zonal averages, high levels and low levels.

1.1 Contrasting the mid-latitudes and tropics

1.1.1 The boundary of the tropics

The tropics is known as a belt with the equator being its center. The definition of its south and north borders, however, varies with the purpose of research (Laing and Evans 2011):

1) $23.5°N/S$ are used due to that the angle of insolation declination can be 90° in this belt.
2) $35°\sim40°N/S$ are used as the region has a net radiation income.
3) $30°N/S$ are used because they are the borders of the descending branch of Hadley Cell. And they are the boundaries of the region in which the mean winds near the surface are easterlies except for monsoons.
4) The tropics can also be defined as the region that has a larger daily temperature range than the annual range.
5) The region that has larger rainfall variability than temperature variability is used as the definition of the tropics.

In this thesis, we generally take $30°N/S$ as the boundaries since the circulation, temperature, moisture and precipitation conditions are the most distinctive in and out of the belt.

There are a variety of differences between the tropics and mid-latitudes. Here we only discuss the ones that are most related to our research.

1.1.2 Coriolis force

People had a hard time explaining why a moving object always tends to deviate from its original track in a rotating system before the definition of Coriolis force. Rather than being a cylinder rotating around its axis, Earth is a sphere, which means the distance from the surface to the axis changes with latitude. The Coriolis parameter, also called as the planetary vorticity was used to depict the effect of rotation from Earth. The parameter changes with latitude:

$$f = 2\Omega sin\varphi, \tag{1.1}$$

where Ω is the rotating speed and φ is the latitude. So the first difference between the mid-latitude and the tropics is that the rotation of the earth has greater impact to the systems in the mid-latitude than in the tropics. However, Coriolis force is not always important, especially for a fast but small object. Here we use the Rossby number to show the relative magnitude of Coriolis force:

$$Ro = \frac{U}{fL}, \tag{1.2}$$

where U is the average velocity of the object and L is the scale of the object. Only when $Ro \ll 1$ the Coriolis effect will be dominant. In this thesis, our targets are slowly propagating synoptic-scale systems, which means they are under the modulation of Coriolis force.

In the mid-latitudes, a wavy flow is usually found, with a wavenumber of 4 to 7. The wave is referred to as the Rossby wave, caused by the rotation of Earth. A special case of the Rossby wave will be introduced in Chapter 2.

In the tropics, the Coriolis effect vanishes at the equator and changes sign in the southern hemisphere. It is natural to expect it to have less effect on many of the tropic systems. However, this is not always the case. Slow and large systems can still be affected since their Ro could be small, once they are larger than the Rossby radius of deformation. Examples are the equatorial waves. They are trapped along the equator, due to the high poleward increasing rate of the Coriolis force. They are restored by the Coriolis force because of potential vorticity conservation, such as the equatorial Rossby wave. Or the Coriolis effect in the northern hemisphere needs to be in balance with the southern hemisphere, such as the equatorial Kelvin wave. Another example of the Coriolis effect in the tropics is the formation of the intertropical convergence zone (ITCZ). The northerlies in the northern hemisphere and southerlies in the southern hemisphere at the bottom of the Hadley Cell are deviated to the west, and then converge at the equator. Also, systems that have large meridional scales can be distorted, such as trade winds and monsoons where northerlies become northeasterlies and southerlies turn into southwesterlies in the northern hemisphere.

1.1.3 Temperature and moisture

Many people's first impression about the tropics is sunshine, beaches and ocean with a melting temperature and high humidity. Yes, due to the tilt of the rotation axis, the region in between 23.5°N/S receives more incoming solar radiation than any other place, leading to a relatively high temperature income. Besides the meridional temperature advection to higher latitudes is not as efficient as zonal advection, leading to a concentration of energy in the tropics. Also, most of the tropical surface is covered by the ocean, leading to a higher capacity of heat. Another feature that can be observed from Fig. 1.1a is that the climatological mean temperature gradient in the tropics is weaker than in the mid-latitudes. The term "weak-temperature gradient"

(WTG) was developed to describe such a scenario (Sobel et al. 2001), it will be discussed in Chapter 4.

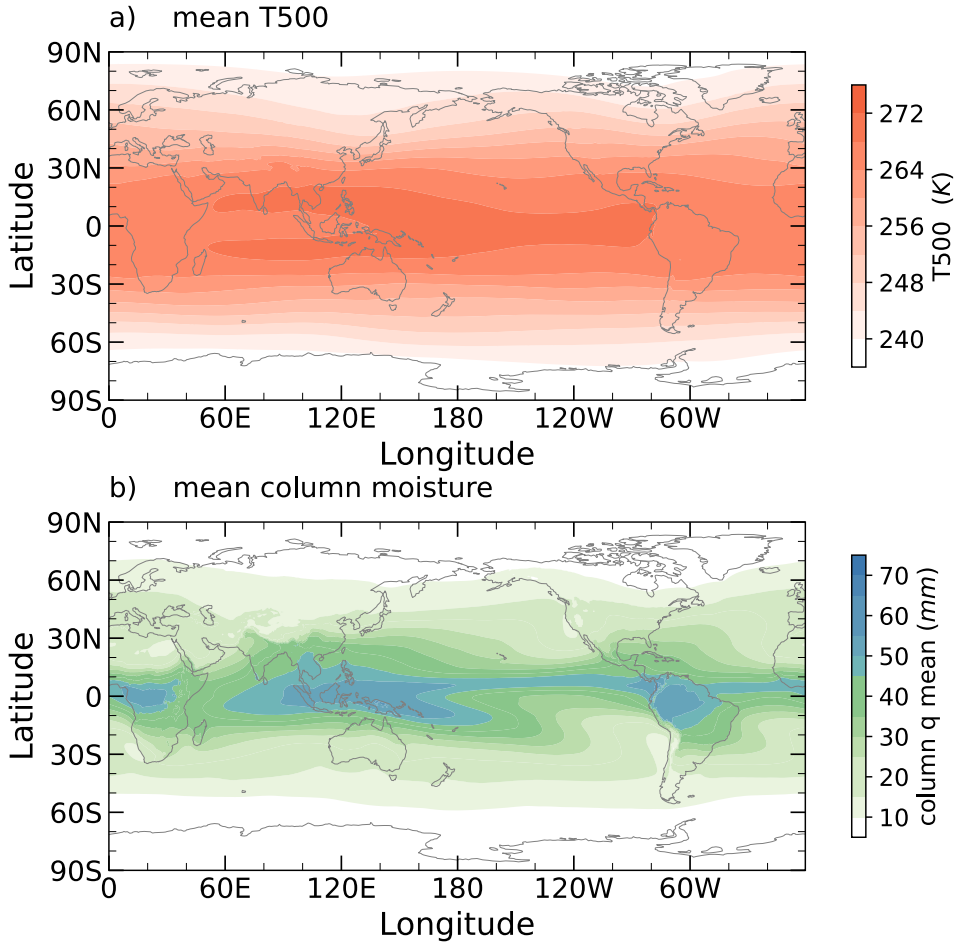

FIG. 1.1 Climatological mean temperature(a) and column integrated water vapor (b).

Different from a homogenized temperature pattern, the moisture condition in the tropics is more variant, especially near the ITCZ. Compared to the mid-latitudes, the high concentration of water vapor in the tropics could release a higher amount of latent heat thus becoming a source of energy to disturbances. The tropics could give birth to the systems that the latent energy is dominant in their thermodynamics, known as the “moisture mode” (Neelin and Yu 1994). For such systems, the moisture variations are more significant than temperature variations. They are in the

WTG balance, the diabatic heating is in balance with the adiabatic cooling (Mayta et al. 2022). Also, the precipitation associated with the systems is highly correlated to their column moisture.

1.1.4 Precipitation

Since the tropics are humid, the rate of precipitation is also high when there is convection. Fig. 1.2a shows the climatological mean precipitation rate. Generally, the tropics have a relatively high precipitation relative to the extratropics. The high precipitation in the tropics is colocated with the high column moisture. Fig. 1.2b shows the standard deviation of precipitation. Nearly all the places that have high precipitation rates have strong rainfall variability. Our target areas: the Indian monsoon region and the North America-North Atlantic region (marked by the red box in Fig. 1.2a) both have a vibrant rainfall pattern.

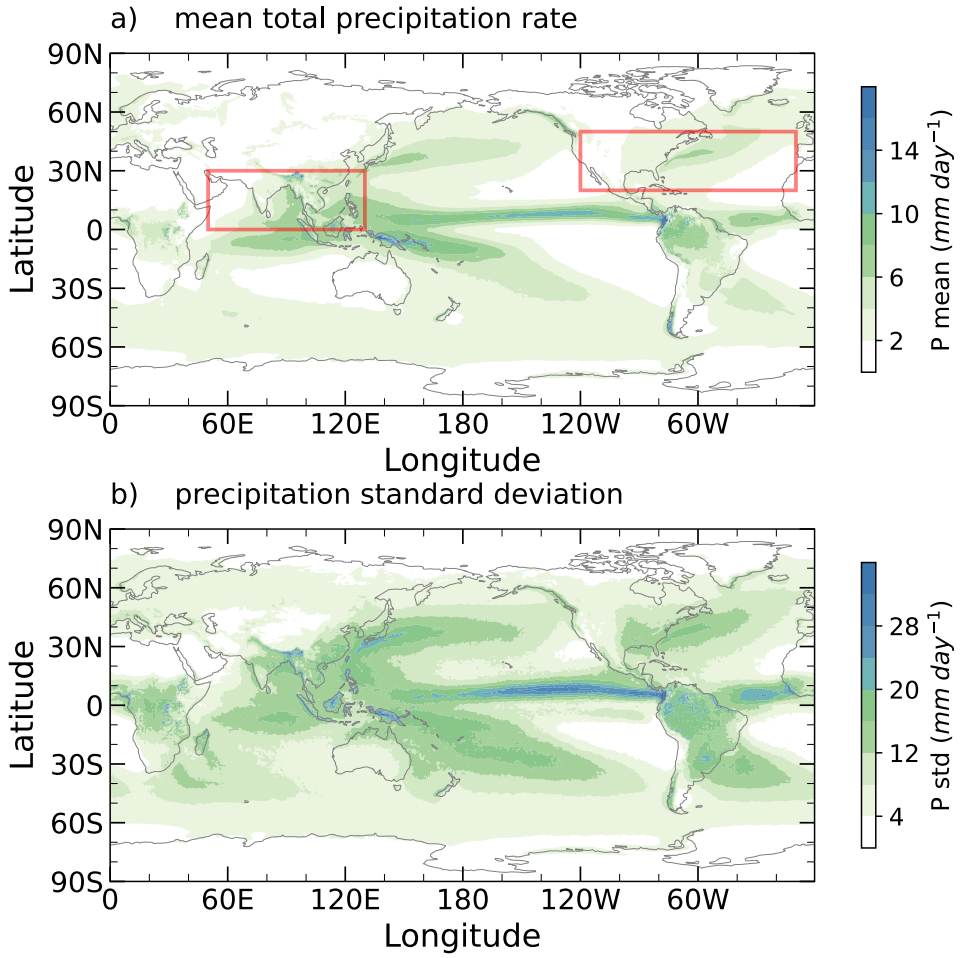

FIG. 1.2 Climatological mean total precipitation rate (a) and precipitation standard deviations (b).

1.1.5 Waves

As mentioned above, the circulation of the atmosphere varies with time, latitude, longitude and height. Once the noise is filtered out, the variations will show up as signals. The signals that repeat in space and time are known as waves. The most commonly seen waves in the extratropical atmosphere are planetary waves, also known as the Rossby wave, caused by the Coriolis effect discussed above. They are usually linked to weather extremes (Francis and Vavrus 2012; Petoukhov et al. 2013; Screen and Simmonds 2014) in temperature and precipitation. The suppressed rainfall in July and August over the southeastern United States and Central America,

known as the midsummer drought, is suggested to have a relation with a Rossby wave in Chapter 2.

Since modern atmospheric research started in the mid-latitudes, observations and theoretical work about the tropics have lagged. The tropics was initially considered as a stable area with tropical cyclone cases occasionally (Riehl 1954). However, the tropics are much more active with a variety of weather systems. Some of them have climate time scale, such as the Indian monsoon, ITCZ and El Nino Southern Oscillation (ENSO). Some of them have synoptic time scales such as Madden-Julian Oscillation (MJO, Madden and Julian 1971), easterly waves (Chang 1970) and monsoon low-pressure systems (Mooley 1973).

1.2 Motivation

The temperature and precipitation, as the most important factors directly related to life and society since ancient times, are the critical points of our study. As two of the less developed areas, Central America and South Asia are plagued by drought and flood. The “abnormals” are becoming the normal for the people living there with climate change. Thus, it is urgent to figure out the connection between the precipitation extremes and the influencing systems, such as the Bermuda High, Rossby Waves and MLPSs. Understanding the mechanism will help to diminish the impact on society and the economy, especially for those agriculture-based countries.

1.3 Outline

The thesis is structured as follows: a Rossby wave train and its connection to the Bermuda High variability and rainfall anomalies over the southeastern US and Central America is discussed

in Chapter 2. The growth and propagation mechanism for Indian monsoon low pressure systems is presented in Chapter 3. Chapter 4 is a study of the wave activity in Indian monsoon low pressure systems. Concluding remarks are in Chapter 5.

1.3.1 Introduction to the Bermuda High and Rossby wave

The North Atlantic Subtropical High is sometimes referred to as the Bermuda High since its center is near Bermuda during boreal summer. The variability of the Bermuda High often impacts the rainfall variability in the surrounding areas such as the southeastern US (Stahle and Cleaveland 1992; Henderson and Vega 1996; Keim 1997) and the Great Plains (Zhu and Liang 2012). The decreased precipitation during July and August near southeastern US and Central America is often referred to as the midsummer drought (Henderson and Vega 1996). The midsummer drought highly impacts the agriculture, hydropower generation and related socio-economic activities (Magaña et al. 1999). The appearance of midsummer drought is related to multiple factors such as El-Nino Southern Oscillation, Pacific-North America pattern, North Atlantic Oscillation and the Bermuda High (Katz et al. 2003). This dissertation focuses specifically on the influence from the Bermuda High during boreal summer. In previous studies, the strength and location of the Bermuda High are strongly connected to the variations in the sea level pressure, trade winds, sea surface temperature and vertical motions thus leading to increased/decreased precipitation (Knaff 1997; Giannini et al. 2000; Small et al. 2007).

The processes that lead to the spatial and temporal evolution of the Bermuda High (BH) during July and August (JA) are investigated in Chapter 2. The Bermuda High could expand westward. Its west edges could reach out into southeastern US, and thus causing anomalous moisture conditions and vertical motions. The expansion and contraction of the Bermuda High are

separated based on a Bermuda High index (BHI). Negative values of BHI indicate a westward expansion of the Bermuda High relative to its climatological-mean location and reduced precipitation in the southeastern United States (SEUS), whereas positive values correspond to BH contraction and enhanced precipitation in the SEUS. Apart from the Bermuda High itself, its connection to the global circulation was also investigated.

Linear regression of the 200-hPa geopotential height based on the BHI reveals the existence of a Rossby wave train that extends zonally from the eastern North Pacific to the eastern North Atlantic. The troughs and ridges associated with this wave train are spatially collocated with the climatological-mean jet stream, indicating that the jet serves as their waveguide. Anomalous troughing in the SEUS associated with this wave train is linked to the contraction of the Bermuda High during JA. The enhanced precipitation is associated with anomalous ascent to the east and south of this trough where anomalous warm advection is observed. Based on these results, it is hypothesized that this Rossby wave train may partially explain the occurrence of suppressed precipitation tied to midsummer drought in the SEUS during July and August. It is found that the BHI has trended from negative to positive in recent decades, suggesting that it may be influenced by low-frequency variability. Through such analysis, the goal of Chapter 2 is to improve the prediction of dry/wet conditions over the target area and lay a foundation to the future study in how the midsummer drought might change in a warming climate.

1.3.2 Introduction to Monsoon low pressure systems

In the global circulation model, the air rises near the equator and descends at the borders of the tropics due to the strong insolation at the equator. The upward and downward motions lead to poleward flow at high troposphere and equatorward flow at low troposphere. Such is the Hadley

flow. The equatorward flow near the surface converges near the equator, forming the Inter-tropical convergence zone. When ITCZ moves northward during boreal summer, its branch over the Indian Ocean moves to the north of Bay of Bengal. That part is also called the monsoon trough. The monsoon trough gives birth to various disturbances. As one of the most prominent weather systems affecting the Indian subcontinent, the Indian summer monsoon low pressure systems (MLPSs) have been studied extensively since they were first documented by Eliot (1884).

However, the processes that govern the growth of the MLPSs are not well understood. After Charney (1947) proposed the protype of barotropic and baroclinic model, scientists started to apply the frameworks to MLPSs since 1970s (Rao and Rajamani 1970; Krishnamurti et al. 1975). The barotropic instability is a horizontal unstable condition. The disturbance must have a tilt against the downgradient zonal wind shear. The baroclinic instability is a vertical unstable condition. Similarly, the disturbance must have a tilt against the downgradient zonal wind shear. It is natural to think MLPSs being powered by baroclinic or barotropic instability since they are the mechanisms in the Indian monsoon. Later, scientists realized the importance of water vapor, and they proposed the moist baroclinic (Krishnakumar et al. 1992) and moist barotropic models. But they are still not the full picture, disagreements showed up as the theories failed to explain the observations. The zonal wind in the Indian monsoon increases from mid troposphere to the surface but the eastward tilt at the top of MLPSs is not seen. So Adames and Ming (2018b) recently proposed the moisture-vortex instability (MVI) as a replacement for baroclinic instability. The MVI is featured by a meridional moisture advection and thus leading to a moisture tendency. The moisture increases and shifts towards the center of the disturbance and enhances the convection. The vortex grows through vortex stretching caused by enhances convection.

To better understand these processes, in Chapter 3, we created an MLPS index using bandpass-filtered precipitation data. Lag regression maps and vertical cross-sections are used to document the distribution of moisture, moist static energy (MSE), geopotential, horizontal and vertical motions in these systems. It is shown that moisture governs the distribution of MSE and is in phase with precipitation, vertical motion, and geopotential during the MLPS cycle. Examination of the MSE budget reveals that longwave radiative heating maintains the MSE anomalies against dissipation from vertical MSE advection. These processes nearly cancel one another, and it is variations in horizontal MSE advection that are found to explain the growth and decay of the MSE anomalies. Horizontal MSE advection contributes to the growth of the MSE anomalies in MLPSs prior to the system attaining a maximum amplitude and contributes to decay thereafter. The horizontal MSE advection is largely due to meridional advection of mean state MSE by the anomalous winds, suggesting that the MSE anomalies undergo a moisture-vortex instability-like growth. In contrast, perturbation kinetic energy (PKE) is generated through barotropic conversion. The structure, propagation, and energetics of the regressed MLPSs are consistent with both barotropic and moisture-vortex growth.

1.3.3 Moist wave activity

In Chapter 3, the moist static energy budget, a combination of dry energy and latent energy, is used to study the thermodynamic characteristics of the monsoon low pressure systems. In Chapter 4, new terminologies are introduced to quantify the role of latent energy. The “moisture mode” criteria are used to define a system that moisture and latent energy dominating its thermodynamics. The “moisture mode activity” is used to show the eddy intensity change during the cycle. It is proportional to the square of eddy column moisture and related to the background

meridional latent energy gradient. The “available latent energy”, as a mirror of moisture mode activity, is to show the means state, the Indian monsoon, intensity variations when the disturbances pass by. The word “available” indicates that this part of latent energy from the means state is ready to be converted to the waves. The sum of moisture mode activity and available latent energy are conserved and their tendency equals to the meridional eddy moisture flux. The coupling of the two quantities revealed and examined our hypothesis that the Indian monsoon is the source of the latent energy that extracted by monsoon low pressure systems when they grow.

1.3.4 Methods

The approaches used in our study are linear regressions and composites. The regressions and composites are based on indices that show the variations of the target systems. In Chapter 2, the index was formulated by the time-varying sea-level pressure difference between two locations, indicating the westward expansion and contraction of the Bermuda High. Dates of the strong positive/negative values in the index were picked out. Variables such as precipitation, winds and geopotential height, on those dates are averaged to produce the composites. In Chapters 3 and 4, the index representing the monsoon low pressure system variations were created through a band-pass filter. Precipitation data was filtered to retain the maximum signal in the synoptic scale over the Indian Ocean. The filtered precipitation was then regional averaged at the head of Bay of Bengal where the genesis of monsoon low pressure systems is the densest. Linear regressions with lags onto the index was used to identify the dynamic features during their propagation, growth and decay.

Chapter 2 A Northern Hemispheric Wave Train Associated with Interannual Variations in the Bermuda High during Boreal Summer

Luo et al. 2021: Published on the Journal of Climate, 34, 6163–6173, https://doi.org/10.1175/JCLI-D-20-0608.1.

2.1 Introduction

The North Atlantic Subtropical High (NASH), also known as the "Bermuda-Azores High", is a region of climatological-mean high pressure centered over the North Atlantic near $32.5°N$, $45°W$. When the NASH is located on the western Atlantic basin during boreal summer, its lower-tropospheric center is located near Bermuda and it is often regarded as the Bermuda High (BH) (Zishka and Smith 1980; Davis et al. 1997; Li et al. 2010). We will use the term "Bermuda High" from here on to denote the western phase of NASH. The BH plays an important role in the climate of southeastern North America. The shape, location and intensity of the BH have been associated with variations in precipitation over the southeastern United States (SEUS) (Stahle and Cleaveland 1992; Henderson and Vega 1996; Keim 1997; Katz et al. 2003; Li et al. 2010; Ortegren et al. 2011) and over the US Great Plains (Zhu and Liang 2012). It also plays a central role in the occurrence and strength of the midsummer drought (Hastenrath 1976, 1978), a local minimum in precipitation that occurs in July and August (JA) over the SEUS, the Major Antilles and part of Central America (Henderson and Vega 1996). An intensified and westward expanded BH brings higher sea level pressure and incites stronger trade winds and lower sea surface temperature (Giannini et al. 2000), along with stronger subsidence (Knaff 1997), resulting in a decrease in precipitation over the

Caribbean region (Small et al. 2007). Gamble et al. (2008) verified these conclusions but pointed out differences in the spatial influence of Bermuda High over the Caribbean region. Instead of initiating the midsummer drought over the whole Caribbean region, the midsummer drought initiates over the eastern Caribbean and proceeds westward, having a different duration over different locations. Kelly and Mapes (2011) argued that a teleconnection pattern that arises from the South Asian monsoon strengthened the BH, causing the midsummer drought in the western North Atlantic. Li et al. (2012) analyzed the relationship between moisture transport and vertical motion associated with displacements of the BH over the SEUS. They found that a southwest displacement of the BH causes increased moisture transport and rainfall whereas water vapor and precipitation decrease when the BH shifts towards the northwest.

The origin of the BH was also investigated in several studies. Using both observational data and a linear quasi-geostrophic model, Chen et al. (2001) revealed that Asian monsoonal heating is the main energy source of the subtropical high. The same conclusions were drawn by Rodwell and Hoskins (2001) through a primitive equation model. Their hypotheses were also supported by Seager et al. (2003), who concluded that summer monsoonal heating over land brings about the development of the subtropical anticyclone. However, these studies found that the subtropical high forced by the Asian monsoon was weak in their models. Miyasaka and Nakamura (2005) proposed that, in addition to the teleconnections with the Asian Summer Monsoon, localized zonal contrasts in near-surface heating between the Atlantic Ocean and cooling near the continental west coast of Africa is the primary driver for the BH.

In this study, we will investigate the mechanisms that modulate the intensity and position of the Bermuda High and the mechanisms by which it modifies precipitation in its adjacent regions. We propose to answer the following questions: 1) Are variations in the BH linked to the rainfall

variations during July and August in the SEUS? 2) If so, what is the mechanism that leads to variations in the BH and the occurrence of the precipitation variations in the midsummer?

This study is structured as follows: Section 2.2 discusses the data and methods employed in this study. Section 2.3 discusses the variability of Bermuda High as well as its relations with precipitation over the SEUS. Section 2.4 investigates the structure of a teleconnection pattern that modulates the Bermuda High. A concluding discussion of this chapter is presented in Section 2.5.

2.2 Data and Methods

We make use of monthly-mean data from the fifth reanalysis from the European Centre for Medium-Range Weather Forecasts (ECMWF) (ERA5, Hersbach et al. 2019). The date covers the period starting in 1979 and ending in 2018. The data has a horizontal resolution of $0.25° \times 0.25°$ and 32 vertical levels ranging from 1000 to 10 hPa. The variables used in this study are geopotential height (z), temperature (T), horizontal and vertical winds (u, v, ω), specific humidity (q), sea-level pressure (SLP) and mean total precipitation rate (P). For comparison, we use monthly precipitation rate data from the Global Precipitation Climatology Project (GPCP) (Adler et al. 2003, 2018), starting from 1979 to 2018. Its spatial resolution is $2.5° \times 2.5°$.

Many of the fields analyzed in this study are anomalies obtained by removing the seasonal cycle and linear trends. The seasonal cycle is removed by subtracting the monthly climatology from each respective month. Linear trends are also removed to avoid contamination with any long-term trends that may not be related to the interannual variations that are of interest to this study.

The position and shape of Bermuda High can be quantified through the use of the Bermuda High Index (BHI) (Stahle and Cleaveland, 1992). The BHI was initially defined as the standardized

SLP northeast of Bermuda (blue dot in Fig. 2.2) minus the standardized SLP over New Orleans (red dot in Fig. 2.2):

$$\mathrm{BHI} = \mathrm{SLP}'(40°\mathrm{N}, 60°\mathrm{W}) - \mathrm{SLP}'(30°\mathrm{N}, 90°\mathrm{W}), \tag{2.1}$$

where SLP' denotes a standardized SLP anomaly field:

$$\mathrm{SLP}' = \frac{\mathrm{SLP} - \mathrm{avg(SLP)}}{\mathrm{std(SLP)}}, \tag{2.2}$$

where std is the standard deviation and avg is the average. The seasonal cycle and linear trends are also removed from the SLP anomalies.

Because we are interested in using the BHI as a time series for linear regression, we will standardize the time series so that an amplitude of 1 corresponds to one standard deviation in the BHI:

$$\mathrm{BHI}' = \frac{\mathrm{BHI}}{\mathrm{std(BHI)}} \tag{2.3}$$

While additional definitions of the BHI exist (, Zhu and Liang 2012), we use the definition described by Eq. (2.1). We have verified that our results are reproducible with alternative definitions of the BHI (not shown).

Most of the results presented in this study are obtained from linear regression analysis based on the BHI. The statistical significance of the regression fields is tested by examining whether the correlation coefficient of each grid point exceeds a critical value. A critical coefficient value is obtained from a Fisher transformed correlation, following the method employed by Chen (1982) and Adames and Wallace (2014). Values that exceed this critical correlation coefficient are significant at the 95% confidence interval. To obtain the critical coefficient, we first, calculate the effective number of degrees of freedom discussed by Davis (1976) and Chen (1982). The effective number of degrees of freedom is calculated through the decorrelation time scale (Adames and

Wallace 2014), which is the sum of multiplied autocorrelations over all time lags for each individual grid point. One of the autocorrelations comes from the BHI and the other one is from the time series of a variable field (for example, precipitation anomalies). With the effective number of degrees of freedom on each grid, the critical coefficient can be calculated through the method presented by Adames and Wallace (2014). A grid point will be deemed significant if its cross correlation's absolute value is higher than the largest absolute value of critical coefficient in the domain.

We also use empirical orthogonal functions (EOF or principal component analysis) on the regional precipitation field. The EOF's time series, also called principal components (PC) are adopted to make regressions and comparisons with the BHI. Similar to EOF analysis, maximum covariance analysis (MCA) (Bretherton et al. 1992; Newman and Sardeshmukh 1995; Cherry 1996; Hu 1997) is also implemented in a joint field of precipitation and geopotential height at the 1000 hPa level. The result of MCA is also shown in the Appendix (Fig. 2.11). To test if the EOFs are statistically distinguishable from one another, we use North et al.'s (1982) method to determine the confidence interval of the eigenvalue of the EOF/MCA analysis. The EOF and MCA patterns shown here were found to be statistically significant at the 95% confidence interval. As shown in the Appendix, the second leading pattern of variability in both analyses is highly correlated with the BHI (Figs. 2.10a and 2.11, respectively).

Some additional plots are obtained from compositing. These composites represent strong Bermuda High contraction (BHI+) and expansion (BHI-) events, defined as the times when the BHI exceeds 1 standard deviation or –1 standard deviation, respectively.

2.3 Variability in the Bermuda High during July and August

Figure 2.1a shows the time series of the BHI from 1979 to 2018. Figure 2.2 shows composites based on the months in which the BHI exhibited an amplitude greater than unity. As seen in Fig. 2.2, in years in which the BHI is positive, the Bermuda High remains over the ocean, and contracts relative to its climatological position (Fig. 2.2a). In years which it is negative, the BHI expands westward into North America, relative to its climatological position (contours in Fig. 2.2b). The index exhibits an amplitude greater than 1 in 07/1979, 07/1984, 07/1985, 08/1988, 07/1994, 07/2004, 08/2005, 07/2007, 07/2008, 08/2012, 07/2013, 07/2014 and 07/2018. It exhibits an amplitude of less than -1 during 08/1980, 07/1983, 07/1986, 1987, 07/1992, 07/1993, 07/1999, 07/2002, 07/2012, 07/2015, 07/2016 and 08/2018. The BHI is skewed: both strong positive and negative Julys outnumber the Augusts. This result indicates that the BH is more variable during July that during August. In spite of this variability, the large-scale patterns associated with fluctuations in the BH are similar during both months (not shown). Also, even the BHI is calculated from detrended data, there is a multi-decadal trend. Before 2003, the BHI has more strong negatives while tends to be strong positive since then. This trend indicates a shift of BH from mainly expansion to contraction in the recent two decades.

Figures 2.1b and c show JA precipitation from ERA5 and GPCP respectively, averaged over the SEUS (23-35°N, 75-95°W, marked by red box in Fig. 2.2). The months that the BHI is positive are dotted in red and the negatives are in blue. Dry conditions are more likely to happen over the SEUS when the BHI is negative, which is consistent with previous studies (Henderson and Vega 1996; Zhu and Liang 2012). The correlation coefficient of ERA5 precipitation time series with BHI is 0.68 and 0.66 for GPCP. Figure 2.1d shows a scatterplot of the BHI and rainfall

anomalies over the SEUS. The clustering of the cloud of points in Figure 2.1d suggests a roughly linear relationship between the BHI and rainfall in the SEUS.

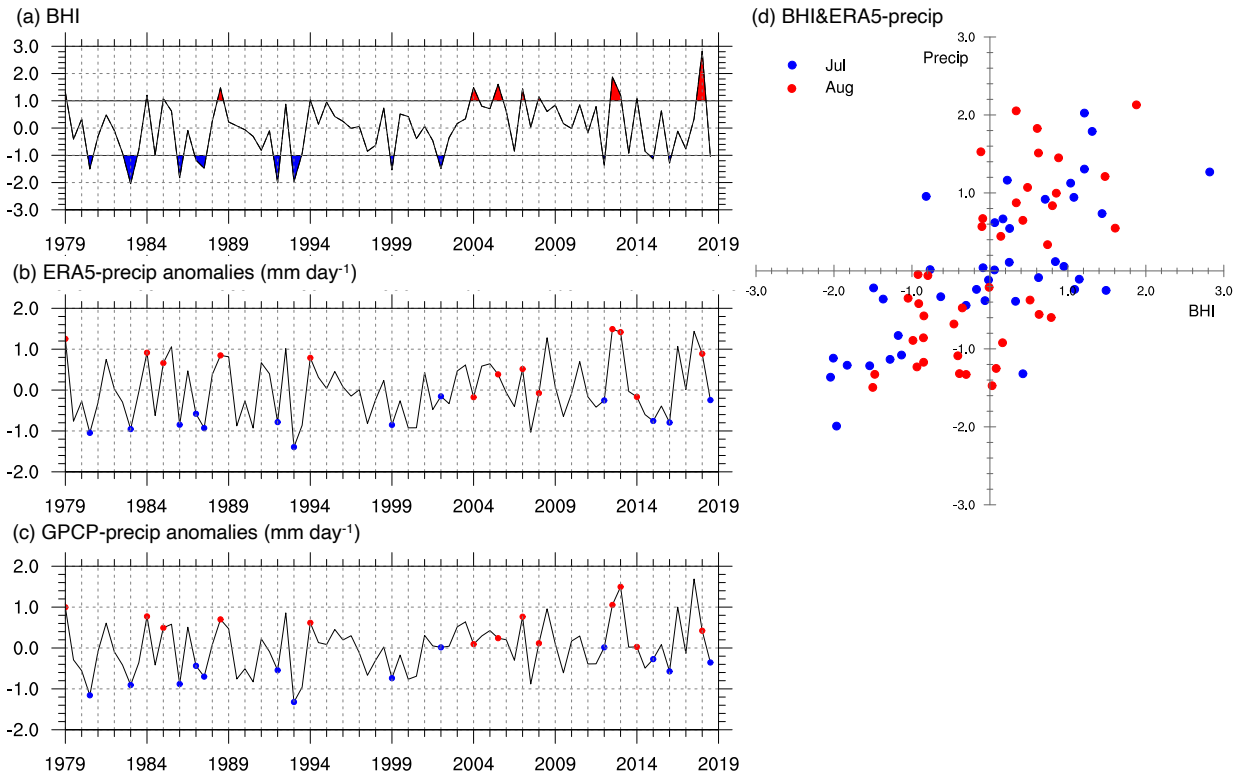

FIG. 2.1. (a) Time series of the standardized BHI in July and August (JA) from 1979 to 2018, defined following Eq. (2.1). The red spikes denote a BHI amplitude greater than 1 std and the blue ones an amplitude less than -1 std. (b) Deseasonalized and detrended precipitation (mm day^{-1}) from ERA5 averaged over the SEUS (23-35°N, 75-95°W red box in Fig. 2.2. (c) As in panel (b) but showing GPCP precipitation data. The dots in panels (b) and (c) are as in the spikes in panel (a), showing the months of strong BHI. (d) Scatterplot of standardized BHI and ERA5 precipitation anomalies. July is marked by blue dots and August is marked by red.

The shading in Fig. 2.2 (a,b,c,d) shows the interannual variation of precipitation in strong positive (a, c) and strong negative (b, d) BHI phases. The contour lines show the area of the BH. During the positive years, a region of mean rainfall greater than 6 mm day^{-1} is observed over the SEUS following the northwestern edge of Bermuda High. Consistent with Fig. 2.1b, during negative years the precipitation in SEUS decreases. In agreement with previous findings, the westward extension of the Bermuda High is correlated with suppressed rainfall (Giannini et al.

2000; Small et al. 2007; Gamble et al. 2008). When the BH is in the negative phase, rainfall is suppressed along with the western edge of BH (Kelly et al. 2018). The horizontal distribution and magnitude of precipitation are similar in ERA5 and GPCP data. Minor differences show up in the SEUS, however. For example, the ERA5 data exhibits less rainfall over Florida in the positive phase.

The distribution of column-integrated specific humidity ($\langle q \rangle$) is shown in Fig. 2.2e and f. The overall patterns are similar, except that during positive BHI months (Fig. 2.2e), higher concentrations of humidity are observed over Florida, while during negative BHI months higher values of $\langle q \rangle$) are observed in the US great plains.

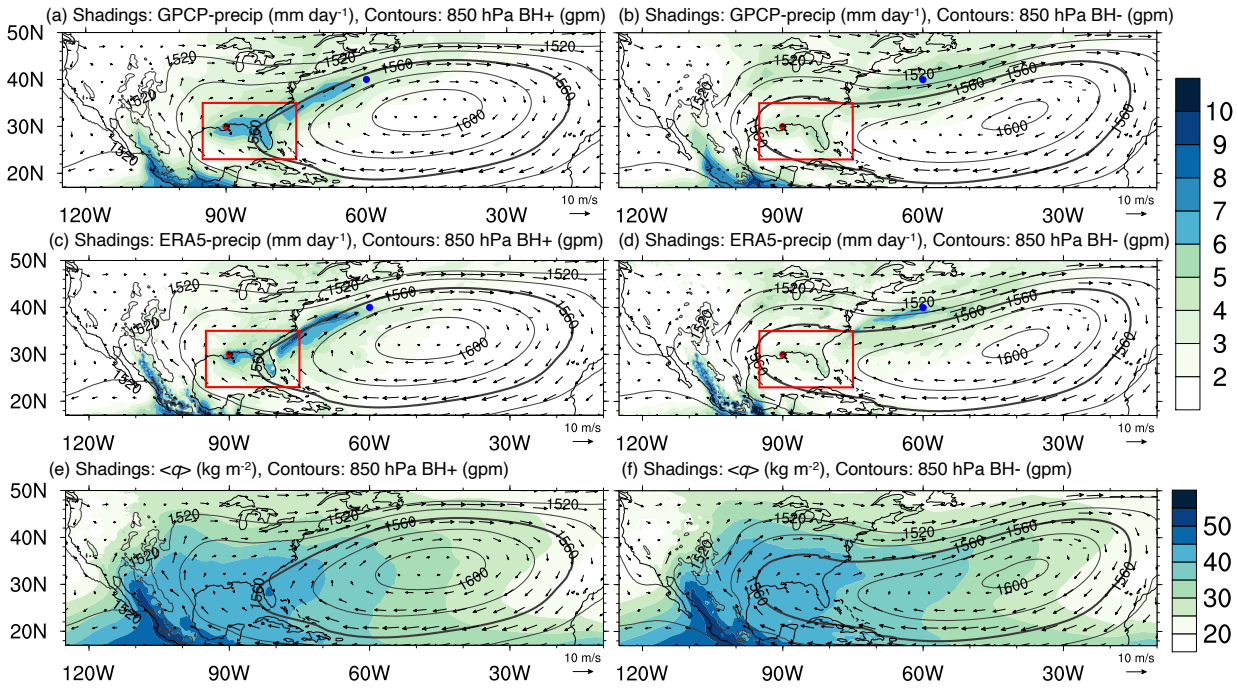

FIG. 2.2. (a): JA composite maps of 850 hPa geopotential heights (contours, in units of gpm), corresponding horizontal wind (vectors, in unites of m s^{-1}) and GPCP precipitation (shading) for BHI exceeding 1 std (left) and -1 std (right). 1560 gpm, which is considered the edge of the Bermuda High (Li et al. 2010) is shown as a thick line. (c, d) and (e, f) are as in (a, b) but showing ERA5 precipitation and column-integrated specific humidity ($\langle q \rangle$, in units of kg m^{-2}), respectively. The SEUS region is shown as a red box in the top four panels. The locations used to calculate BHI are marked by red ($30°N$ $90°W$) and blue dots ($40°N$ $60°W$).

Figure 2.3a shows linear regressions of 850 hPa geopotential height and precipitation onto BHI. As described in Section 2.2, the fields are anomalies obtained by removing the mean and seasonal cycle from the data. An anomalous anticyclone is seen over the northwestern Atlantic and an anomalous cyclone is seen over SEUS and Gulf of Mexico. Colocated with the anomalous cyclone is a region of enhanced precipitation. Suppressed precipitation is seen near the northwestern Atlantic anticyclone. Apart from the two strong centers, another cyclone is seen in the northeastern Atlantic. No significant precipitation anomalies are seen near this cyclone.

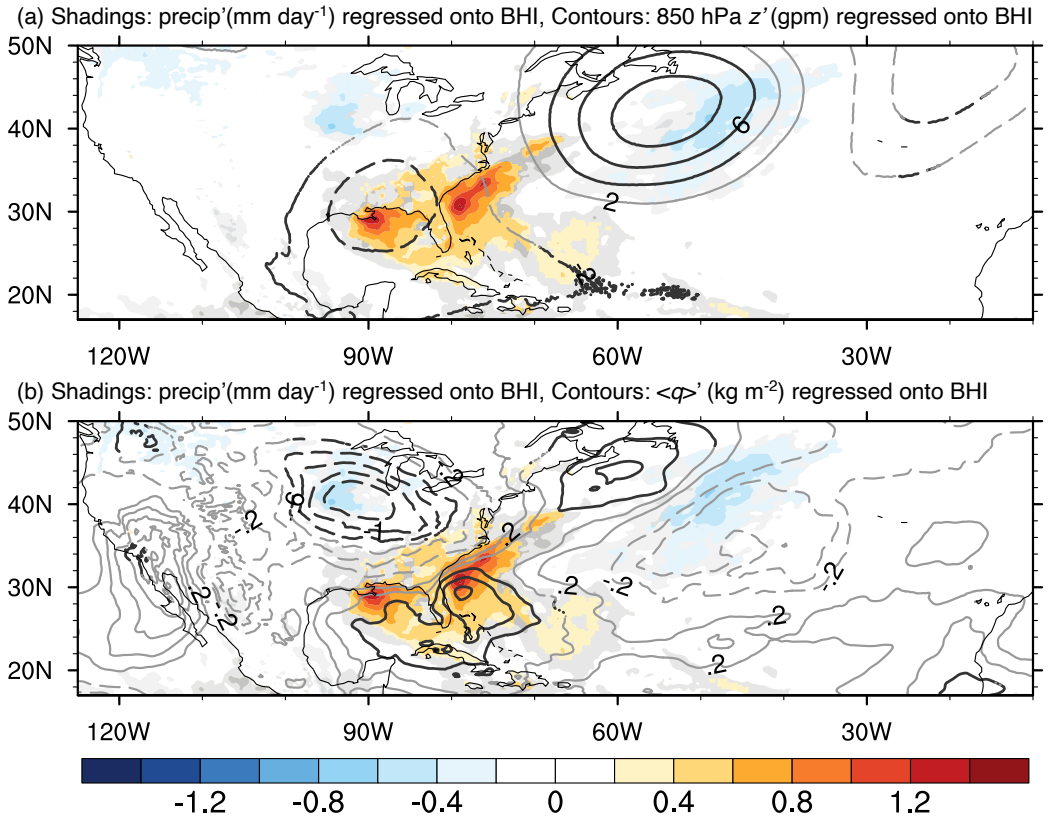

FIG. 2.3. (a): Linear regression of 850 hPa geopotential height anomalies (contours, with an interval of 2 gpm) and ERA5 precipitation rate anomalies (shading, in units of mm day^{-1}) onto the BHI. (b): As in (a) but showing column-integrated specific humidity anomalies. Contour interval of 0.2 kg m^{-2}. The black contours and blue/red shading are significant at the 95% confidence interval.

Figure 2.3b shows the distribution of anomalous precipitation along with the anomalies in column-integrated specific humidity. The moisture anomalies are located at the edges of the

anomalous cyclone and anticyclone shown in Fig. 2.3a. Anomalously humid conditions are seen at the equatorward component of the cyclone, while the reverse conditions are seen in the poleward side. To first order, the regions of enhanced precipitation correspond to the regions of increased water vapor and the suppressed rainfall corresponds to reduced water vapor. However, the precipitation anomalies are shifted to the north of the water vapor anomalies over SEUS.

2.4 Northern Hemisphere wave train

The regression maps of anomalous geopotential height (contours) and precipitation (shadings) in Fig. 2.3a show a horizontal structure suggestive of a large-scale wave train in the Northern Hemisphere. To investigate this idea further, we examine longitude-height cross sections of geopotential height and vertical velocity averaged over the 40°-50°N latitude band (Fig. 2.4). We chose this band because most of the troughs and ridges of the wave, especially the anticyclone that is closely related to the BH over the North Atlantic, are located within this band (refer to Fig. 2.5). This cross section reveals a wave train, with alternating regions of high and low geopotential heights that encompass most of the western hemisphere. The vertical wind anomalies are located in the regions where the horizontal gradients in geopotential height are strongest, suggestive of quasi-geostrophic forcing as indicated by the omega equation (Holton and Hakim 2013a). We can qualitatively express the omega equation for this cross section as:

$$\omega \propto \frac{\partial \mathbf{v}}{\partial p} \cdot \boldsymbol{\nabla}_h \Phi, \tag{2.4}$$

where ω is the vertical velocity in isobaric coordinates, $\Phi = gz$ is geopotential and p is pressure. Equation (2.4) indicates that when $\frac{\partial u}{\partial p} < 0$, which is typical for the midlatitudes, ascent occurs in regions where the geopotential is increasing with longitude and descent occurs in regions where

the geopotential decreases with longitude. This type of pattern is clearly seen throughout the western hemisphere (180°- 0°) in Fig. 2.4.

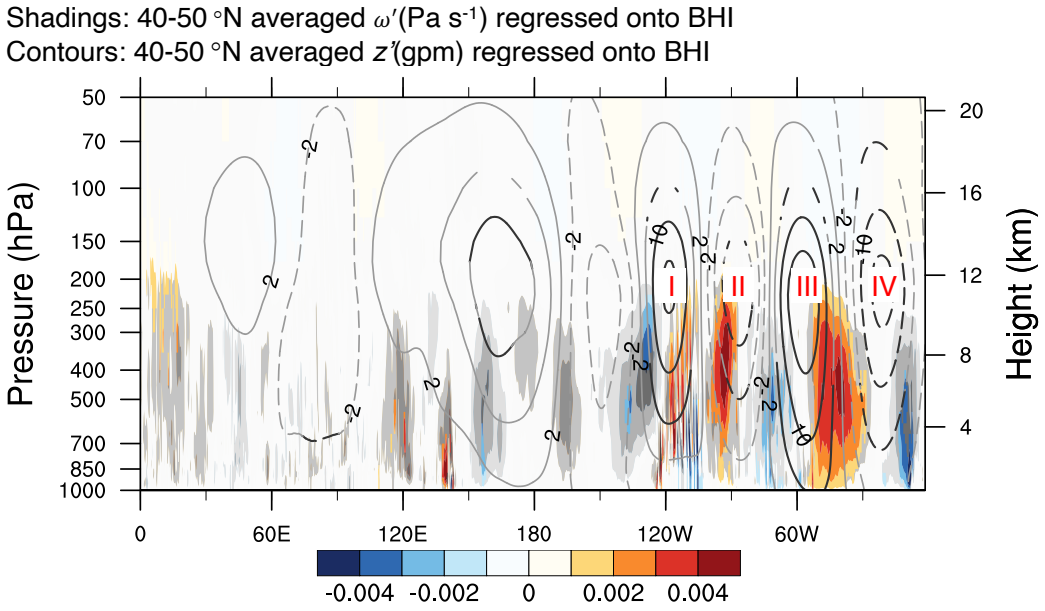

FIG. 2.4. Vertical cross section of 40-50°N averaged geopotential height anomalies (contour interval is 4 gpm, beginning at 2 and -2 gpm, respectively) and vertical velocity anomalies (shaded, in units of Pa s^{-1}) regressed on to the BHI. The black contours and blue/red shading are significant at the 95% confidence interval.

The results from Fig. 2.4 reveal the existence of a wave train that may affect the position and amplitude of the Bermuda High. Its strongest variations are located near 200 hPa. Such wave trains are usually guided by the midlatitude jet stream (Wirth et al. 2018). In order to verify this idea, Fig. 2.5 shows the geopotential height anomalies regressed onto the BHI and the JA-mean jet stream at 200 hPa. From 120°W to 0°, near the 40°N-50°N band where the jet is strong, four clearly-defined, statistically significant ridges and troughs are observed following the region of maximum westerly winds over the Atlantic and North America region. Such a pattern indicates that the westerly jet acts as a waveguide for this pattern (Branstator 1983). In addition to these four centers, there is a hint of a statistically-significant signal over the Pacific Ocean. Most of the centers are nearly collocated with the lower tropospheric geopotential height signatures seen in

Fig. 2.3a, indicative of an equivalent barotropic structure. For the centers over SEUS and North Atlantic, a small northwestward tilt in height is seen in the geopotential, as hinted by Figs 2.4 and 2.5.

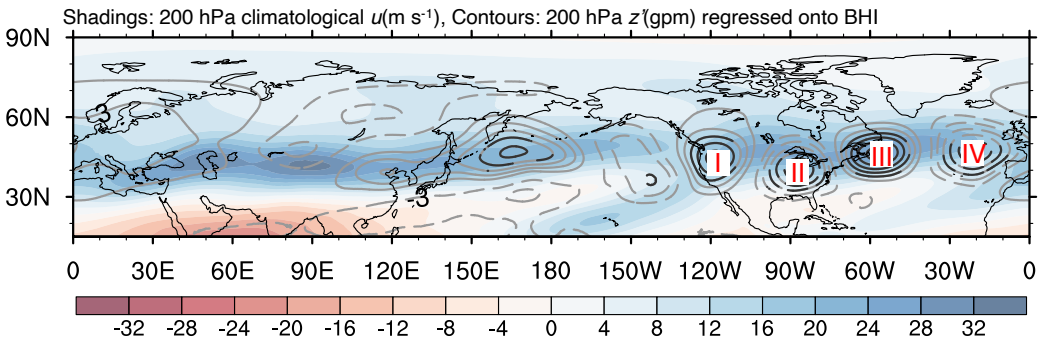

FIG. 2.5. 200 hPa geopotential height anomalies (contour) regressed onto the BHI. The black contours are significant values at the 95% level. The contour interval is 3 gpm. The shading depicts the 200 hPa JA-mean zonal wind in units of m s^{-1}.

Spectral analysis of the 200 hPa height anomalies reveals that the wave train exhibits a horizontal scale between zonal wavenumber 6-7 (Fig. 2.6), which corresponds to a wavelength of 3000-3500 km. Previous research has shown that Rossby wave trains with a zonal wavenumber ~6 tend to be trapped around the latitude of the jet stream core (Hoskins and Karoly 1981 and Branstator 2002). The alternating troughs and ridges in Fig. 2.5 are suggestive of such trapping. For a Rossby wave that propagates in the westly flow, and has little variations in the latitudinal direction compared to its zonal scale, the stationary Rossby wavenumber is calculated to support the result from spectral analysis. Based on the method proposed by Hoskins and Karoly (1981; Hoskins and Ambrizzi (1993); and Wills et al. (2019), the stationary Rossby wavenumber is calculated as follows:

$$K_s = a\cos\varphi \left(\frac{\beta - \frac{\partial^2 [U]}{\partial y^2}}{[U]} \right)^{\frac{1}{2}}, \qquad (2.5)$$

where K_s is the stationary wavenumber, a is the radius of Earth, $cos\varphi$ is cosine of latitude, $\beta = 2 \times 10^{-11}$ m^{-1} s^{-1} is the gradient of planetary vorticity (i.e. the Rossby parameter), and $[U]$ is the zonal-averaged zonal wind. Based on the values of the fields shown in Fig 2.5, we obtain a value of K_s of 6. Thus, the value of the stationary wavenumber is consistent with the observed scale of the wave train shown in Figs. 2.4 and 2.5.

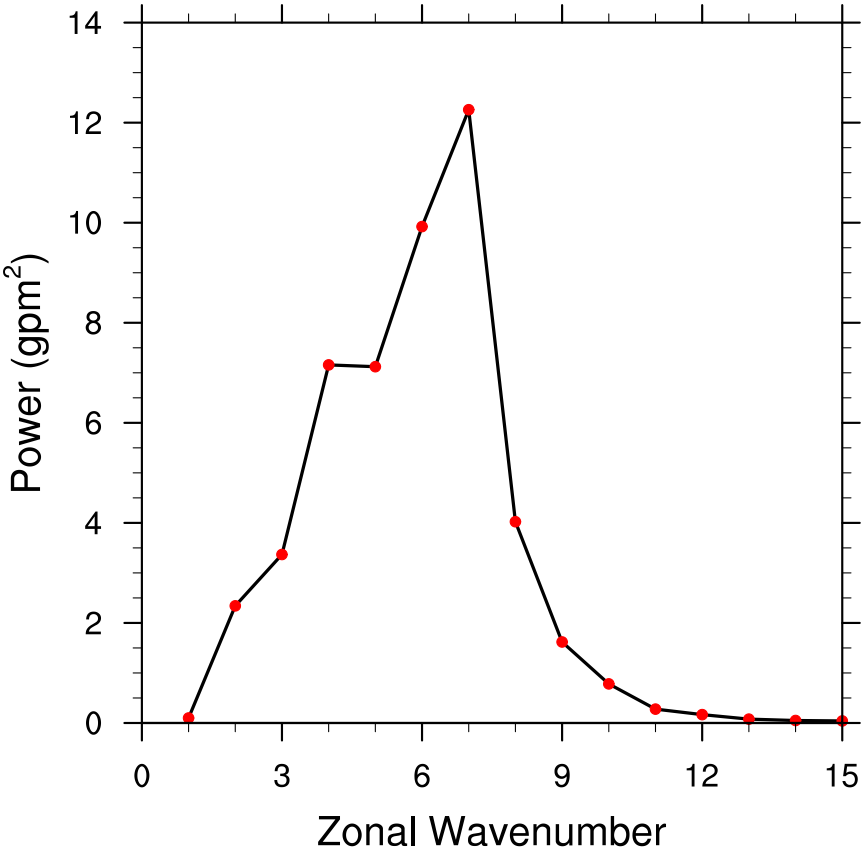

FIG. 2.6. Power spectral density (in units of gpm2) as a function of zonal wavenumber for 200 hPa geopotential height anomalies regressed onto the BHI and meridionally averaged over the $40°N$-$50°N$ latitude belt. The spectral power at each zonal wavenumber is shown as a red dot.

Figure 2.7 shows the Takaya-Nakamura (T-N) wave activity flux (Takaya and Nakamura 1997, 2001) of the 200 hPa geopotential anomalies, overlaid with vertical velocity anomalies averaged over the 300-500 hPa layer, the layer in which vertical motions are strongest in Fig. 2.4. The wave activity fluxes are used to depict the propagation of energy in a wave train. Unlike the

previous figures, these are composites based on the negative phases of the BHI. We chose to show composites due to nonlinearities in the wave activity flux calculation, which project poorly onto a linear regression. Wave activity flux arrows indicate eastward propagation of wave activity from the North Pacific towards the Atlantic. The regions of ascent and descent over the Atlantic sector are collocated with the enhanced and suppressed precipitation, respectively, suggesting that vertical motions associated with this wave train may at least partly explain the fluctuations in precipitation over this region. Statistically-significant regions of vertical motion are also observed over the northeast Pacific and Great Lakes region.

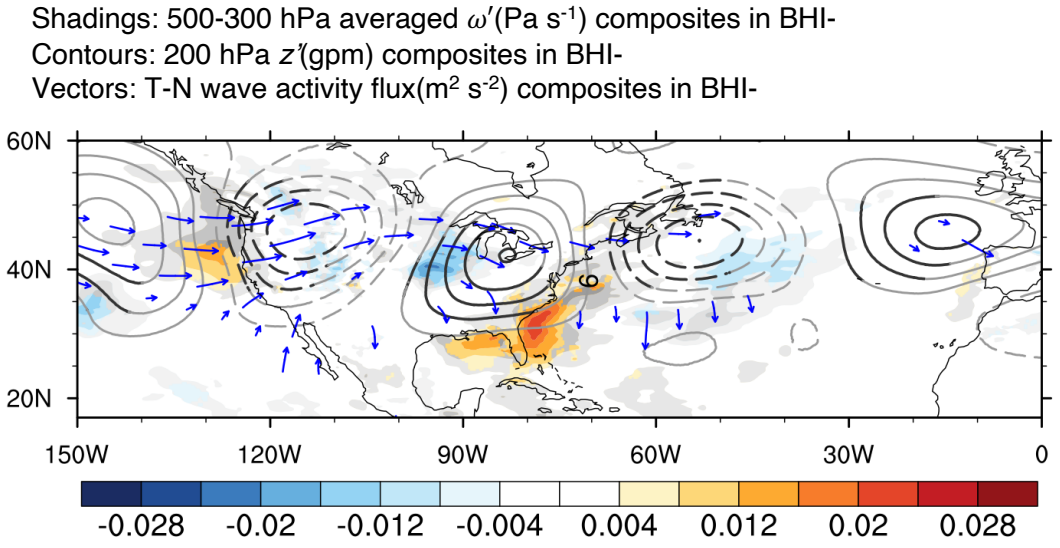

FIG. 2.7. Geopotential height anomalies on 200 hPa (gpm, contours, the interval is 6 gpm), Takaya-Nakamura (T-N) wave activity flux (m2 s^{-2}, vectors) and vertical velocity anomalies (m s^{-1}, shading) composited for negative BHI years. The vertical velocity is averaged from 300-500 hPa and smoothed in longitude with a running window of 2.5°. The black contours and blue/red shadings are significant at 95% confidence interval. The vectors are masked out in where the wave train is not significant at the 95% confidence interval.

To see if anomalous precipitation associated with this wave train occurs away from the BH region, Fig. 2.8 shows the precipitation anomalies over the northern hemisphere extratropics. Though significant vertical motions and associated geopotential height anomalies are seen throughout the extratropics, statistically-significant precipitation anomalies are observed only over

the northwestern US, SEUS and northwestern Atlantic. A region of statistically-significant rainfall is seen in the tropical western Pacific, although from Fig. 2.8 it is unclear if this region of rainfall is connected to the rest of the wave train. The latter two exhibit the strongest precipitation anomalies. This is likely because the SEUS and northwestern Atlantic exhibit high concentrations of water vapor during JA (Fig. 2.2 and 2.3, see also Kållberg et al. 2005). The consistency in the structure of the wave in the 200 hPa and 500 hPa levels supports the idea that this wave train exhibits an equivalent barotropic structure.

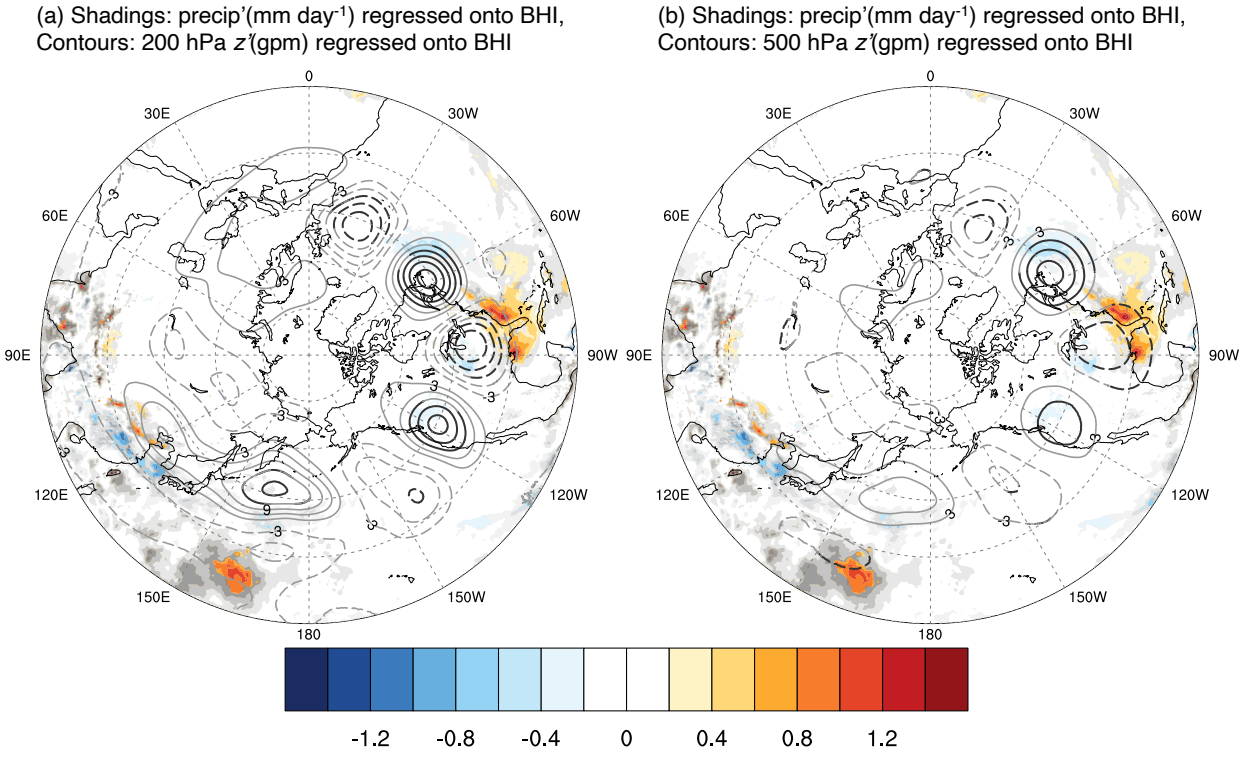

FIG. 2.8. 200 (a) and 500 (b) geopotential height anomalies (contours, with an interval of 3 gpm) and ERA5 precipitation anomalies (shadings, with a unit of mm day^{-1}) regressed onto the BHI. The black contours are statistically significant area of geopotential height at 95% confidence interval and the blue/red shading are that of precipitation.

In order to quantify whether large-scale motions are the cause of the precipitation anomalies in the SEUS, we will now analyze the thermodynamic energy equation, which can be written following Nie and Sobel (2016) as:

$$C_p \frac{\partial T}{\partial t} + C_p \mathbf{v} \cdot \nabla_h T + \omega \frac{\partial S}{\partial p} = J, \tag{2.6}$$

where C_p=1004 $J \cdot K^{-1} kg^{-1}$ is the specific heat of dry air under constant pressure, $\frac{\partial}{\partial t}$ is the local time derivative, T is the temperature, $\mathbf{v} \cdot \nabla_h T$ is the horizontal advection of temperature, ω is the vertical pressure velocity, $\frac{\partial}{\partial p}$ is the partial derivative with respect to pressure, $S = C_p T + \Phi$ is the dry static energy (Φ is geopotential) and J is the diabatic heating rate. We assume that $\frac{\partial T}{\partial t}$ is negligibly small due to the low frequency of the pattern that we are analyzing, and $\frac{\partial S}{\partial p}$ is nearly constant (Adames and Ming 2018b). The vertical integration of J describes the sum of the surface precipitation rate and the column-integrated radiative heating rate (Yanai et al. 1973):

$$\langle J \rangle = \frac{1}{g} \int_{100\ hPa}^{1000\ hPa} J \mathrm{d}p \simeq L_v P + \langle Q_r \rangle, \tag{2.7}$$

where $\langle \cdot \rangle$ denotes the vertical integration, $g = 9.8\, m\, s^{-2}$ is gravitational acceleration, $L_v = 2.5 \times 10^6\, J \cdot kg^{-1}$ is the latent heat of vaporization, P is precipitation rate, and Q_r is the radiative heating rate. Applying Eq. (2.7) to (2.6), and rearranging the terms, it becomes a diagnostic equation for ω:

$$\langle \omega \rangle \simeq \left(\frac{\partial \overline{S}}{\partial p} \right)^{-1} \left[L_v P + \langle Q_r \rangle - \left\langle C_p u \frac{\partial T}{\partial x} \right\rangle - \left\langle C_p v \frac{\partial T}{\partial y} \right\rangle \right], \tag{2.8}$$

where u is the zonal wind and v is the meridional wind. The overline in the dry static energy is used to denote that we are using a tropospheric mean value. The first term on the right-hand side is latent heat from phase changing, the second term is the column radiative heating anomaly, the third term is zonal temperature advection and the fourth term is meridional temperature advection.

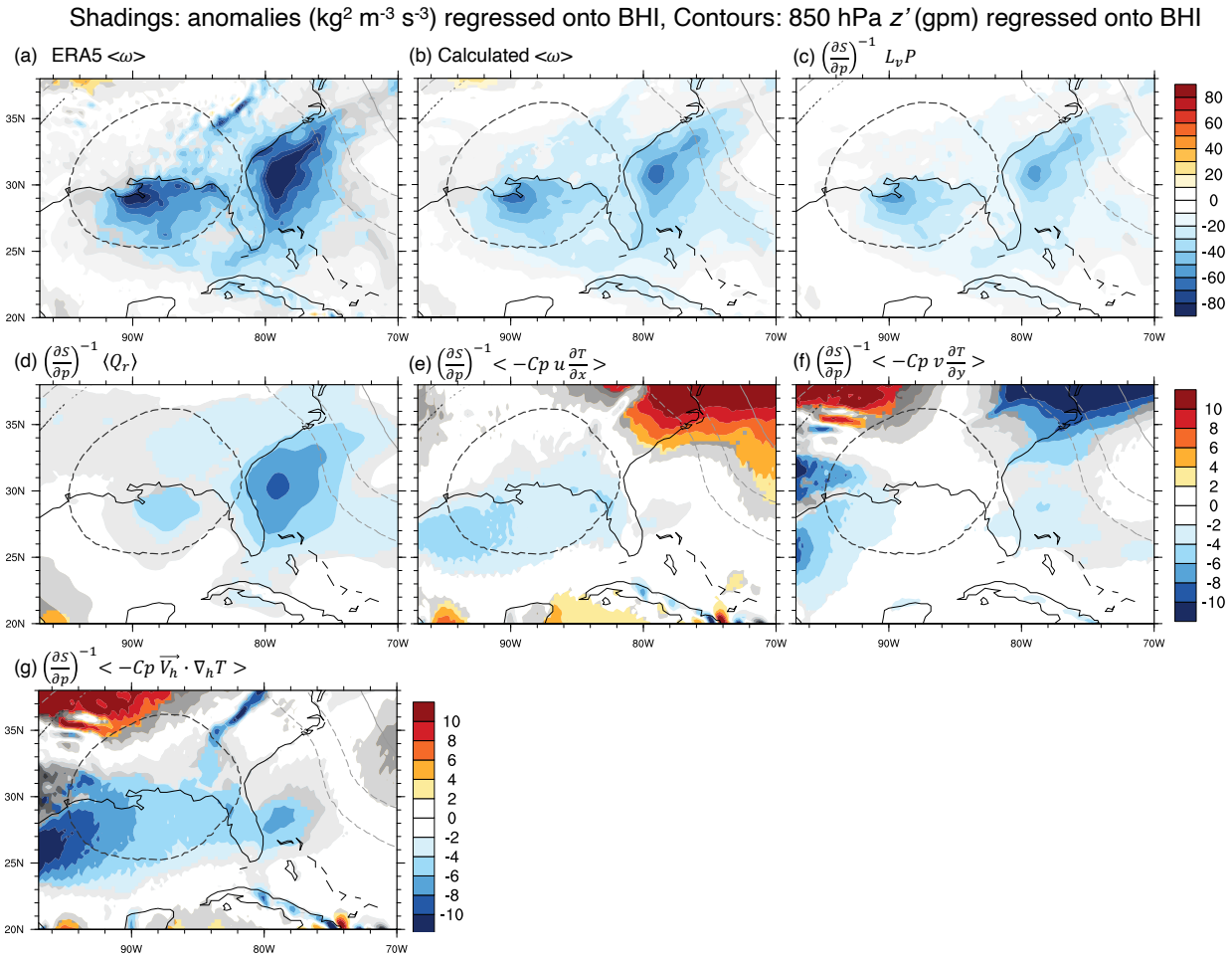

FIG. 2.9. 850 hPa geopotential height anomalies (gpm, contours, interval of 1 gpm) and column-integrated vertical velocity contributions (kg2 m^{-3} s^{-3}, shading) regressed onto the BHI. The vertical velocities are (a): ERA5 column-integrated vertical velocity; (b): column-integrated vertical velocity estimated from Eq. (2.8); (c): contribution from latent heating; (d): contribution from radiative heating; (e): zonal temperature advection; (f): meridional temperature advection; (g): total horizontal temperature advection. Black contours and blue/red shadings are statistically significant at 95% confidence interval.

Equation (2.8) allows us to quantify the vertical velocity in the column as a result of diabatic heating or anomalous temperature advection, which is related to the quasi-geostrophic (QG) omega equation in Eq. (2.4). The results, shown in Fig. 2.9, reveal that the pattern of vertical velocity in the SEUS is predominantly a result of latent heat release in precipitating clouds. However, ascent associated with radiative heating and warm advection is also seen in this region, although these are of a much smaller magnitude. Radiative heating contributes to the anomalous

ascent near the north part of the Gulf of Mexico and to the east of Florida. Both zonal (Fig. 2.9e) and meridional (Fig. 2.9f) temperature advection contribute to the anomalous ascent seen in this region. Zonal temperature advection predominantly contributes to ascent over the northeastern Gulf, while meridional temperature advection is more important over the western Gulf and to the east of Florida. That the precipitation in the Gulf of Mexico is located in a region of warm air advection suggests a potential relationship between the two.

2.5 Discussion and Conclusions:

Our study of the Bermuda High (BH) is based on the Bermuda High index (BHI) during July and August. The BHI shows that the BH varies on an interannual scale, expanding westward during some seasons and contracting during others. The strongest contraction and expansion tend to take place in July. A multi-decadal variation is also found in the BHI, indicating a shift from majorly expansion to contraction in the last two decades. We hypothesize that this trend may be a result of low-frequency, multidecadal oscillations. More work is needed to elucidate the case of this multidecadal shift.

In order to answer question (1), “Are variations in the BH linked to the rainfall variations during July and August in the southeast US (SEUS)?”, we created a scatterplot comparing the BHI to rainfall in the (Fig. 2.1d). A strong correspondence is seen between the two, with a correlation of 0.68. Suppressed rainfall over the SEUS is related to the westward expansion of the BH.

Composites of mean precipitation illustrate the rainfall distribution in the two phases. During the contraction phase, precipitation shifts towards the southern, southeastern and eastern coast of the US. This region also corresponds to the northwestern edge of the Bermuda High. During the expansion phase, the coastal areas are drier while wetter near the US Midwest. These

findings are consistent with previous studies that showed a correlation between the westward expansion of the BH and the occurrence of suppressed rainfall (Giannini et al. 2000; Small et al. 2007). Linear regression analysis of rainfall and geopotential on the BHI clearly show this relationship (Fig. 2.3). The same results are obtained on the basis of EOF and MCA analysis (see Appendix B)

Fluctuations in tropospheric-averaged temperature across the US are also observed in association with the fluctuations in the BH. The displacement of cold and warm centers with respect to anomalous cyclones and anticyclones, as well as the existence of temperature anomalies in the western US indicates that fluctuations in the BHI are the result of an extratropical wave train. The potential existence of this wave train would lead to a hypothetical answer to question (2) " what is the mechanism that leads to variations in the BH and the occurrence of the precipitation variations in the midsummer". We performed BHI-based linear regression analysis of the geopotential height anomalies on the 200 hPa level, revealing a wave train that encompasses much of the northern extratropics. It exhibits a zonal wavenumber near 6 or 7 and appears to be guided by the midlatitude westly jets. The wave train exhibits an equivalent barotropic structure with its strongest amplitude occurring at the 200 hPa level.

While the wave train encompasses a large region of the northern hemisphere extratropics, its modulation of precipitation is largely confined to the BH region. The anomalous vertical motion over the SEUS is mainly attributed to anomalous diabatic heating (Fig. 2.9). Radiative heating and horizontal temperature advection are much smaller in amplitude, but nonetheless contribute non-negligibly to the total vertical motion. That the anomalous precipitation is collocated with warm advection suggests a potential physical connection, at least over the Gulf of Mexico. It is possible that ascent associated with warm air advection moistens the troposphere through isentropic lifting,

leading to a more favorable environment for precipitation. Upper-tropospheric clouds then reinforce the lifting by reducing the outgoing longwave radiation. Previous studies also suggested that horizontal advection of moisture also plays a role in precipitation anomalies associated with BH fluctuations (Henderson and Vega 1996; Diem 2006). While we did not examine the role of horizontal moisture advection in this study, we do not discard the possibility that both temperature and moisture advection are creating a thermodynamic environment that is more favorable for precipitation in this region. Additionally, because of the way the precipitation anomalies are oriented with respect to the land, it is possible that interactions between the land, the sea and the atmosphere also play a role in determining the distribution of rainfall. More work is needed to establish the mechanism that leads to rainfall in the SEUS in association with fluctuations in the BH.

Our results suggests that fluctuations in the BH modulates rainfall in the SEUS, and that this modulation is associated to a Rossby wave train in the midlatitudes. We sought to understand the energetics of this wave trough by calculating barotropic or baroclinic energy conversions but the results were inconclusive. It is possible that the Rossby wave train is the result of mechanisms that vary from year to year.

In this chapter, the dynamics of a mid-latitude Rossby wave and its relationship with the Bermuda High and anomalous precipitation was investigated. The latent energy is critical to vertical motions but the temperature advections and radiative fluxes are also important. In the next two chapters, we will pay attention to a tropical wave over the Indian Ocean, which is mainly driven by the latent energy and has little fluctuations in temperature. The wave also induces anomalous precipitation along its track and thus causes social-economic losses to less-developed territories.

2.6 Appendix

2.6.1 EOF Analysis

Regression patterns similar to those shown in the main text can be obtained through EOF analysis of rainfall data over the Atlantic North America sector (17-50°N, 10-125°W). The first and second EOFs are statistical significantly separated according to the method presented by North et al. (1982). The leading EOF of rainfall variability in this region (not shown) is reminiscent of teleconnection patterns associated with ENSO variability during boreal summer (Ropelewski and Halpert 1987), and exhibits a correlation of 0.53 with the Niño 3.4 index. The second EOF (Fig. 2.10a) explains 7.2% of the total JA precipitation variance in the Atlantic-North America domain. Regression maps of rainfall and 850 hPa geopotential height are nearly identical to those obtained using the BHI. The principal component time series associated with this pattern exhibits a correlation with BHI of 0.7.

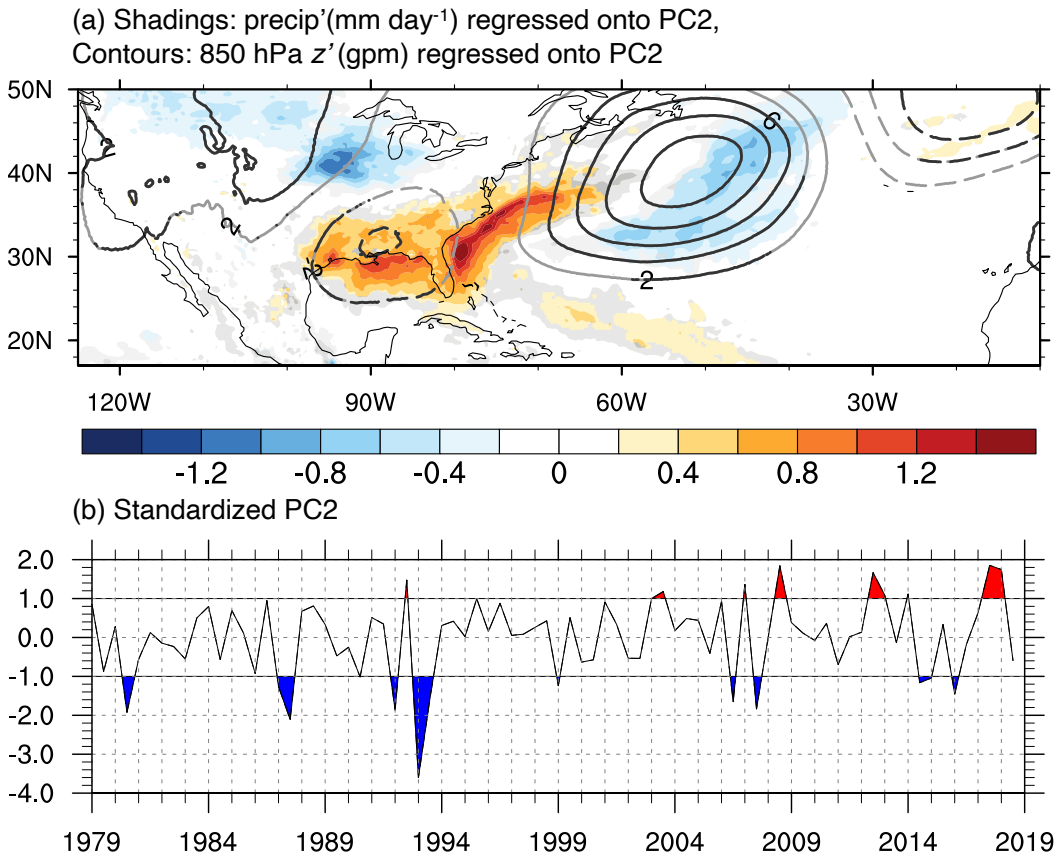

FIG. 2.10. (a): 850 hPa geopotential height anomalies (contours, with an interval of 2 gpm) and ERA5 precipitation rate anomalies (shading, in units of mm day^{-1}) regressed onto the second principal component of the plotted domain, which explains 7.2% of the variance and has a correlation with BHI as of 0.7. Black contours and blue/red shading are statistically significant values at 95% level. (b): Standardized principal component 2.

2.6.2 Maximal Covariance Analysis

Maximal covariance analysis is applied on precipitation and geopotential height anomalies. As in the EOF analysis discussed previously, the leading MCA pattern is correlated with ENSO. The MCA is also tested using North et al.'s (2014) method and proved to be significantly separated. The second MCA is more closely related to the BHI and is shown in Fig. 2.11, with panel (a) showing the homogenous map and (b) showing the heterogeneous map, explain 12.4% of total variance. The map exhibits some similarity to the patterns shown in Fig. 2.3a, except the MCA emphasizes rainfall anomalies occurring over the tropical Atlantic more. The time series associated

with the second-leading pattern exhibit a correlation with the BHI of 0.78. The principal component 2 shown in Fig. 2.10b also has a similar trend as BHI of BH shifting from negative to positive during the recent two decades, even it is calculated from detrended precipitation.

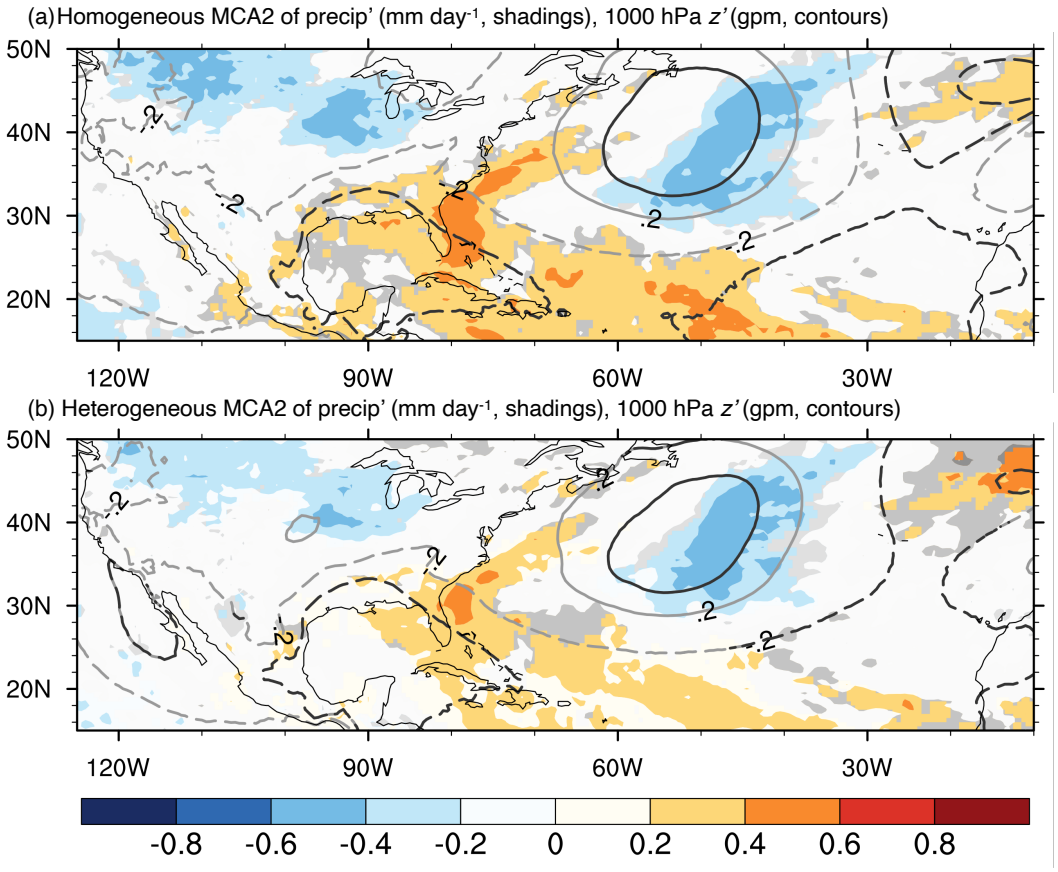

FIG. 2.11. MCA2 of precipitation and 1000 hPa geopotential height anomalies. The shadings are the homogeneous (a) or heterogeneous (b) field for precipitation, the contours are those of geopotential height anomalies respectively. It explains 12.4% of the total variance. The left expansion coefficient (precipitation) has a correlation with BHI as of 0.78 and the right one (geopotential height) is 0.79. The dark contours and blue/red parts are significant values at the 95% level.

Chapter 3 Barotropic and Moisture-vortex growth of Monsoon Low Pressure Systems

Luo et al. 2023: Published on the Journal of the Atmospheric Sciences, 1, https://doi.org/10.1175/JAS-D-22-0252.1.

3.1 Introduction

Westward or northwestward-propagating synoptic-scale disturbances are frequently observed over the Bay of Bengal during the summer monsoon season. Often referred to as monsoon low-pressure systems (MLPSs), these systems exhibit a horizontal structure of roughly 2000 km across and extend vertically from the surface to 100 hPa (Krishnamurti et al. 1975; Godbole 1977; Sikka 1977; Adames and Ming 2018a). From June to September, around 2-4 MLPSs form per month on average (Krishnamurti et al. 2013; Thomas et al. 2021, 2022). In spite of their short 3-to-5-day life cycle, they play an important role in the hydrologic cycle of South Asia, accounting for up to 50% of the summer monsoon rainfall (Krishnamurti 1979; Saha et al. 1981; Yoon and Chen 2005; Yoon and Huang 2012; Thomas et al. 2021). The variation of precipitation brought about by MLPSs significantly impacts agriculture and fishery (Dong et al. 2017; Thomas et al. 2021). It is not only a major source of fresh water to one of the most densely populated areas of the world, but it is also a major cause of life-threatening floods, as previous studies have documented (Ajayamohan et al. 2010; Hunt et al. 2018; Hunt and Fletcher 2019). Although MLPSs have been extensively documented, the mechanisms responsible for their growth and propagation have remained elusive. MLPSs are situated in a vertically-sheared environment that is conventionally thought to favor baroclinic instability (Charney and Stern 1962;

Krishnamurti et al. 1975, 2013). As a result, previous studies hypothesized that baroclinic instability (Rao and Rajamani 1970; Saha and Chang 1983), often enhanced by cumulus heating (Moorthi and Arakawa 1985; Krishnakumar et al. 1992; Kasture et al. 1993), or baroclinic-barotropic instability can excite and amplify these systems (Aravéquia et al. 1995). However, major disagreements between observations and theory have made the idea of baroclinic growth in MLPSs questionable (Cohen and Boos 2016). Vertical cross-sections of potential vorticity documented in previous studies show upright or slightly westward tilted structures and neither of the two is characteristic of baroclinic instability under easterly shear. Results from idealized simulations of MLPSs also agree that baroclinic instability does not explain MLPS growth (Diaz and Boos 2019a; Clark et al. 2020).

With baroclinic instability unlikely to be the source of growth of MLPSs, alternative hypotheses have been proposed. One potential theory, namely, is the moisture-vortex instability (MVI) (Adames and Ming 2018a). A generalization of the balanced moisture waves described by Sobel et al. (2001), MVI (Fig. 3.1, Adames 2021) emphasizes the role of prognostic moisture in MLPS-related rainfall and horizontal gradients of moisture and temperature in MLPSs growth. As one of the emblematic features, the meridional advection of moist static energy (MSE) induces a moisture tendency to the west of the MLPSs. The convection is then enhanced by the anomalously high moisture, which peaks near or slightly to the west of the center of the vortex. Lastly, the vortex strengthens due to vortex stretching. Adames (2021) recently posited that MVI is amplified over south Asia at the expense of baroclinic instability, potentially explaining why baroclinic instability is not observed in this region.

The south Asian monsoon is also characterized by strong meridional shears in the zonal wind that allow it to be barotropically unstable (e.g., Lindzen et al. 1983; Nitta and Masuda 1981).

However, dry barotropic instability alone does not provide adequate energy to allow MLPSs to grow against dissipation (Diaz and Boos 2019a). As a result, it has been hypothesized that a variant of barotropic instability that includes moist processes, termed moist barotropic instability, can explain MLPS growth (Diaz and Boos 2019a,b). Though the explanations for how diabatic heating enhances the vortex are different, the theory still shares some similarities with MVI. For example, the low-level meridional MSE gradient is still a primary energy source and the moisture advected by the winds towards the vortex enhances the convection (Diaz and Boos 2021a).

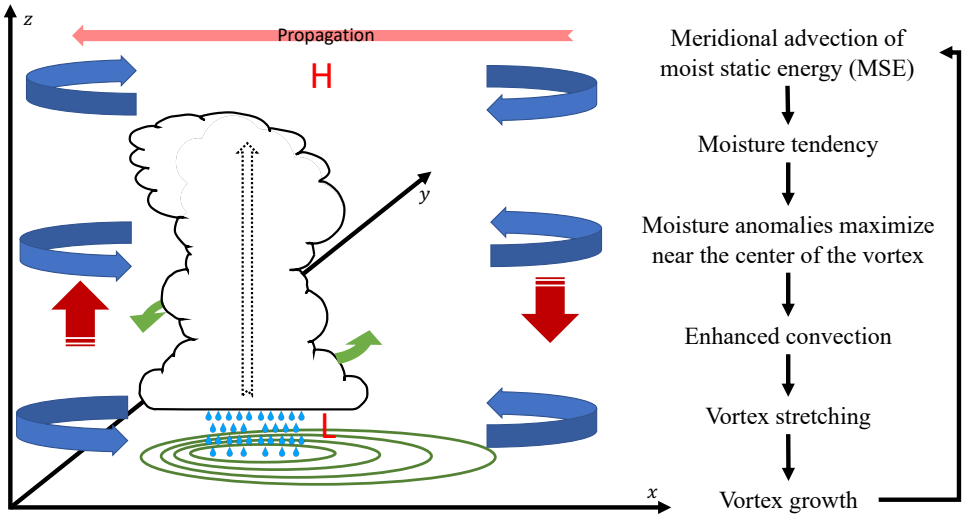

FIG. 3.1 Schematic of moisture-vortex instability (left). The light red arrow on the top refers to the westward propagation. The blue curved arrows represent the circulations at low, mid and high levels, with a high pressure on the top and a low pressure on the bottom. The meridional MSE advection is shown as the green arrows. The dark red upward (downward)-pointing arrow refers to the adiabatic lifting (subsidence). The contours near the surface represent a high column moisture center, which is partly colocated with the precipitation. The dashed arrow is enhanced convection. A flow chart showing this mechanism is on the right.

In this chapter, we will examine the energetics of MLPSs in order to elucidate the processes that may be able to explain their growth. Because we are investigating barotropic and moisture-vortex instabilities, we will emphasize the moist static and perturbation kinetic energy budgets. The contents are structured as follows: the data and methods used in this study are shown in section

3.2. The climatological features of monsoons and disturbances are depicted in Section 3.3. Section 3.4 is the analysis on MVI and barotropic instability energetics. Concluding remarks are shown in Section 3.5.

3.2 Data and methods

The data used in this study is the fifth reanalysis product from the European Centre for Medium-Range Weather Forecasts (ERA5, Hersbach et al. 2019). We examined the MLPSs from 1980 to 2019 for the extended boreal summer, June to September (JJAS), when MLPSs are the most active. The temporal resolution is six hours, the spatial resolution is $0.5° \times 0.5°$ in longitude and latitude, and 27 layers ranging from 1000 to 100 hPa in the vertical direction.

Our analysis is based on linear regressions onto an MLPS index. Different indices were used to represent MLPS activity in previous studies for different purposes (Boos et al. 2015; Ditchek et al. 2016). In this study, we put emphasis on rainfall-related features so our index is based on precipitation anomalies that are filtered in space and time and regionally averaged over a spot with strong rainfall variabilities (Hayashi 1971, 1979; Wheeler and Kiladis 1999; Wheeler et al. 2000). The applied filter retains data between westward zonal wavenumbers 3 to 25, and frequencies between 1/15 to 1/2 day^{-1}, where the strongest signal shows up on the wavenumber-frequency diagrams (Adames and Ming 2018b). The outputs were then averaged over a box area, $85 - 90°E$, $15 - 20°N$ (red box in Fig. 3.2a,b) (Sikka 1977; Godbole 1977; Boos et al. 2015; Adames and Ming 2018b). The location has a precipitation rate and variance. It is also the place for maximum MLPS genesis (Krishnamurthy and Ajayamohan 2010; Boos et al. 2016). The index was then standardized by subtracting its temporal average and being divided by its standard deviation. We have verified that similar results are obtained if an alternative index based on the

sea-level pressure is used as a time series or if EOF analysis is used instead in the Appendix. Statistical significance of the regression fields is determined by a two-tailed t-test (Davis 1978; Chen 1982; Adames and Wallace 2014) at a level of 95%. Only anomaly fields that are found to be statistically significant according to this test are shown.

Most of the fields were integrated through the atmospheric column. The mass-weighted vertical integrals were calculated using the following equation (Adames and Ming 2018b):

$$\langle \blacksquare \rangle = -\frac{1}{g}\int_{p_s}^{p_t} \blacksquare \, dp, \tag{3.1}$$

where $g = 9.8\, m\, s^{-2}$ is the gravitational acceleration, $p_\mathrm{t} = 100$ hPa and $p_\mathrm{s} = 1000$ hPa are seen as the tropopause and surface pressures, respectively, and "■" represents an arbitrary quantity.

Our study focuses on the MSE and perturbation kinetic energy (PKE) of MLPSs. The MSE is defined as:

$$m = C_p\, T + \Phi + L_v\, q, \tag{3.2}$$

where m is MSE; $C_p = 1004\, J \cdot (K \cdot kg)^{-1}$ is the heat capacity at constant pressure, T is temperature, Φ is geopotential, $L_v = 2.5 \times 10^6\, J\, kg^{-1}$ is the specific latent heat and q is specific humidity. The sum of the first two terms is the dry static energy (DSE).

PKE is defined as:

$$K' = \frac{1}{2}(u'^2 + v'^2), \tag{3.3}$$

where K' is PKE, u' and v' are the zonal and horizontal wind temporal anomalies obtained through the filtering process. In this chapter, we use the prime sign to represent the anomalies in time and bar sign to represent the background state in which the anomalies propagate.

3.3 Characteristics of monsoon low pressure systems

To better understand the processes that govern the evolution of MLPSs, it is instructive to first consider the climatology of the south Asian monsoon, shown in Fig. 3.2. The Bay of Bengal, where MLPS activity is the strongest, is characterized by average precipitation rates that exceed 4 $mm\,day^{-1}$ (Fig. 3.2 b). The rainfall maxima are on the west coast of India, central India as well as the eastern and northern Bay of Bengal. Our indexing area is to the east of the monsoon trough, with a precipitation rate standard deviation higher than 20 $mm\,day^{-1}$ (Fig. 3.2a). In Fig. 3.2b, a low-level westerly jet shows up at around 10 to 20 °N at 850 hPa. The westerlies peak near 60 °E and slow down when encountering the Western Ghats at 75 °E and the Eastern Ghats at 80 °E. Then they speed up when entering the Bay of Bengal.

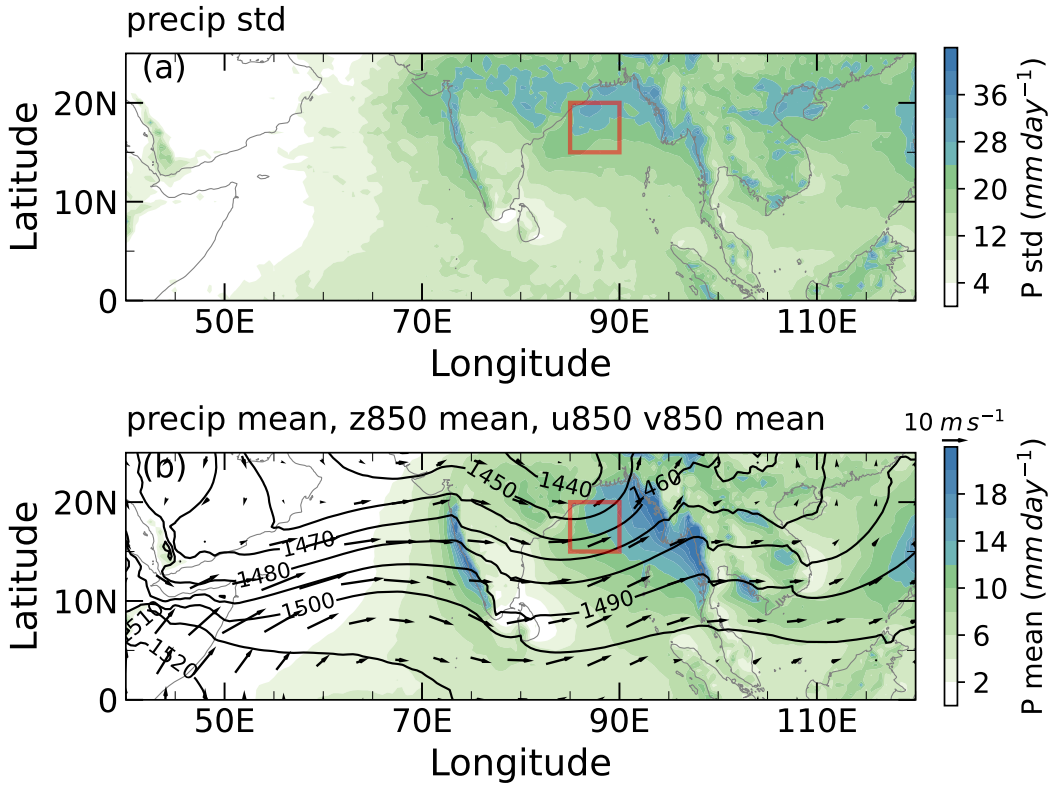

FIG. 3.2 (a) Standard deviation of JJAS mean total precipitation rate. The MLPS index was calculated by averaging the precipitation anomalies over the area within the red box. (b) JJAS mean precipitation (shadings), geopotential height (contours, starting from 1440 gpm to 1540 gpm, at an interval of 10 gpm) and winds at 850 hPa (vectors).

The disturbances and related precipitation (P') that grow in this background state are shown in Fig. 3.3. The lag regressions were calculated from two days before (day -2) the maximum signal to two days after (day 2). At 850 hPa, anomalous anticyclones are colocated with suppressed precipitation, and enhanced precipitation is in-phase with the anomalous cyclones. Although the circulation and the precipitation anomalies are generally colocated with each other, there is a small displacement between the two fields with rainfall centers shifted towards the southwest of the troughs and ridges. Individual highs and lows move across 15° westwards while only 5° northward.

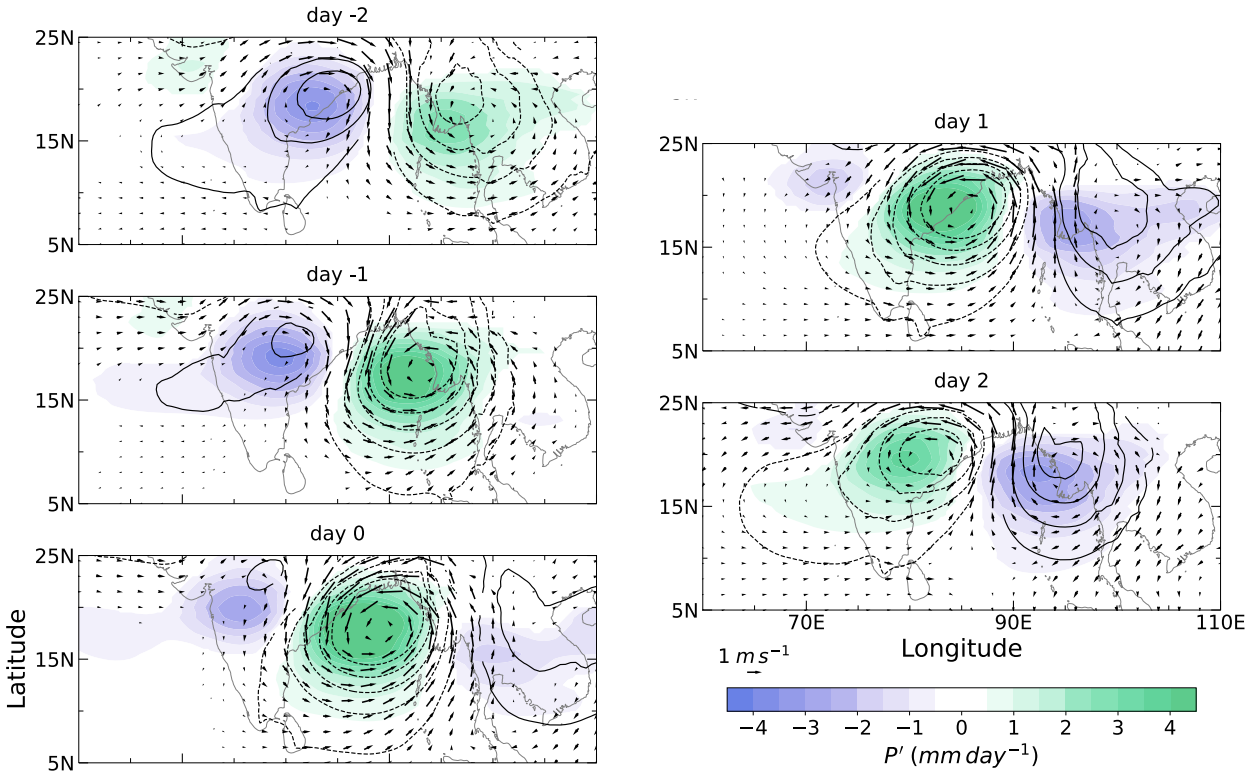

FIG. 3.3 Lag regressions from day -2 (top) to day 2 (bottom) of anomalous precipitation rate (shadings), geopotential height (contours, starting from $-4\ gpm$ to $4\ gpm$ at an interval of $1\ gpm$) and winds (vectors) at 850 hPa onto MLPS index during JJAS. Only statistically significant anomalies are shown.

On day -2, the centers of the negative precipitation anomalies are located near the eastern coast of India, and the positive anomalies are over the eastern Bay of Bengal. From day -2 to day

0, the positive precipitation anomalies amplify. On day 0, the negative precipitation anomalies are located in northwestern India, and the positive anomalies are centered over the northwestern Bay of Bengal. From day 1 to day 2, the positive center and the negative center to the west weakened, while the newly developing negative center on the east intensified along with the anti-cyclonic flow. On day 2, the locations of the centers are the same as on day -2 but with a reversed pattern.

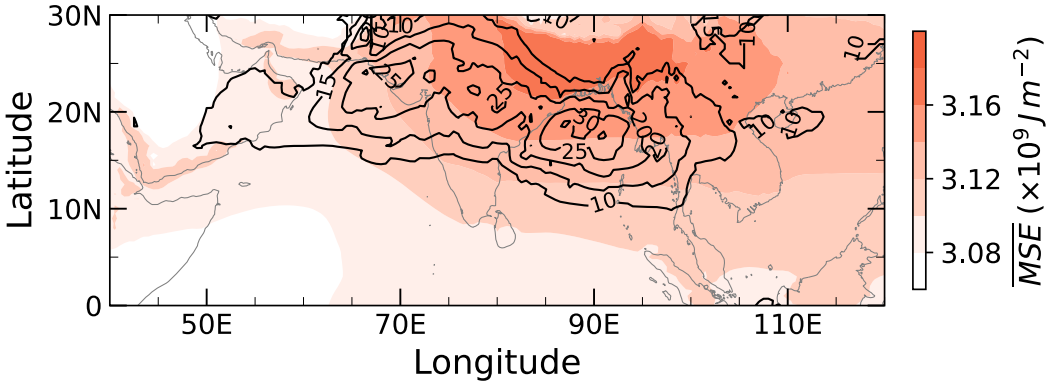

FIG. 3.4 Column-integrated mean MSE is shown as shading. The contours are the root-mean-square of anomalous MSE regressed onto the MLPS index from day -2 to day 2 (from 0 to 30× $10^9\ J\ m^{-2}$ at an interval of 5× $10^9\ J\ m^{-2}$, contour labels are).

The lag regressions of anomalous column-integrated MSE exhibit a similar pattern as the rainfall anomalies (not shown). Their root-mean-square amplitude is shown as the contours in Fig. 3.4. The shading shows the climatological mean column-integrated MSE. Mean MSE increases from southwest to northeast and peaks near $25\,^{\circ}N$, $90\,^{\circ}E$. The contours show the west-northwestward propagation of the MLPSs, which approximately follows the contours of mean MSE from $\sim 70\,^{\circ}E$ to $105\,^{\circ}E$.

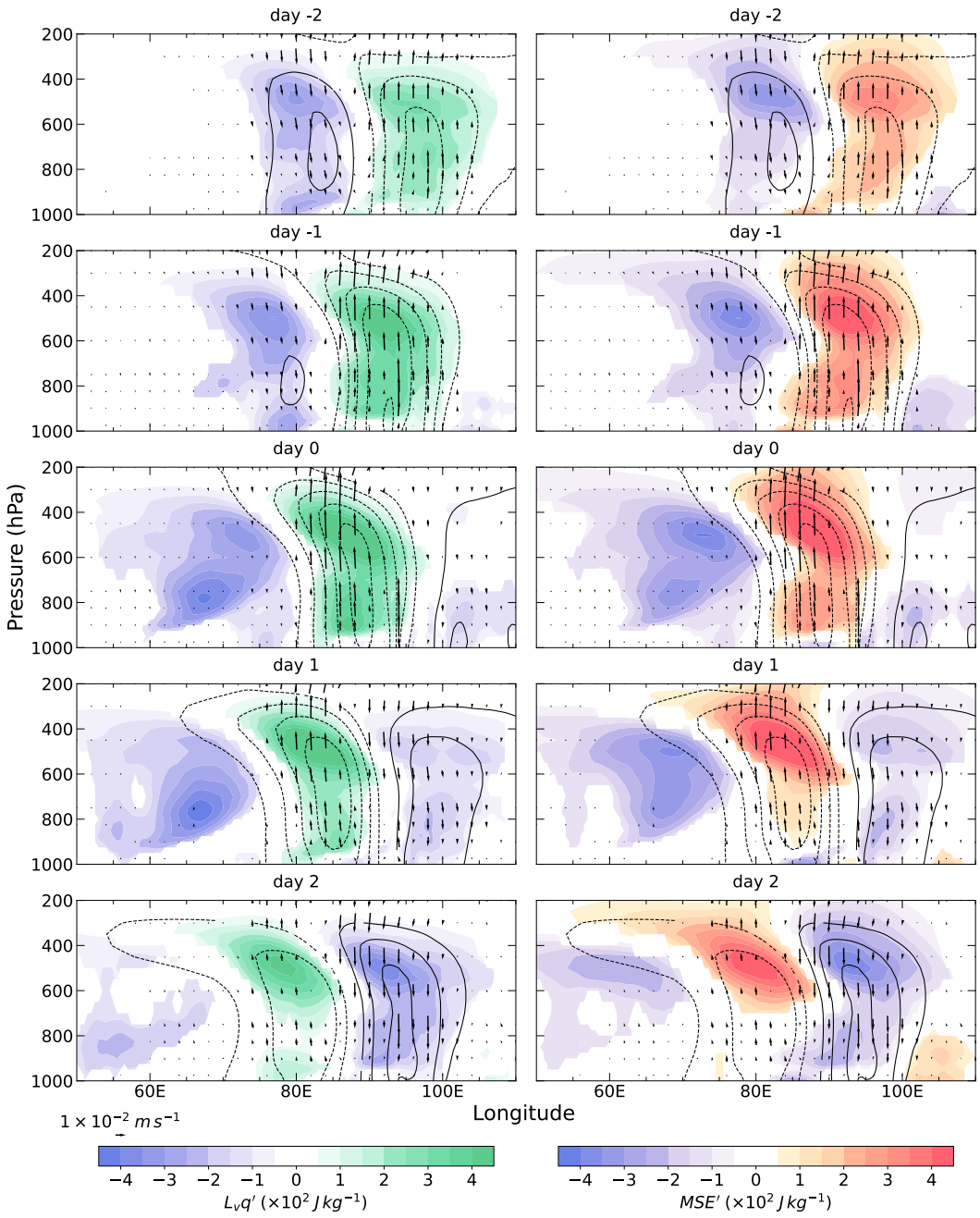

FIG. 3.5 Longitude-height cross-sections of anomalous latent energy ($L_v\, q'$, shadings on the left), MSE (shadings on the right), geopotential height (contours, from -5 gpm to 5 gpm at an interval of 1 gpm) and zonal and vertical winds (vectors, vertical winds are scaled to a larger magnitude) anomalies regressed onto MLPS index from day -2 (top) to 2 (bottom) during JJAS. Averaged over $10 - 25°N$. Only statistically-significant anomalies are shown.

The longitude-height cross-sections of meridionally-averaged $(5 - 20°N)$ geopotential height, winds, moisture and MSE are shown in Fig. 3.5.The vertical distribution of geopotential

height (contours) is upright during growth and tilts westward with height when it decays, consistent with previous findings (Godbole 1977; Hunt et al. 2016; Cohen and Boos 2016). The negative anomalous latent energy (left shadings) had a maximum near 500 hPa in the growing stage, while it is around 800 hPa during its decay. The negative anomalous MSE (right shading) however, persisted at 500 hPa. The structure of enhanced latent energy and MSE are similar. The vertical wind anomalies (u, ω, vectors in Fig. 3.5 with ω scaled for better display) exhibit an upward motion within the positive moisture and MSE anomalies while downward motion in the negative MSE anomalies.

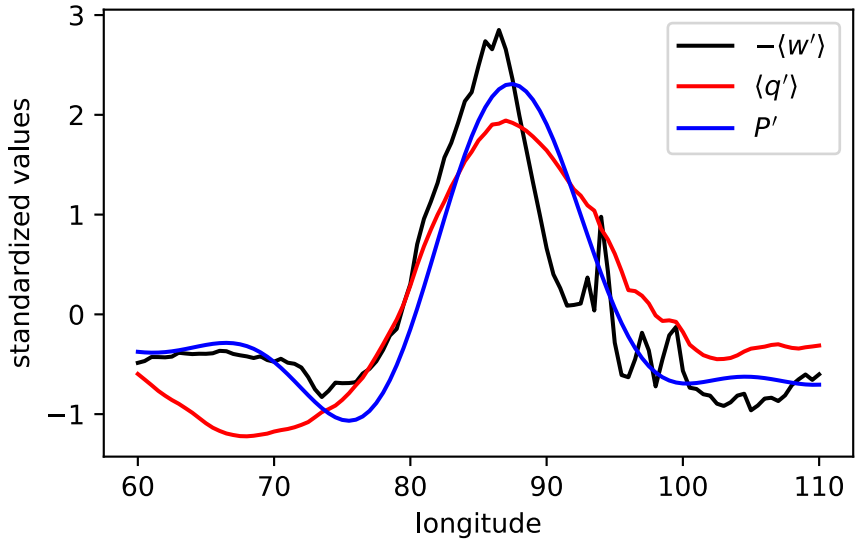

FIG. 3.6 Column-integrated anomalous vertical velocity (black), moisture (red) and precipitation (blue), zonally averaged across $10 - 25°N$ on day 0. The values are standardized as discussed in Section 3.3.

As discussed in the previous sections, the upright structure shown in the vertical cross-sections is inconsistent with baroclinic instability, which requires an eastward tilt with height. The peaks of column moisture and the precipitation anomalies, shown in Fig. 3.6, colocate with each other near $88°E$. To better present, the values are standardized by subtracting their temporal averages and then divided by standard deviations. The anomalous ascent is shifted about 3°

westward with respect to the other two fields. The vertical structure and shift shown in Fig. 3.6 are consistent with MVI as shown in Fig. 14 of Adames (2021).. The upright structure in geopotential and horizontal winds is also consistent with barotropic growth.

3.4 Energetics

3.4.1 Moist static energy budget

In this section, we will investigate MSE and PKE budgets and show the major possible contributors to the growth and propagation of MLPSs. Following Adames and Ming (2018a), the tendency of MSE can be broken down into the following terms:

$$\frac{\partial \langle m' \rangle}{\partial t} = -\left\langle u \frac{\partial m}{\partial x} \right\rangle' - \left\langle v \frac{\partial m}{\partial y} \right\rangle' - \left\langle \omega \frac{\partial m}{\partial p} \right\rangle' + LW' + SW' + SH' + L_v E', \tag{3.4}$$

where the prime refers to the anomalies obtained with a 1/2 to 1/15 day^{-1} bandpass filter (see Section 3.2). Angle brackets represent mass-weighted column integration (Eq. (3.1)). The term on the left-hand side is the anomalous MSE tendency. On the right, $u\frac{\partial m}{\partial x}$ is the zonal advection of anomalous MSE; $v\frac{\partial m}{\partial y}$ is the meridional advection; $\omega\frac{\partial m}{\partial p}$ is the vertical advection; LW is the net longwave radiation flux; SW is the net short wave radiation flux; SH is the surface sensible heat flux and $L_v E$ is the surface latent heat flux. All the flux terms are positive upwards.

To elucidate the processes that lead to propagation and MSE in MLPSs, the fractional contributions to the tendency and maintenance ($\langle m' \rangle$) of anomalous MSE from each term in Eq. (3.4) are shown in Fig. 3.7. The variance contributions were defined using the following equation (Andersen and Kuang 2012):

$$C = \frac{\sum_{i=1}^{n} X_i Y_i}{\sum_{i=1}^{n} {Y_i}^2}, \tag{3.5}$$

where C refers to the percentage of variance explained by X with respect to Y; n is the total number of the grid points in the domain; X is the right-hand side terms in the budget equations; Y can be either $\frac{\partial\langle\blacksquare\rangle}{\partial t}$ (tendency) or $\langle\blacksquare\rangle$ (maintenance); $\blacksquare$ is either anomalous MSE or PKE. The contributors to tendency can be interpreted as the mechanism responsible for propagation and the contributors to maintenance correspond to intensity variations.

As is shown in Fig. 3.7, the overwhelming contribution to the MSE tendency comes from the meridional MSE advection. It peaks at day 0, and the lead and lag regressions are nearly symmetric with respect to day 0. Other terms contribute little. The relative contribution of each term to the MSE tendency changes little from day -2 to day 2.

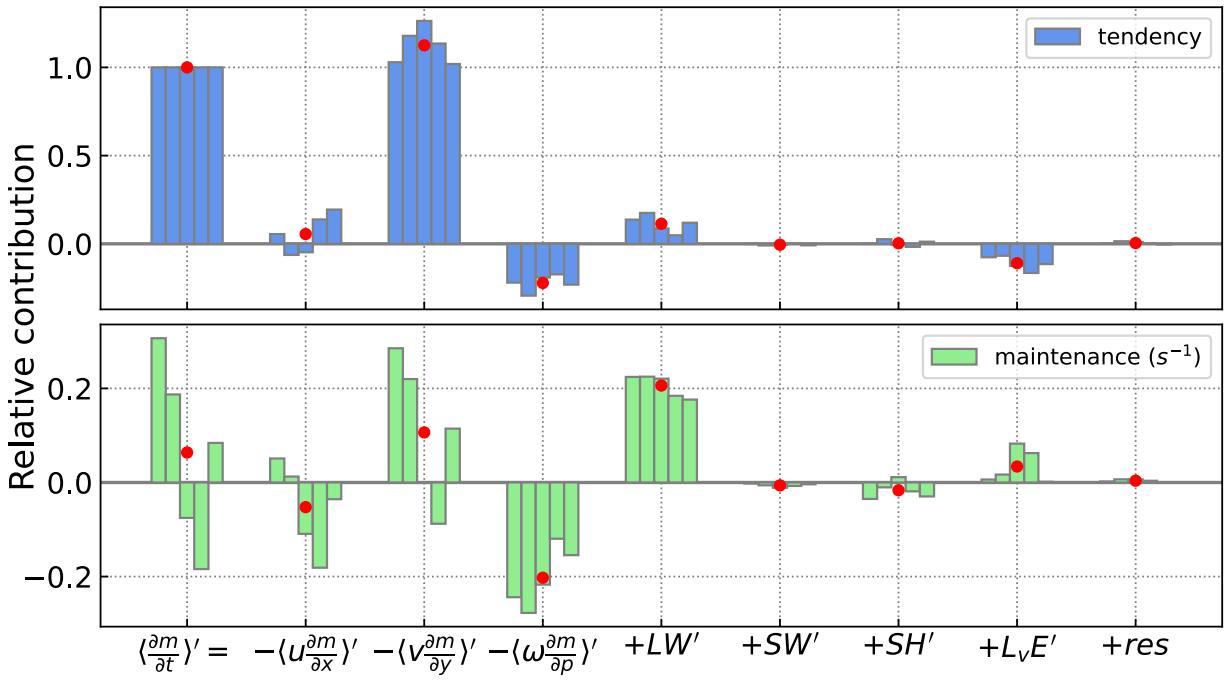

FIG. 3.7 Normalized contributions to MSE tendency (top, $\partial\langle m'\rangle/\partial t$) and maintenance (bottom, $\langle m'\rangle$) from the terms in Eq. (3.4). "res" is the residual between the left-hand side and the right-hand side. The five bins within each group represent the lag regressions at days -2, -1, 0, 1, and 2 during JJAS. The red dots are the averages of the five days. The contributions are calculated within $60-110^{\circ}E$, $10-25^{\circ}N$.

Unlike the contributions to the MSE tendency, the contributors to MSE maintenance exhibit pronounced changes from day -2 to day 2. The positive projection of MSE time tendency to the maintenance illustrates the growth and the negative represents the decay of the depressions. The system grows on day -2 and day -1. It starts weakening on day 0. The decaying process accelerates on day 1, with dissipation occurring on day 2, the same day that a new vortex forms to the east (Fig. 3.7).

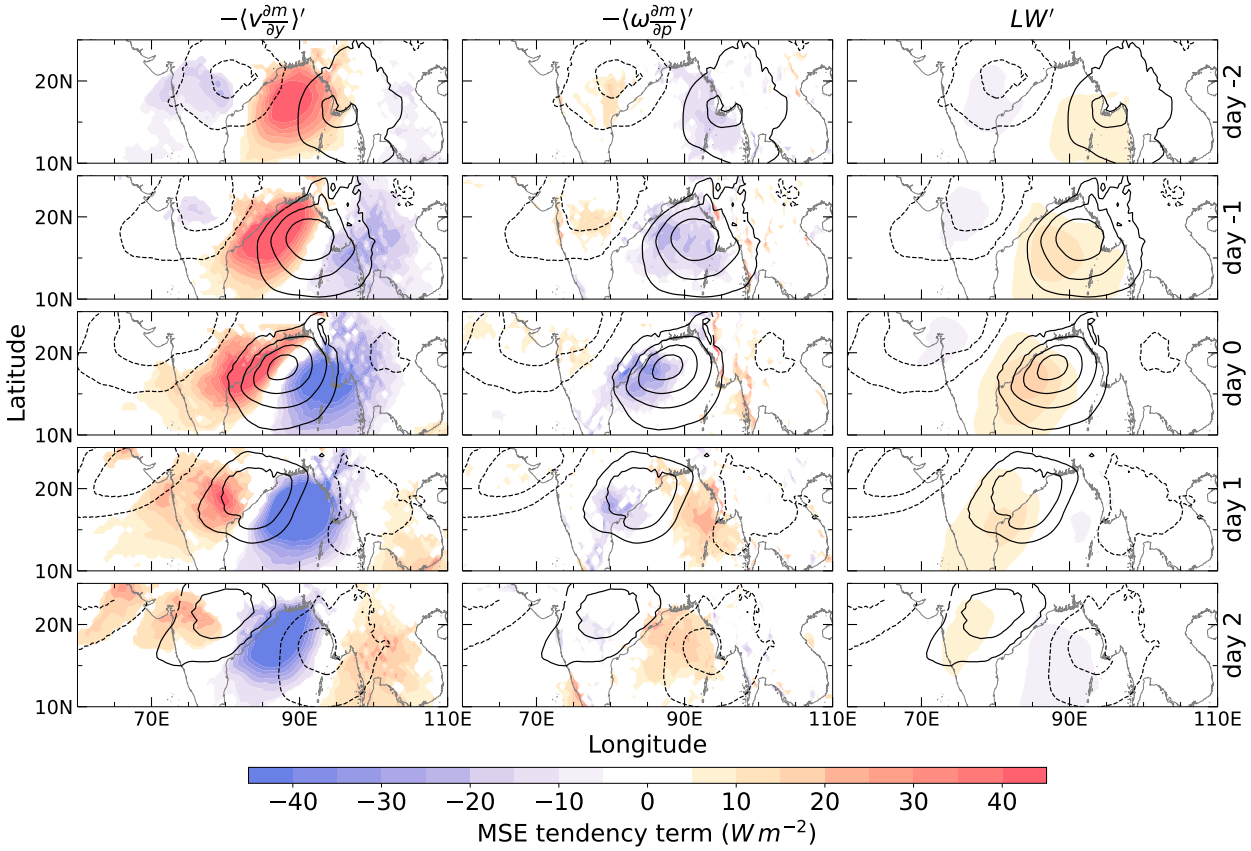

FIG. 3.8 From top to bottom, the maps are lag regressions from day -2 to day 2. From left to right, the shadings are column-integrated meridional MSE advection ($-\left\langle v\frac{\partial m}{\partial y}\right\rangle'$), vertical MSE advection ($-\left\langle \omega\frac{\partial m}{\partial p}\right\rangle'$), and longwave radiation flux anomalies (LW'). The contours are column-integrated anomalous MSE ($\langle m'\rangle$, from $-2\times10^6\,J\,m^{-2}$ to $4\times10^6\,J\,m^{-2}$ at an interval of $1\times10^6\,J\,m^{-2}$). Only statistically-significant anomalies are shown.

The leading contributors to MSE maintenance are horizontal MSE advection, vertical MSE advection, and longwave radiative heating (bottom panel of Fig. 3.7). The longwave radiative

heating contribution is due to an anomalous greenhouse effect that arises from the presence of anomalous high clouds in the MLPS, acting as an MSE source (Andersen and Kuang 2012; Wolding et al. 2016; Adames and Ming 2018b). The vertical MSE advection is an MSE sink in MLPSs because the rate of large-scale condensation exceeds the moistening by vertical moisture advection. When examined together, we see that longwave radiative heating and vertical MSE advection change little from day -2 to day 2, and approximately cancel each other out. In contrast, the horizontal MSE advection terms vary in time with the MSE tendency. During days -2, -1 and 2 the growth is predominantly determined by the meridional MSE advection, while the decay during day 0 is related to zonal MSE advection and the decay on day 1 is due to both zonal and meridional advection. Although small, surface latent heat fluxes do still contribute to MSE maintenance.

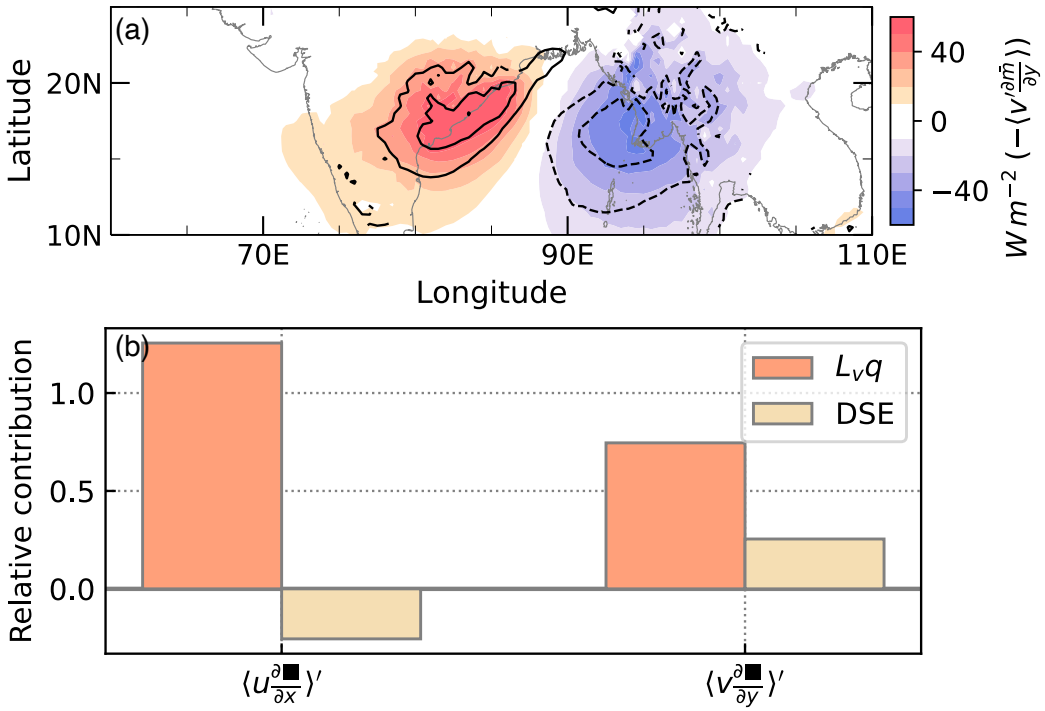

FIG. 3.9 (a): $-\left\langle v\frac{\partial m}{\partial y}\right\rangle'$ (contours, $-50\ W\ m^{-2}$ to $50\ W\ m^{-2}$ at an interval of $10\ W\ m^{-2}$) and $-\left\langle v'\frac{\partial \bar{m}}{\partial y}\right\rangle$ (shading) regressed onto MLPS index on day 0. (b): Relative contributions of the column-integrated horizontal advection of latent energy and DSE to the horizontal MSE advection.

Horizontal maps of the largest contributors to the MSE propagation and maintenance are shown in Fig. 3.8. As in Fig. 3.7, we see that the positive meridional advection of MSE shows up to the west of the enhanced MSE anomalies. The pattern colocates with the MSE tendency anomalies, corroborating that the propagation of MLPSs is largely determined by the anomalous meridional advection of MSE. Additionally, on day -2 and -1, the center of enhanced MSE anomalies have a larger overlap with the positive meridional MSE advection than with the negative advection, indicating growth of the system. The meridional MSE advection becomes negative on day 1 contributing to the decay of MLPS. We also see more clearly that the vertical MSE advection and LW' are in phase with the MSE anomalies, and tend to cancel one another.

In order to better understand how the MSE is advected horizontally, we decompose the advection into contributions from the anomalies, and from the background state, i.e. $\langle(\overline{v}+v')\,\partial_y(\overline{m}+m')\rangle$. Through this decomposition, we find that the meridional advection of background MSE by the anomalous winds governs the meridional MSE advection, making up to over 90% of it:

$$\left\langle v\frac{\partial m}{\partial y}\right\rangle' \simeq \left\langle v'\frac{\partial \overline{m}}{\partial y}\right\rangle, \tag{3.6}$$

In Fig. 3.9a we see that $v\frac{\partial m}{\partial y}$ and $v'\frac{\partial \overline{m}}{\partial y}$ are in-phase with each other. Thus, the propagation and growth of the MSE in the MLPS can be qualitatively understood by how its anomalous winds advect the monsoonal distribution of MSE. The background MSE ($\overline{m}$) is further decomposed into latent energy ($L_v q$) and DSE contributions (Fig. 3.9b). In contrast to the general circulation model results in (Adames and Ming 2018b), the anomalous moisture advection is the major contributor to the anomalous MSE advection in ERA5. The meridional latent energy advection makes up over 75% of the meridional MSE advection. The zonal latent energy advection makes up an even larger

fraction of the zonal MSE advection. Thus, the horizontal MSE advection in MLPSs is largely due to horizontal moisture displacements.

3.4.2 Perturbation kinetic energy budget

Linear regressions of column-integrated perturbation kinetic energy K' are shown in Fig. 3.10. Positive PKE is observed in association with the anomalous cyclone, implying that PKE increases with the passage of these systems. On the other hand, negative PKE is seen with the anomalous anticyclones, implying that PKE is reduced during the passage of these systems. A west-northwest propagation of the PKE anomalies is seen, consistent with the propagation of the MSE anomalies discussed previously. On day -2, the negative PKE center is seen to the northeast of the anticyclonic flow. The positive PKE is centered substantially further east of the cyclonic flow, near the South China Sea. On day -1 this center weakens and positive PKE develops to the east of the center of the anomalous cyclone. During the following days, the anomalous centers are on the northeast of the geopotential height centers. Contrary to the precipitation and MSE anomalies, the centers of PKE shift slightly northeastward of the geopotential centers, colocating within the strongest horizontal wind anomalies in the disturbances.

The column-integrated perturbation kinetic energy tendency can be split into the following terms (Maloney and Hartmann 2001; Diaz and Boos 2019a,b):

$$\frac{\partial\langle K'\rangle}{\partial t} = -\langle\bar{\mathbf{v}}\cdot\nabla_h K'\rangle - \left\langle\bar{\omega}\frac{\partial K'}{\partial p}\right\rangle - \langle\mathbf{v}'\cdot\nabla_h K'\rangle - \left\langle\omega'\frac{\partial K'}{\partial p}\right\rangle$$
$$-\langle\mathbf{v}'\cdot\nabla_h\Phi'\rangle + \langle C_b\rangle + \langle C_{bV}\rangle - \langle D\rangle, \quad (3.7)$$

where $\bar{v}\cdot\nabla_h K'$ is the horizontal advection of PKE,

$$C_b \equiv -u'v'\left(\frac{\partial \bar{v}}{\partial x}+\frac{\partial \bar{u}}{\partial y}\right)-u'^2\frac{\partial \bar{u}}{\partial x}-v'^2\frac{\partial \bar{v}}{\partial y}, \tag{3.8}$$

is the barotropic energy conversion along the horizontal plane,

$$C_{bV} \equiv -u'\omega'\frac{\partial \bar{u}}{\partial p}-v'\omega'\frac{\partial \bar{v}}{\partial p}, \tag{3.9}$$

is the vertical barotropic energy conversion,

$$\mathbf{v}'\cdot\nabla_h\Phi' = u'\frac{\partial \Phi'}{\partial x}+v'\frac{\partial \Phi'}{\partial y}, \tag{3.10}$$

is the geopotential advection by the anomalous horizontal winds, indicating the work done by the pressure gradient force (Diaz and Boos 2019b). D' is the sum of friction and other processes. Since we are unable to calculate the friction using reanalysis data, we put friction and other processes that cannot be inferred from the current dataset into the residual ("res") between the left and right-hand side. The relative share of each term is shown in Fig. 3.11 calculated following Eq. (3.5).

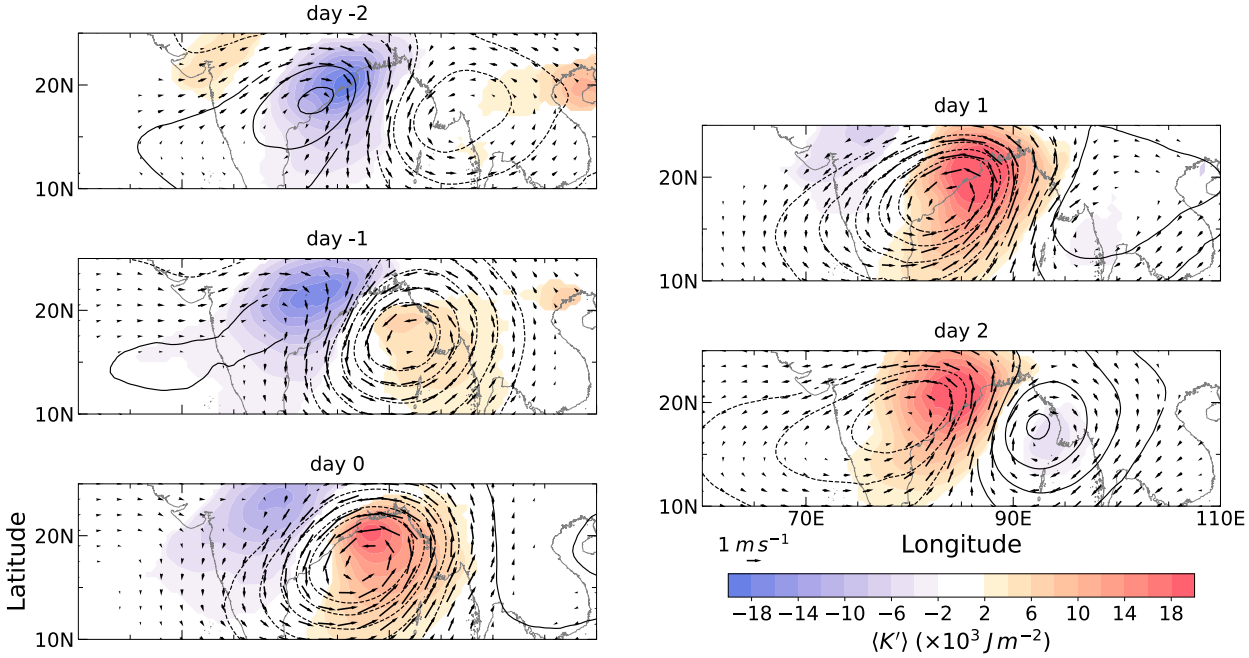

FIG. 3.10 Lag regressions from day -2 to day 2 of column-integrated perturbation kinetic energy anomalies (shadings), geopotential height (contours, from -4 gpm to 4 gpm at an interval of 1 gpm), and winds (vectors) at 500 hPa onto the MLPS index. Only statistically-significant anomalies are shown.

As shown in Fig. 3.11, the major contributors to the PKE tendency are the horizontal advection of anomalous geopotential by the wind anomalies ($v' \cdot \nabla_h \Phi'$), and the residual. The budget residual projects positively to the PKE tendency, indicating that the residual is not only a result of dissipation but may also be the result of processes that are unsolved in the reanalysis data, possibly related to subgrid-scale processes (Diaz and Boos 2019b) or convective systems and internal gravity waves caused by mountains (Alaka and Maloney 2014; Chen et al. 2016). The other terms have relatively small values. The horizontal advection of PKE by anomalous winds, however, shows a non-negligible increase on day -2 and day 2 and a decrease on day 0. The leading terms to the maintenance of K' are the horizontal barotropic energy conversion, horizontal advection of geopotential anomalies and the residual. The horizontal and vertical advection by anomalous winds serves as small but non-negligible sinks of PKE.

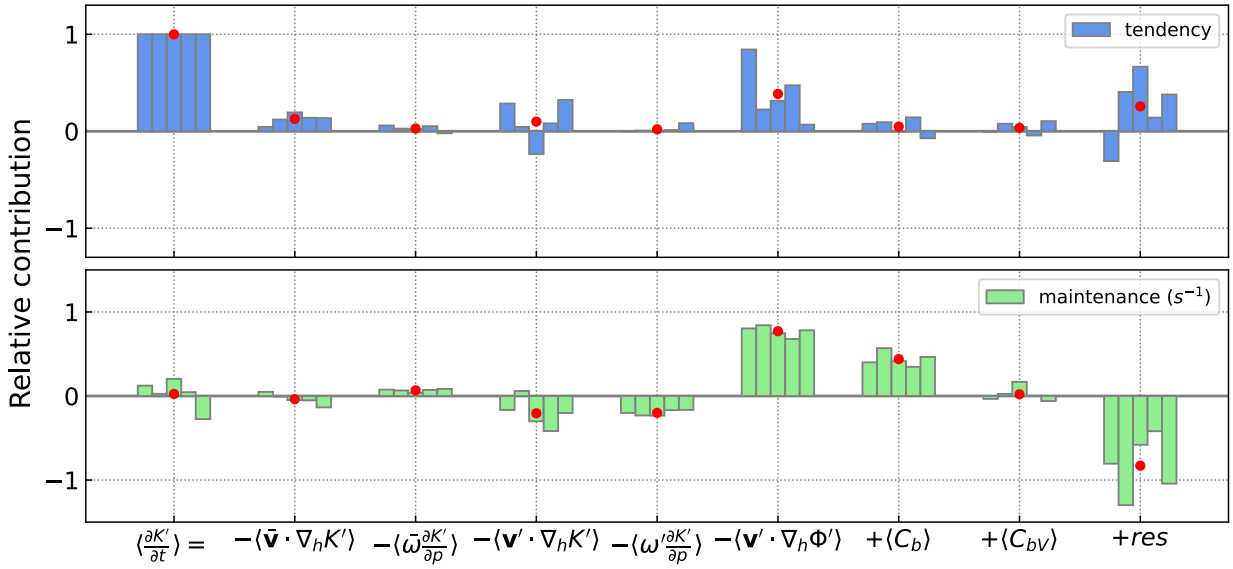

FIG. 3.11 Normalized contributions to PKE tendency (top, $\partial \langle K' \rangle / \partial t$) and maintenance (bottom, $\langle K' \rangle$) from the terms in Eq. (3.7). "res" refers to the residual between left-hand side and right-hand side of Eq. (3.7). The five bins within each group represent the lag regression at days -2, -1, 0, 1, and 2. The red dots are the averages of the five bins. The contributions are calculated within $60 - 110°E$, $10 - 25°N$.

The barotropic term is shown in the leftmost column in Fig. 3.12. The locations of negative and positive centers of the barotropic term are identical to the PKE (contours). A strong negative barotropic conversion initiates at the east coast of India and the western Bay of Bengal on day -2, collocated with an anti-cyclonic anomalous flow. The pattern indicates that kinetic energy transports from eddies to the mean state in the anti-cyclonic anomalies. As the negative center moves northwestward, a weak positive center (transporting kinetic energy from mean state to disturbances) forms and grows in the north Bay of Bengal. On day 2, the positive center moves to north India and the negative center disappears.

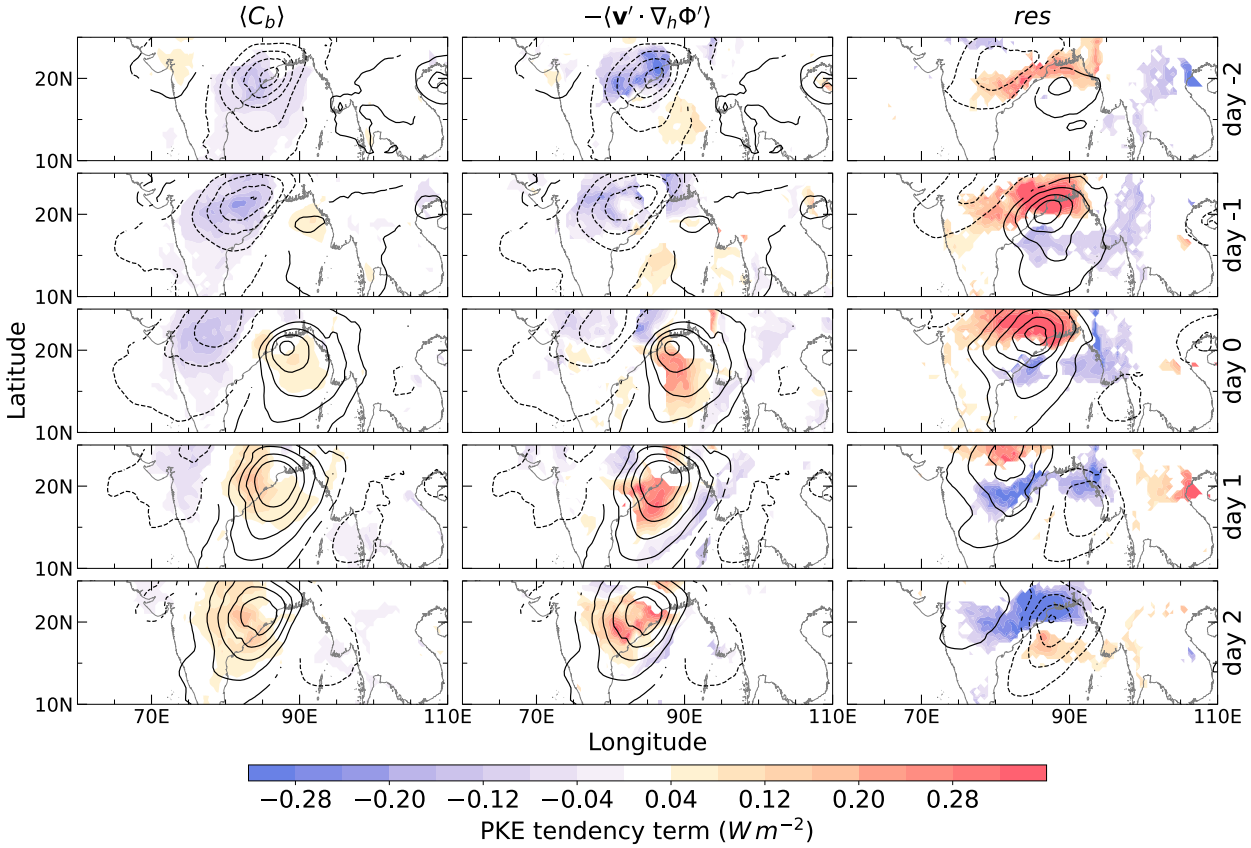

FIG. 3.12 From top to bottom, the maps are lag regressions from day -2 to day 2. From left to right, the shadings are column-integrated horizontal barotropic term ($\langle C_b \rangle$), horizontal geopotential advection ($-\langle v' \cdot \nabla_h \Phi' \rangle$), and residual ($res$). The contours in the rightmost column are the tendency of column-integrated PKE ($\frac{\partial \langle K' \rangle}{\partial t}$ from $-18 \times 10^3\ W\,m^{-2}$ to $18 \times 10^3 W m^{-2}$ at an interval of $4 \times 10^3\ W\,m^{-2}$), the contours in the rest of the panel are the column-integrated PKE ($\langle K' \rangle$ from $-0.2\,J\,m^{-2}$ to $0.25\,J\,m^{-2}$ at an interval of $0.05\,J\,m^{-2}$). Only statistically-significant anomalies are shown.

The horizontal advection of anomalous geopotential by the wind anomalies is shown in the middle column of Fig. 3.12, which can be viewed as the work done by the pressure gradient force (Diaz and Boos 2019b). From the examination of the composites, it is clear that this term is nearly always in phase with the PKE (contours). Given that the non-divergent component of the winds is parallel to the isobars in MLPSs (Fig. 3.3), it follows that the positive $\langle v' \cdot \nabla_h \Phi' \rangle$ anomalies are the result of the strong divergence that is associated with the anomalous convection that is located near the center of the anomalous cyclones and anticyclones (Figs. 3.3 and 3.5).

The residual is shown in the rightmost column of Fig. 3.12. The pattern exhibits more northward propagation than westward propagation. The enhanced residual centers are to the south of the negative PKE tendency and to the north of the positive PKE tendency.

3.5 Discussions and conclusions

In this study, we created an MLPS index by filtering precipitation data to retain westward-propagating wavenumbers from 3 to 25, and frequencies between 1/2 to 1/15 day^{-1}, and averaging over the head of the Bay of Bengal. The index was used to create lag regressions that elucidated the structure of MLPSs and their governing processes. The regression results were then compared with three theories that have been posited to explain MLPS growth and propagation: dry barotropic, baroclinic, and moisture-vortex growth. The consistency between observations and theories is summarized in Table 3.1.

We found that none of the theories alone are capable of explaining all the features we found in MLPSs. However, most of them are consistent with the combination of barotropic and MVI-like growth. Thus, we posit that these two mechanisms could be potential explanations for MLPS growth and propagation. Evidence for this statement can be found by revisiting the MSE and PKE

budgets. As seen in Fig. 3.7, the meridional advection of mean MSE by anomalous winds is vital to both propagation and growth of the MSE anomalies. Longwave radiative heating is also important to the maintenance of MSE, in both MLPSs and other slow-propagating convectively-coupled systems across the tropics (Yasunaga et al. 2019; Andersen and Kuang 2012; Mayta et al. 2022). However, this positive feedback is balanced out by the vertical advection of MSE. The anvils caused by the vertical motion suppress the outgoing longwave radiation and hence compensate for the MSE sink from vertical MSE advection (Andersen and Kuang 2012; Adames and Ming 2018b; Inoue et al. 2020). So only when horizontal MSE advection is considered can we explain the growth of MSE within MLPSs. The contributions from horizontal MSE advection to maintenance is approximately equal to the projection from MSE tendency. A positive projection of MSE tendency to maintenance implies an increase in MSE, a negative projection indicates a decrease.

TABLE 3.1 A summary of the features in MLPSs documented in this study and which growth process is consistent with.

Observed Features	**MVI-like**	**Dry Barotropic**	**Moist Baroclinic**
Upright vertical structure	Yes	Yes	No
Tilts against horizontal shear	No	Yes	No
Synoptic horizontal scale of ~1000 km	Yes	Yes	Yes
Moisture, precipitation and vorticity have an in-phase component	Yes	No	No
MSE anomalies follow the contours of mean MSE	Yes	No	Yes
Meridional MSE advection important for MSE growth	Yes	No	Yes
Barotropic energy conversion important for PKE generation	No	Yes	No
PKE generation through downgradient geopotential advection	Yes	No	Yes

The examination of the PKE budgets shows that the barotropic conversion from the horizontal shear is important for the maintenance of PKE in MLPSs. The downgradient advection of anomalous geopotential, on the other hand, cannot be explained with barotropic growth. The non-divergent component of horizontal winds in MLPSs are approximately geostrophic or gradient wind balance and tends to be parallel to the isobars (Adames 2022). In the absence of convection, these winds can induce barotropic growth but exhibit a negligible downgradient advection of anomalous geopotential. In MVI, however, winds that blow down the pressure gradient would be explained by the irrotational flow that is brought about by the existence of convection near the center of the MLPS. Thus, this contribution to the PKE maintenance likely comes from MVI-like processes. Together, barotropic energy conversions and downgradient winds can generate enough PKE to maintain MLPSs against sinks.

With barotropic and MVI-like growth being consistent with most of the features of MLPSs, it follows that baroclinic growth does not need to be invoked. Further, most of the features of MLPSs disagree with this type of growth, such as the upright structure, and colocating of water vapor, rainfall and vorticity. This result supports previous works that have posited that baroclinic growth is of little importance to MLPSs (Cohen and Boos 2016; Adames 2021).

It is worth noting that the moist barotropic instability mechanism proposed by Diaz and Boos (2019b) has many similarities to MVI. Diaz and Boos (2021a) also posit that meridional MSE advection is essential to MLPS growth. In a way, moist barotropic instability can be viewed as a combination of MVI and dry barotropic instability. Hence, we do not discuss this growth mechanism in Table 3.1 but acknowledge that it can also explain the observed features of MLPSs.

3.5.1 Caveats and future work

There are a few caveats in this study. Though residuals exist in both MSE and PKE budgets, their contributions are different. The MSE budget residual is negligibly small. The PKE budget residual, however, is significant. It functions as a sink of PKE but acts to propagate the PKE northwestward. Frictional dissipation could be the reason for the vortex decay. Sub-grid scale processes that are not well-represented in ERA5, such as convective momentum transports, could account for the contribution to propagation (Chen et al. 2016). Also, the residual may be a result of numerical errors due to the complex topography of the region.

Because we used linear regression to understand MLPSs, our analysis does not account for nonlinearities that may be present in individual systems. Also, the index and the linear regressions emphasize the weaker MLPSs and not the stronger monsoon depressions. The stronger depressions differ from MLPSs in that latent heat fluxes are also important for the growth of depressions (Fujinami et al. 2019; Diaz and Boos 2021b).

In this study, we only present evidence that MSE advection is a key factor in MVI-like growth. Recent work has indicated that the disturbances that grow from MVI extract latent energy from the background circulation (Mayta and Adames Corraliza 2023; Adames Corraliza and Mayta 2023). Extending the results to this study would lead to the hypothesis that MLPSs extract latent energy from the Indian monsoon, thereby weakening it. Testing this hypothesis will be the focus of next chapter.

3.6 Appendix

3.6.1 Index sensitivity test

Empirical orthogonal function analysis is applied over the domain shown in Fig. 3.13. EOF1 explains 14.3% of the total variance and the pattern is similar to the disturbance growth (day -1 in Fig. 3.3). EOF2 explains 13.6% of the variance and is similar to the pattern of decay on day 1.

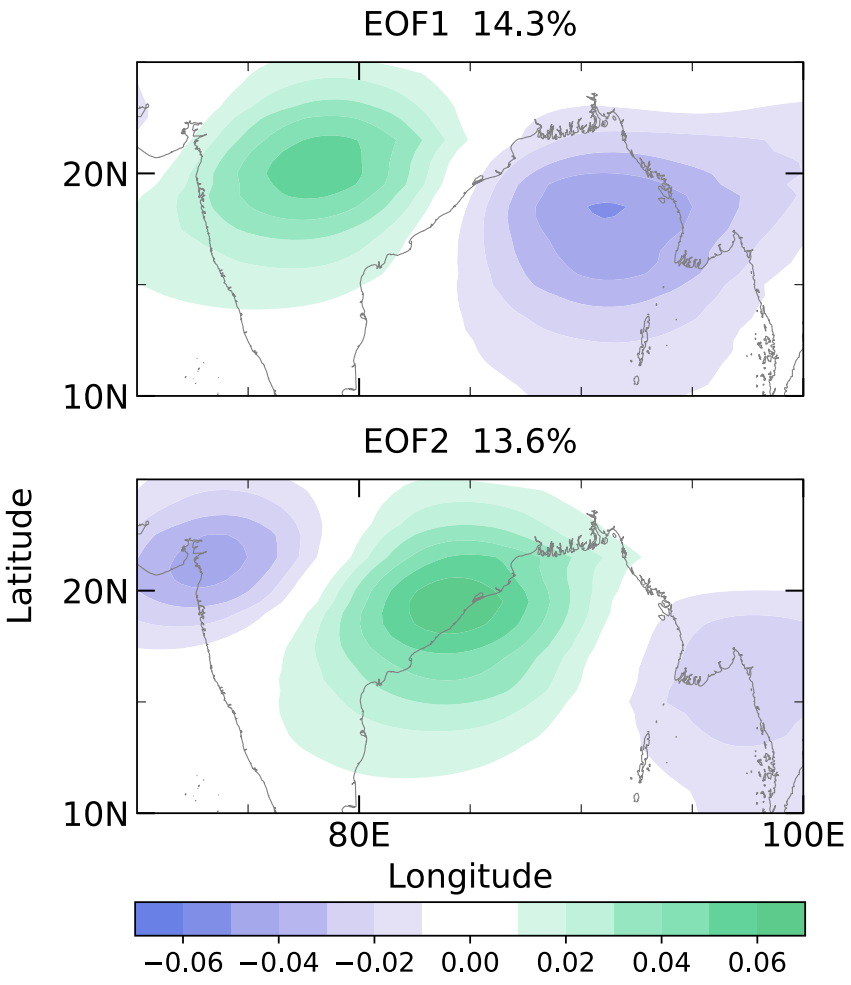

FIG. 3.13 The leading two EOFs of the filtered precipitation anomalies.

The filtered mean sea-level pressure, averaged over the head of Bay of Bengal (red box in Fig. 3.2) was also tested as an index (Fig. 3.14). The disturbance has the same growth and propagation features as the one with precipitation as its index but has a relatively smaller magnitude in rainfall but stronger winds and geopotential anomalies.

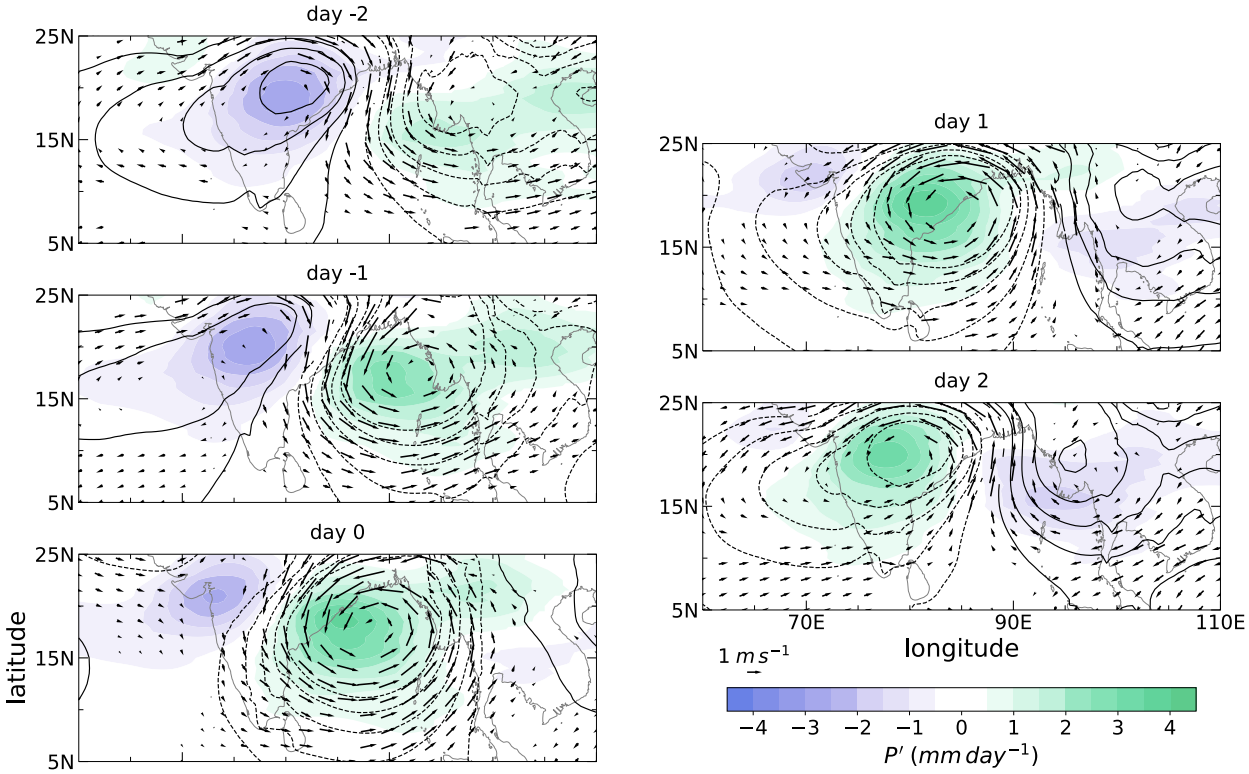

FIG. 3.14 Same as Fig. 3.3 but using filtered mean SLP as the MLPS index.

Chapter 4 Interactions of Monsoon Low Pressure Systems and Indian Monsoon during Growth from Moisture-vortex Instability

manuscript in preparation for submission

4.1 Introduction

In the previous chapter, we have introduced some observed features of the monsoon low pressure systems. The monsoon low pressure systems (MLPSs) are shown to grow from the moisture-vortex instability (MVI) and barotropic instability. The analysis of MSE budget indicates that the major contributor to the propagation and growth is the meridional eddy advection of climatological mean moist static energy (MSE) (Adames and Ming 2018b), which is in accordance with the MVI theory. It was also pointed out that the anomalous moisture colocates with anomalous MSE, indicating that the latent heat is an essential component of MSE. These features are consistent with the moisture modes (Neelin and Yu 1994). A straightforward definition of the moisture mode is a system in which moisture dominates its thermodynamics.

In the last chapter, however, we did not show the intensity variation of the Indian monsoon when the mean MSE is advected by anomalous winds during the growth of MLPSs from MVI. In this chapter, based on the moisture mode theory, we can now investigate the wave-mean-flow interactions through a "moisture mode activity". In a recent study by Adames Corraliza and Mayta (2023, AM23 hereon) the interactions between the large-scale moisture modes and the Hadley Cell was analyzed using a moist two-layer model. It is posited that the moist waves weaken the Hadley Cell as they grow from MVI. The moisture is advected against the background mean meridional

moisture gradient. In the previous chapter, we have seen that the mean MSE advected by the anomalous meridional wind plays the leading role when growing from MVI (Fig. 3.7 and Eq. (3.6)). So the climatological mean MSE can be seen as an energy source and the mean MSE gradient can be viewed as a representation of the Indian monsoon intensity. Following the track, in this chapter, we hypothesize that the MLPSs enhance at the expense of the Indian monsoon during MVI-like growth.

This chapter is structured as follows: data and methods are shown in Section 4.2. The moisture mode criteria are examined in Section 4.3. A two-layer model and AM23 are revisited in Section 4.4. The interaction of the Indian monsoon and MLPSs is analyzed using reanalysis data in Section 4.5. Section 4.6 is the concluding remarks.

4.2 Data and methods

4.2.1 Reanalysis data

The 6-hourly data comes from the European Centre for Medium-Range Weather Forecasts (ERA5, (Hersbach et al. 2019)). The dataset is from 1980 to 2019, with a horizontal resolution of $0.5° \times 0.5°$, 27 levels in the vertical direction from 1000 to 100 hPa.

4.2.2 Linear regressions

Linear regressions onto an MLPS index are the main approaches in this study. As in the previous study, the index was generated through filtered precipitation (Luo et al. 2023). The frequency band of the filter is from $\frac{1}{15}$ to $\frac{1}{2}$ day^{-1}. The wavenumber band of the filter is from -3 to -25, with a negative sign representing westward propagation. The band-pass filter selected the

maximum signal in the frequency-wavenumber domain over South Asia (Wheeler and Kiladis 1999; Wheeler et al. 2000; Adames and Ming 2018b). The filtered data are used as the temporal deviations and are referred to as "anomalies" or "anomalous fields" in this study. The filtered precipitation was then regionally averaged over the head of the Bay of Bengal (BoB, $15-20°N$, $85-90°E$), the area where the initiations of MLPSs are the most dense (Krishnamurthy and Ajayamohan 2010; Boos et al. 2016). For an arbitrary variable X, its temporal anomalies, marked as X', went through the same band-pass filter.

The regression coefficients were obtained through the least square approach and tested using a two-tailed t-test (Davis 1978; Adames and Wallace 2014) based on an effective degree of freedom (Chen 1982). All the regressions shown in this study are statistically significant on a 95% level.

The moisture fields are vertically integrated from the surface to the top of the disturbances for the arbitrary variable X as the following Adames and Ming (2018a) and Luo et al. (2023):

$$\langle X \rangle = -\frac{1}{g}\int_{p_s}^{p_t} X\, dp, \tag{4.1}$$

where $\langle\ \rangle$ refers to the column-integration, $g = 9.8\ m \cdot s^{-1}$ is the gravitational acceleration, $P_t = 100$ hPa and $P_s = 1000$ hPa are defined as the top and surface of the disturbance.

As in AM23 but to distinguish from annotations for temporal anomalies, we denote the zonal averages and deviations as follows:

$$\tilde{X} = \frac{1}{lon_E - lon_W}\int_{lon_W}^{lon_E} X\, dlon, \tag{4.2}$$

where lon_W is the longitude of the west border and lon_E is the east border. The meridional average is defined as follows:

$$[X] = \frac{1}{lat_N - lat_S} \int_{lat_S}^{lat_N} X \, dlat, \tag{4.3}$$

4.3 Moisture mode

4.3.1 Revisit of moisture mode theory

The story starts with our desire for simulating the movement of the atmosphere. Based on Newton's laws of motion, we formulated the basic general circulation models. The primitive numeric models showed better performance in simulating the large-scale motions than smaller-scale processes such as cumulus convection. So the processes with smaller scales are represented by parameters. That is called "parameterization". However, the parameterization varies due to the complexity of the physics. Different parameterization schemes were then proposed based on different perspectives and assumptions. One of the most popular schemes for cumulus convection in the late 1900s was proposed by Manabe et al. (1965) in which they adopted the "moist convective adjustment" for the first time. They assumed that moisture and temperature in a convective system are adjusted by convection to reach a state in which their sources and sinks are quasi-equal. But the timescale for such adjustment was assumed to be instant in their scheme. Betts (1986); Betts and Miller (1986) then amended the scheme by introducing the relaxation time, allowing for a longer timescale in the adjustments. The improvement makes the scheme applicable to more types of systems. It is called "Betts-Miller" scheme and has been used widely since then.

By investigating the primitive equations that incorporate the "Betts-Miller" moist convection adjustment parameterization, Yu and Neelin (1994) found that one of the solutions to the formula that has low wavenumbers has been dominated by moisture component and decay fast in the convective timescale. The moisture and energy budgets showed that variations in

temperature are small comparing to the moisture variation. They define such system as the "moisture mode".

With more evidence of the coupling between moisture and convection being documented in the past two decades (Sobel 2002; Bretherton et al. 2004; Sherwood et al. 2004; Holloway and Neelin 2009; Ahmed and Schumacher 2015; Rushley et al. 2018), the concept of moisture mode is catching more attention. The moisture mode theory was applied to study the tropical motion systems, such as the Madden-Julian oscillation (MJO) (Maloney et al. 2010; Sobel and Maloney 2012, 2013; Pritchard and Bretherton 2014; Adames and Kim 2016). The targets are often have a larger scale than the convections, which is contrary to the limitations in Yu and Neelin (1994). That is due to the application of weak-temperature gradient (WTG) approximation.

To better understand the atmospheric dynamics, simplification of basic equations is necessary. Assumptions are used to remove the noise in the physical processes. The weak-temperature gradient approximation was developed for the examination of moisture-dominated systems which also have comparable divergent flow as the rotational flow (Sobel et al. 2001; Sobel 2002). The WTG approximation is also called as WTG balance because it states the balance between the diabatic heating and, the vertical advection of dry static energy (potential temperature was used initially), a representation of the adiabatic cooling. The gravity wave is removed when a system reaches WTG balance (Sobel 2002). When applying the WTG approximation to the moisture mode, moisture mode was found not only in convective scale, but also in the larger scales (Sobel 2002; Sobel and Bretherton 2003; Ahmed et al. 2021).

Classification of the large-scale tropical waves according to the key factors in their thermodynamics became an intuitive next step since moisture mode is not limited to convective-scale development. They were generally separated into two scenarios: waves that are dominated

by moisture variations and waves that are dominated by temperature variations (Yasunaga et al. 2019; Inoue et al. 2020). The latter eventually evolves into gravity waves. Recently, Adames et al. (2019) provided a continuum view from the moisture mode group to the gravity wave group by pointing out the existence of mixed waves of the two scenarios.

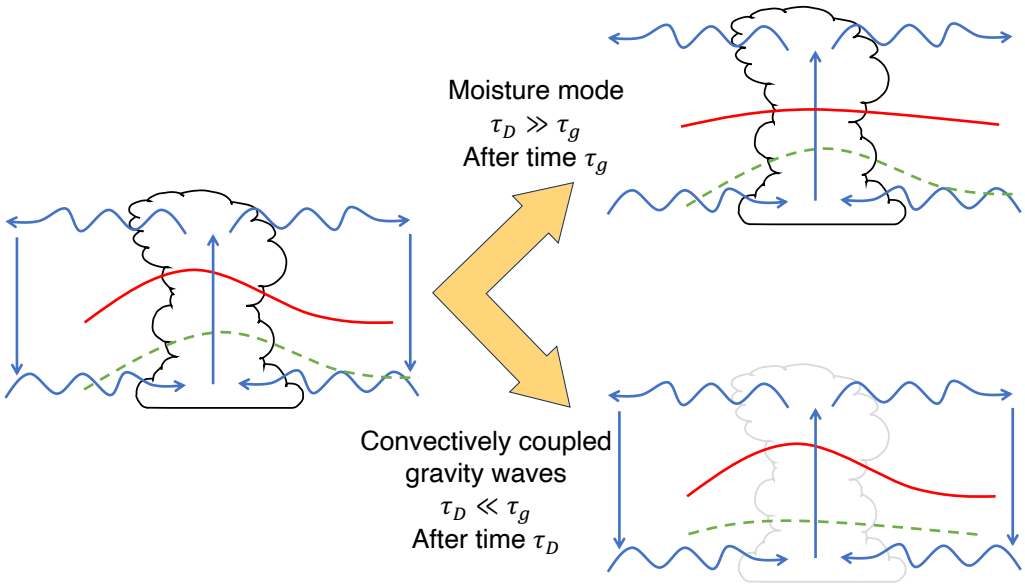

FIG. 4.1 Schematic description of moisture mode condition (top) and non-moisture mode condition (bottom). The red solid curves are the horizontal temperature profiles, the green dashed curves are the horizontal moisture profiles. The blue wavy and straight arrows are the gravity wave circulations. When $\tau_D \gg \tau_g$, the gravity waves redistribute as they propagate. Temperature is then homogenized and the system is in WTG balance. The moisture peak has not been removed by the convection. When $\tau_D \ll \tau_g$, the convection shuts down, moisture is flattened due to the convection. The system is then dominated by temperature and fails to reach WTG balance, only gravity waves left.

A schematic plot showing the moisture mode and convectively coupled gravity wave conditions, is in Fig. 4.1, where τ_g is the gravity wave adjustment time scale or the WTG adjustment time scale (Ruppert and Hohenegger 2018; Adames et al. 2019). τ_D is the drying timescale by convection. In the moisture mode condition, gravity waves redistribute the energy from convection, flatten the horizontal temperature profile and adjust to the WTG balance before it is dried out by the convection (Adames and Maloney 2021; Adames 2022). So the system is controlled by moisture instead of temperature. In the gravity wave regime, the convection dries

the disturbance by transforming moisture into precipitation. Then the convection ceases, the gravity wave and temperature variation left. The gravity wave modulates temperature through adiabatic lifting and generates new convection.

4.3.2 Criteria for moisture mode

1). In a moisture mode, the dry enthalpy ($|C_pT'|$) is greatly smaller than the latent energy ($|L_vq'|$). Adames et al. (2019) used a dimensionless number N_{mode} to quantify the relative importance of moisture to temperature in a system:

$$N_{mode} \equiv \left|\frac{C_pT'}{L_vq'}\right|, \tag{4.4}$$

where $C_p = 1004\,J\cdot(K\cdot kg)^{-1}$ is the heat capacity at constant pressure, T' is anomalous temperature, $L_v = 2.5\times10^6\,J\cdot kg^{-1}$ is the specific latent heat and q' is anomalous specific humidity. $|\cdot|$ represents the absolute value. Eq. (4.5) explicitly shows that when $N_{mode} \ll 1$, the moisture is dominant, indicating that the system is a moisture mode. When $N_{mode} \simeq 1$, the contributions from moisture and temperature are equivalent, the wave is a mixed wave. When $N_{mode} \gg 1$, the temperature governs the thermodynamics. Using the scale analysis, N_{mode} can be transformed into the following format:

$$N_{mode} \simeq \frac{c_p^2\tau_\omega}{c^2\tau_c}, \tag{4.5}$$

where $c_p \simeq 6.7\,m\cdot s^{-1}$ refers to the phase speed of the MLPSs. It can be obtained from the slope of Fig. 4.2. $c \simeq 50\,m\cdot s^{-1}$ is the phase speed of free gravity wave, $\tau_c \simeq 12\,hrs$ is the convective moisture adjustment time scale. It can be calculated from the regression coefficient of column

moisture anomalies and precipitation anomalies ($\tau_c = \frac{\langle q' \rangle}{P'}$, Fig. 4.3a). $\tau_\omega \simeq 4\ days$ is the temporal scale of the wave. It can be obtained from Fig. 4.3.

Eq. (4.5) states that if a wave propagates slowly enough and needs long enough time to turn moisture into rainfall, it tends to be a moisture mode (Fig. 4.1). For MLPSs, $N_{mode} \simeq 0.15$, which is consistent with moisture mode.

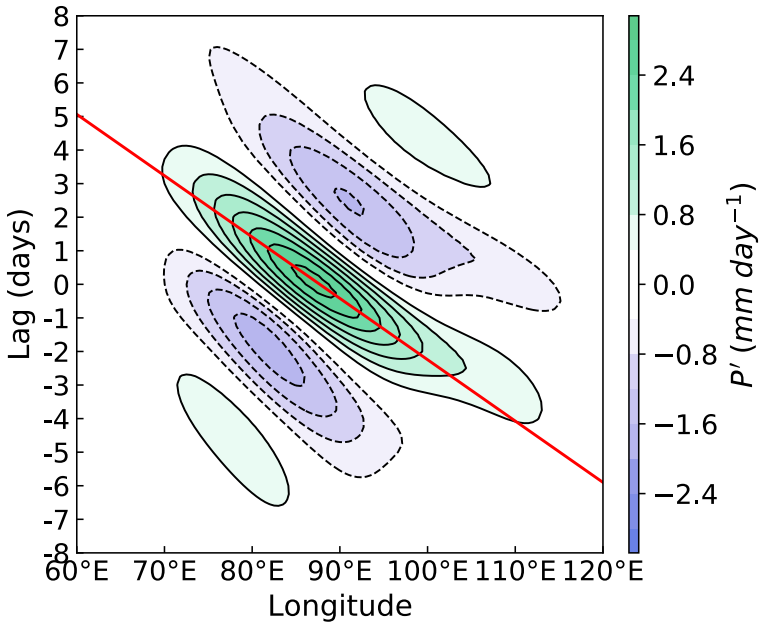

FIG. 4.2 Longitude-time diagram of precipitation anomalies in ERA5. A least-square linear fit is shown as a red line.

Apart from N_{mode}, another set of criteria was proposed by Ahmed et al. (2021). According to the summary of Mayta et al. (2022), the criteria can be described as follows:

2). The column moisture anomalies ($\langle q' \rangle$) should be highly correlated with the precipitation anomalies (P'):

$$P' \propto \langle q' \rangle, \tag{4.6}$$

3). The system should be in weak-temperature gradient balance. The adiabatic cooling should be equal to diabatic heating (Sobel and Bretherton 2000; Sobel et al. 2001; Adames 2022):

$$\left(\omega\frac{\partial s}{\partial p}\right)' \simeq Q_1', \tag{4.7}$$

$$\langle Q_1\rangle' = LW' + SW' + SH' + L_vP', \tag{4.8}$$

where $s = C_pT + \Phi$, Φ is geopotential, ω is the vertical wind, Q_1 is diabatic heating, LW refers to the longwave radiation flux, SW is the shortwave radiation flux, SH is surface sensible heat flux and L_vP is the latent heat flux.

By combining the mass continuity equation, the criterion turns into the balance between the anomalous divergence of DSE flux and anomalous apparent heating rate:

$$\nabla\cdot\langle s\,\boldsymbol{v}\rangle' \simeq \langle Q_1\rangle', \tag{4.9}$$

4). The anomalous latent heat should significantly outweigh anomalous DSE:

$$|L_vq'| \gg |s'|, \tag{4.10}$$

Fig. 4.3a shows the distribution of $\langle q'\rangle$ and P'. The correlation coefficient between precipitation and column moisture is as high as 0.852. The regression coefficient is 2 day^{-1}, which is the reciprocal of $\tau_c = 12\,hrs$. Fig. 4.3b shows a regression coefficient of 0.871, indicating that the system is in WTG balance. Fig. 4.3c shows that the regression coefficient of column latent heat anomalies and MSE anomalies ($m' = s' + L_vq'$) is close to 1 indicating that the moisture is leading the variations in the thermodynamics. So far, MLPSs satisfied all the criteria for being a moisture mode.

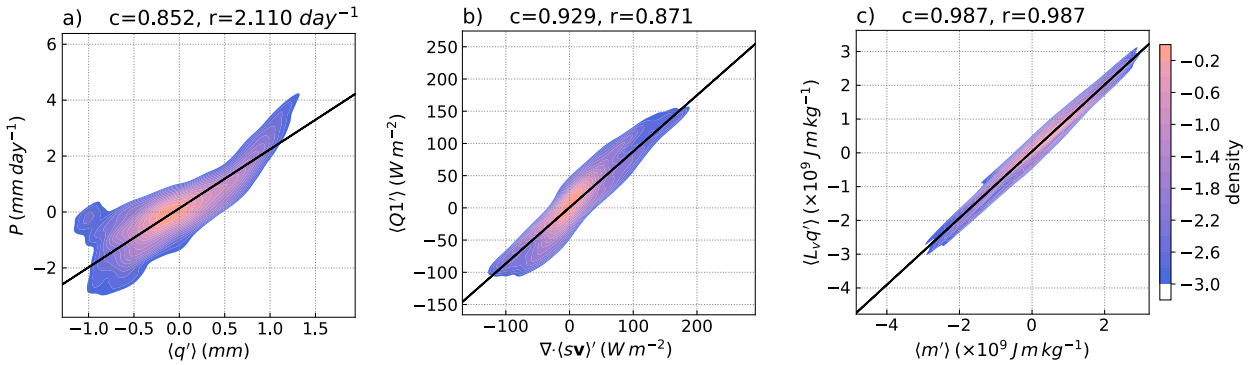

FIG. 4.3 Scatter plots showing the three moisture mode criteria. The contour shows the kernel-density estimate of scatters in the form of a natural logarithm based on a Gaussian kernel. The estimator bandwidth of the kernel was calculated using Scott's rule (Scott 1979). Higher values in the colorbar represent denser points. The black line refers to a linear fit based on the least square method between the x and y-axis. "c" in the title is the correlation coefficient, "r" in the title is the regression coefficient or the slope of the fit.

4.4 A linear framework, review of AM23

In order to understand the activity of the MLPSs and their interactions with the Indian monsoon with the presence of MVI, we used a two-layer model (Adames 2021) with prognostic water vapor as in AM23. The model is originally from Holton and Hakim (2013b). The surface boundary layer is at 1000 hPa, the top boundary is at 100 hPa, the layers are sliced evenly according to pressure into two major layers with two minor layers in each of them.

The model was designed and modified as a simplified representation of the Indian monsoon, in which the streamfunction and the column moisture are intertwined by the polarization relation so that the moisture mode can grow from the meridional moisture advection. Different from traditional models, the WTG approximation, instead of the quasi-geostrophic (QG) approximation was adopted for the systems in the model so that the system can be a moisture mode. A schematic plot of the two-layer model in the Indian monsoon environment is shown in Fig. 4.4.

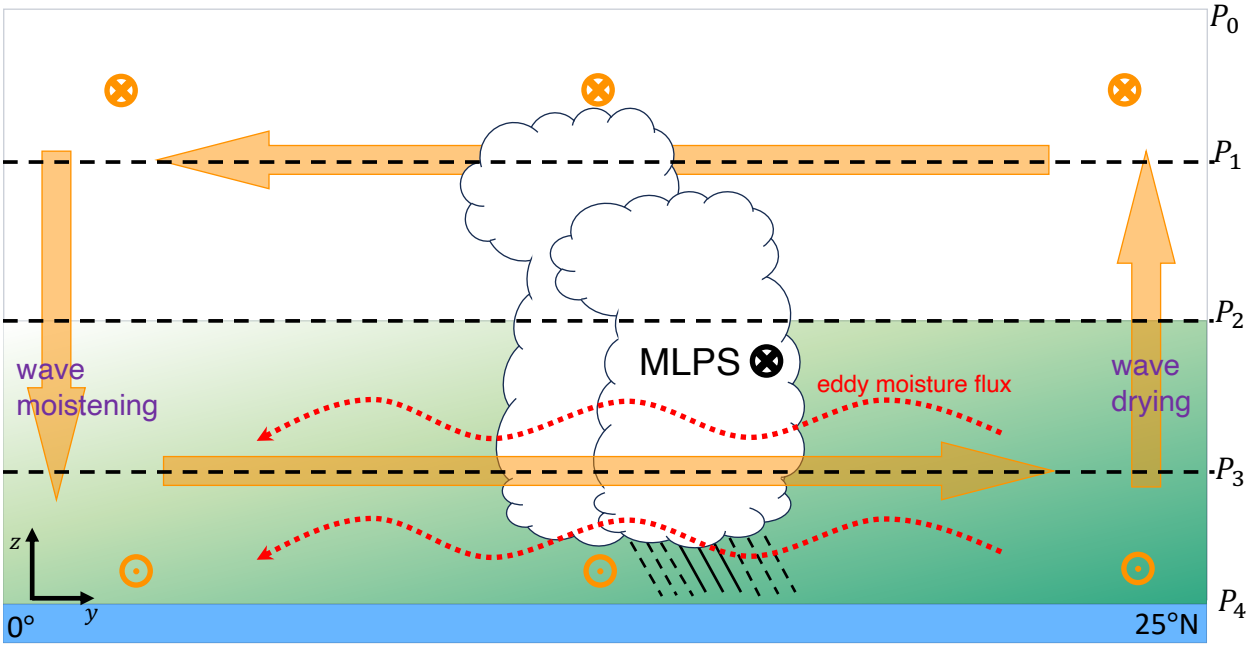

FIG. 4.4 Schematic of the two-layer model. The dashed black lines are the boundaries of layers. P_2 is the boundary of the two major layers, the top layer and bottom layer. P_1 and P_3 are the boundaries of sub-layers at top and bottom layers, respectively. The green shading at the bottom layer represents the column water vapor. The darker the shading is, the more moisture it has. The moisture increases linearly from south to north. The yellow arrows and markers refer to the mean winds. Southwesterlies are at the bottom layer and northeasterlies are at the top layer. Ascending flow is in the north and subsidence is in the south. The monsoon low pressure systems are placed in the middle, marked by clouds and precipitation. They propagate westwards. The red dashed lines are the eddy moisture flux. It goes against the background moisture gradient, and moistens the air in the south while dries the air in the north.

To represent the Indian monsoon, the mean meridional winds at the bottom layer are southerlies and switch to northerlies at the top layer. The mean zonal winds are westerlies at the bottom layer and easterlies at the top layer. The parameters were calibrated according to the values calculated from ERA5 data. The speed of westerlies was set as $5\ m \cdot s^{-1}$ at layer P_3. Since MVI only exists in an environment where moisture colocates with vorticity at the lower troposphere, prognostic moisture was also included at the bottom level, with a steady poleward meridional column moisture gradient ($\frac{\partial \widetilde{\langle q \rangle}}{\partial y}$) of $5 \times 10^{-6}\ kg \cdot m^{-3}$. The cloud radiative feedback is set as 0.5, gross dry stability is set as $10^8 J \cdot m^{-2}$. The convective moisture adjustment time scale τ_c is 12 hours. The initial state of streamfunction is set at the scale of $10^5 m^2 \cdot s^{-1}$. Zonal wave number is

8 and meridional wave number is 1. Width of the region is 3000 km. The latitudinal distortion in grids is assumed to be negligible in this model.

By using the model, we propose that when MLPSs grow from MVI, an equatorward eddy moisture flux occurs. The moisture flux tries to homogenize the monsoonal moisture distribution and thus weakens the Indian monsoon.

As shown in AM23, the model has two solutions, a growing wave and a decaying wave. Only the growing wave is discussed in this study. The relationships between growth rate, phase speed and wavenumber are shown in Fig. 4.5.

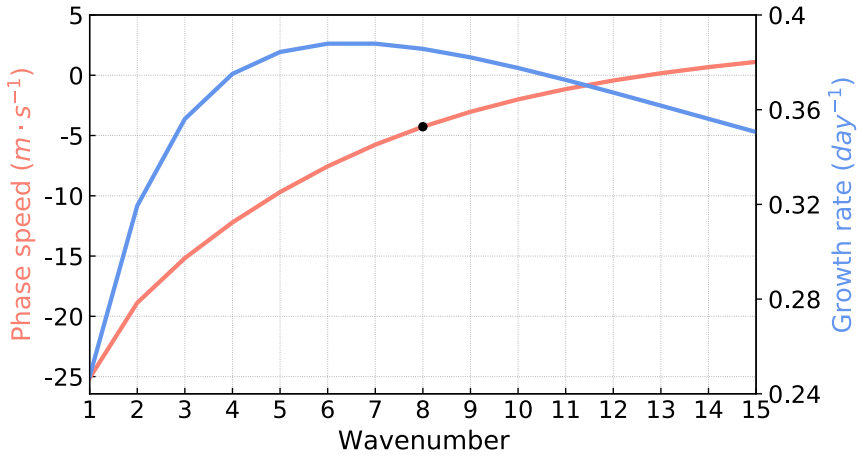

FIG. 4.5 Phase speed (orange) and growth rate (blue) of the wave solution at different wavenumbers.

The solution to the model at layer P_3 is shown in Fig. 4.6. A growing wave moves westward at a speed of $4.3\ m \cdot s^{-1}$ when the wavenumber is 8. The displacement between the moisture and the streamfunction is due to the polarization relation (Eq. 32 in AM23).

In previous studies, the Eliassen-Palm flux (E-P flux) has been extensively used to diagnose the activity for dry disturbances (Edmon et al. 1980), especially in the mid-latitudes. AM23 followed the idea and developed the moisture mode activity to show the latent energy

conversion of moist waves. By swapping the potential vorticity with column-integrated specific humidity anomalies in E-P flux, the moisture mode activity is defined as follows:

$$A = \frac{L_v \widetilde{\langle q' \rangle^2}}{2} \left(\frac{\partial \widetilde{\langle q \rangle}}{\partial y} \right)^{-1}, \tag{4.11}$$

The sign is flipped comparing to Eq. 36 in AM23 due to the mean moisture increases from south to north in the Indian monsoon (Fig. 4.7), which is contrary to the Hadley Cell. Besides, the MLPSs have stronger fluctuations along time than along latitudes. So the temporal anomalies of moisture is used here instead of the zonal deviations in AM23. When compared to the mean state, the scale of the deviations in the zonal mean column moisture gradient ($\frac{\partial \widetilde{\langle q \rangle}}{\partial y}$) is small so we assume it is a constant in both space and time. The moisture mode activity of the two-layer model is shown in Fig. 4.6. It peaks at the center of the wave and grows as the wave grows.

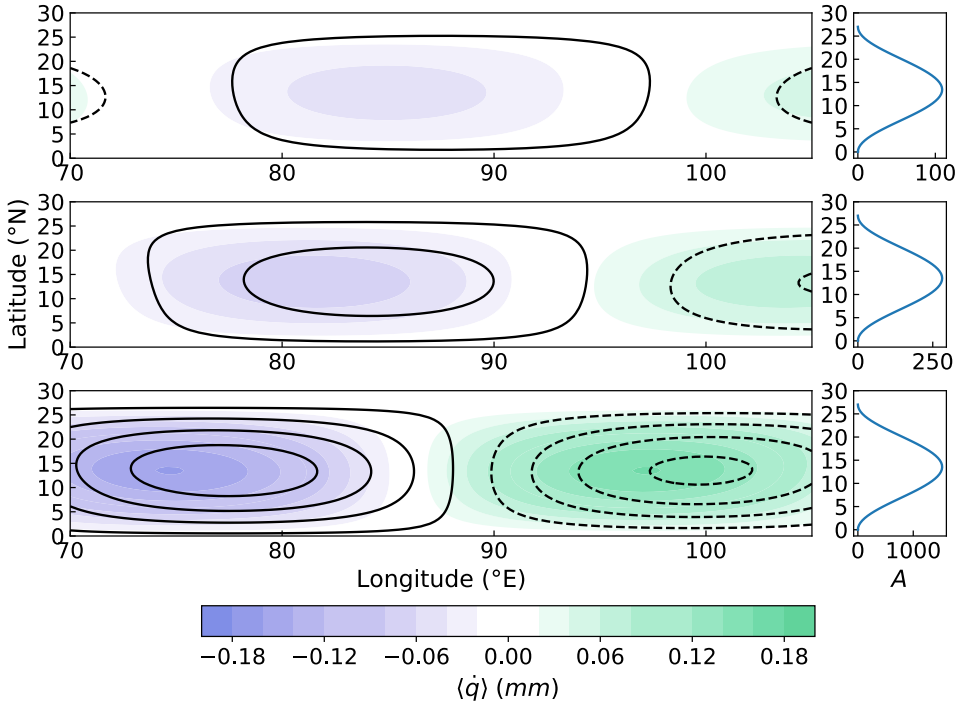

FIG. 4.6 The wave generated through the two-layer model at three consecutive time steps (from top to bottom) with an interval of 1 day, is shown on the left. The shading is showing the column moisture, the contours are the streamfunction. The moisture mode activity is shown as the line plot on the right. X-axis is the values, Y-axis is the latitude.

As it is derived in AM23, the tendency of moisture mode activity equals to the meridional eddy latent heat flux:

$$\frac{\partial A}{\partial t} = -L_v \widetilde{v'\langle q \rangle}', \tag{4.12}$$

The equation, however, exists only when the meridional moisture gradient is significantly larger than the zonal gradient. As is shown in Fig. 4.7, the zonal moisture gradient increases and exceeds the meridional gradient on the west of the Bay of Bengal and central India. So, the west border of the region is set at $85°E$. The east border is consistent with the last chapter, placed at $110°E$. The south and north borders are extended to $0°$ and $26°N$ in order to preserve the activity of the Indian monsoon at the edges of the wave.

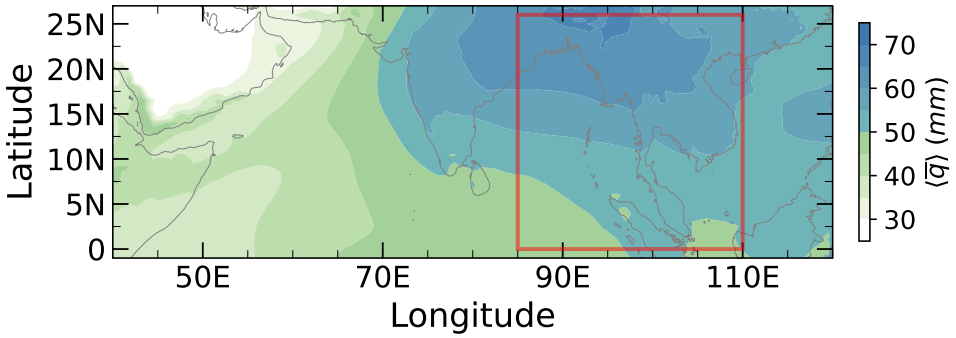

FIG. 4.7 Climatological mean column-integrated water vapor. The region studied is marked by the red box.

4.5 Moisture mode activity in reanalysis

Fig. 4.8a is a latitude-time diagram showing the variability of moisture mode activity in ERA5. The major latitudinal belt for moisture mode activity is from $15°N$ to $20°N$, which is colocated with the MLPSs tracks (Luo et al. 2023). Also, a slight tilt from south to north is seen, indicating a diminutive northward propagation. The pattern has two peaks. The first and the

strongest peak is on day -0.5, 12 hours before the maximum signal day, and the second one is on day 2.5, centered at $18°N$. The peaks represent the passage of anomalous centers, which could either be a trough or a ridge.

The latitude-time diagram of eddy meridional moisture flux is shown in Fig. 4.8b. The latitudinal belt of flux centers colocates with the belt of moisture mode activity center. The flux pattern is in correspondence with the tendency of the moisture mode activity, proving Eq. (4.12) is true in the observed disturbances. The flux also reveals the intensity variability of the wave: a positive value refers to growth and a negative value represents decay. A slight tilt is seen in the flux, indicating a northward propagation.

In AM23, an "available latent energy" (ALE) was defined to depict the background variability, it refers to the part of latent energy that can be converted and contribute to wave activity:

$$\mathrm{ALE} \equiv \int_{-L_H}^{0} \widetilde{\langle q \rangle}\, dy \sim \frac{L_H^2}{2} \frac{L_v\, \partial \widetilde{\langle q \rangle}}{\partial y}, \tag{4.13}$$

where L_H is the half width of the region. And its tendency is the inverse of eddy moisture flux. To simplify, ALE is proportional to latent heat difference at the south and north margins:

$$\mathrm{ALE} \propto \widetilde{\langle q \rangle'}_N - \widetilde{\langle q \rangle'}_S, \tag{4.14}$$

where $\widetilde{\langle q \rangle'}_N$ and $\widetilde{\langle q \rangle'}_S$ refer to the zonal averaged column moisture anomalies at the north and south boundaries.

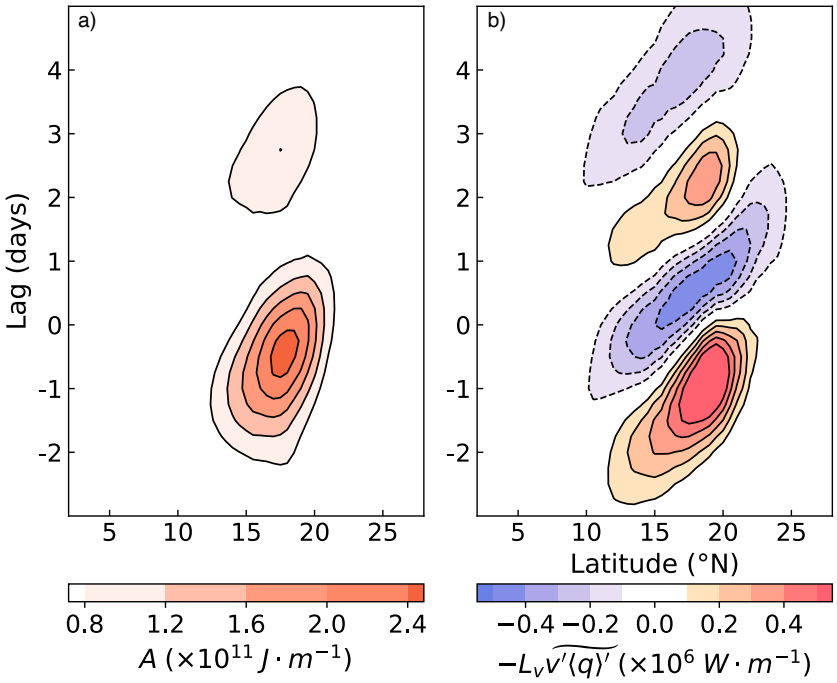

FIG. 4.8 Latitude-time diagram of the moisture mode activity (a) and zonal averaged meridional latent heat flux (b).

The ALE, regional averaged moisture mode activity and meridional eddy moisture flux are shown in Fig. 4.9. The eddy meridional moisture flux indicates the growth and decay of MLPSs. The disturbances grow from day -3 to day -0.5 and decay on day 0 and day 1. A second growth happens on day 2 and turns into decay soon. The line plots also proved the relationship in Eq. (3.12). The ALE is approximately equal to the inverse of meridional averaged moisture mode activity. The changes of ALE indicate that when the disturbances grow/decay from MVI, the latent energy gradient of the monsoon decreases/increases through positive/negative meridional eddy moisture flux, leading to moistening/drying in the south and drying/moistening in the north (Fig. 3.3). In other words, the MLPSs grow at the expense of the Indian monsoon.

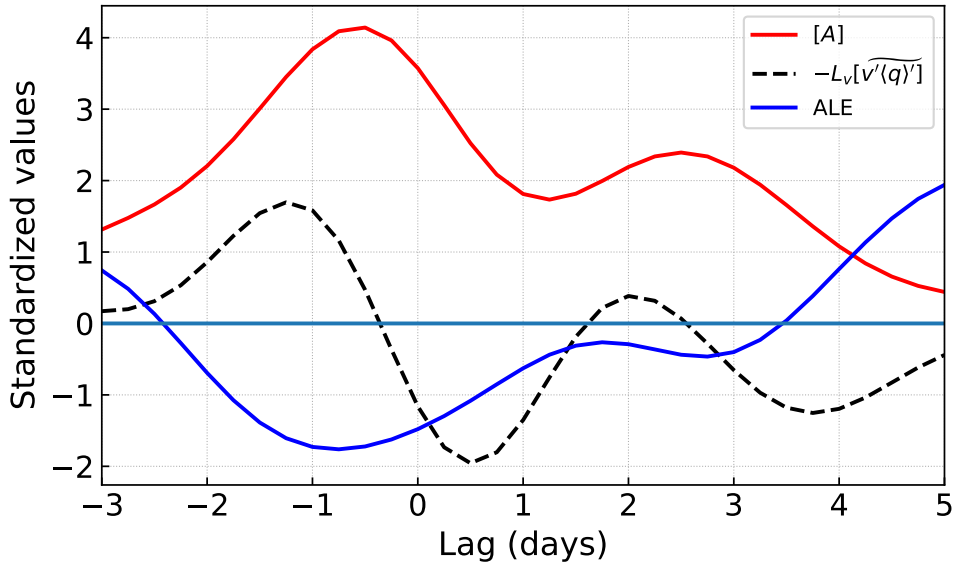

FIG. 4.9 Standardized meridional averaged moisture mode activity (red line), meridional latent heat flux (dashed line) and available latent energy (ALE, blue line). The standardized values are obtained through dividing by their temporal standard deviations.

4.6 Discussion and conclusion

In this chapter, we examined the importance of water vapor in the Indian monsoon low pressure systems by investigating the criteria of moisture mode. The precipitation induced by MLPSs is found to be highly correlated with its column-integrated water vapor. Besides, the systems are in WTG balance. And latent heat plays a leading role in MSE. Moreover, the N_{mode} is greatly smaller than 1, indicating that the moisture variability is more important than the temperature variability in the thermodynamics.

To better show the interaction between MLPSs and the Indian monsoon, we utilized a two-layer model with prognostic moisture at the bottom layer. The solution to the model is a growing westward propagating wave at a speed of $4\,m \cdot s^{-1}$. Based on the solution, the moisture mode activity was formulated to represent the wave processes. When assuming the meridional moisture gradient changes little with time and space, the tendency of the wave activity equals the meridional

flux. Such a relationship is observed near the head of the Bay of Bengal. The available latent energy anomalies, as a representation of the monsoon variability, are associated with the meridional averaged moisture mode activity. The observed feature indicates that when the wave grows from MVI, the equatorward moisture flux weakens the background. When MLPSs decay, the moisture flux points poleward, taking away latent energy from the disturbances and enhancing the monsoon.

There are some caveats in this study. The two-layer model and the moisture mode activity only account for the linear processes between the background and the disturbances. The nonlinear processes might also be important such as mesoscale processes could diffuse moisture, acting as the dissipation of the moisture mode activity (Adames Corraliza and Mayta 2023). Moreover, the current framework assumes that the contributions from zonal moisture advection as well as vertical moisture advection, radiation and surface fluxes are negligibly small. However, the zonal moisture gradient is larger if we expand our domain further to the west. So future studies will focus on incorporating the linear and nonlinear genesis or dissipation terms that we neglected into the budget of moisture mode activity and ALE.

Chapter 5 Conclusions and Future work

5.1 Summary of Findings

5.1.1 Conclusion for Chapter 2

In Chapter 2, we analyzed the dynamics of the Bermuda High and a Rossby wave train using linear regressions and composites onto the Bermuda High Index. BHI was created by subtracting the sea-level pressure at $30°\mathrm{N}, 90°\mathrm{W}$ from the SLP at $40°\mathrm{N}, 60°\mathrm{W}$. The composites of the mean geopotential height show a contraction pattern when BHI is positive and an expansion mode when BHI is negative. Enhanced mean precipitation and column-integrated moisture over the southeastern US is seen when the Bermuda High contracts. The expansion of the Bermuda High corresponds to suppressed rainfall and water vapor. The regressions of anomalous geopotential height at 850 hPa and precipitation reveal the potential connection between the circulation and rainfall variations as well.

The regressions at 200 hPa geopotential height reveal the existence of a mid-latitude Rossby wave train. The Rossby wave has a wavenumber of 7 and is centered around the belt of 40-50°N. It propagates eastward, and its axis colocates with the mid-latitude westly jet, indicating the jet being its waveguide. The amplitude of the wave reaches its maximum near North America and the North Atlantic. In order to show the mechanism leading to precipitation, we made use of the thermodynamic energy equation (Eq. (2.6)). The energy equation can be further transformed into a diagnostic ω equation. The factors leading to the vertical motion were separated into diabatic heating, radiative heating and horizontal temperature advection. The major contributor to the

vertical velocity is the latent heat released by the precipitating clouds. Radiative heating and horizontal temperature advection are non-negligibly small. The diabatic heating leads to vertical motion in both the northern Gulf of Mexico and east of Florida. The radiative heating is responsible for the vertical velocity near the east of Florida and the temperature advection is responsible for the vertical velocity near the northern Gulf. It's possible that the warm air advection moistens the troposphere through isentropic lifting thus leading to precipitation. The lifting is enhanced due to the decrease in outgoing longwave radiation by high clouds. The results indicate that the variations of Bermuda High at lower levels are associated with the fluctuations in the Rossby wave train. The precipitation is modulated by the Rossby wave train and the Bermuda High.

5.1.2 Conclusion for Chapter 3

In Chapter 3, we utilized a similar approach by creating an Index that represents the variability of monsoon low pressure systems and regressing onto the index. However, different from the Bermuda High, which varies at the monthly time scale, the monsoon low pressure systems are synoptic wave-like disturbances. In order to capture the transient signal, a band-pass filter was adopted. The filtered data has a frequency between $1/2$ to $1/15\ day^{-1}$, and a wavenumber between 3 to 25, propagating westward. The index was generated through the regional average of the filtered precipitation over the head of Bay of Bengal. When regressing the geopotential height anomalies onto the index, we see a high-low-high pattern across the Bay of Bengal and India. The lag regressions from 2 days ahead of the maximum signal day to 2 days after reveals the westward propagation of the wave. The wave intensifies on day -2 and -1, reaches maximum strength around day 0 and decays on day 1. The enhanced precipitation is associated with the troughs while suppressed precipitation is in accordance with the ridges. The moist static energy, which is linear

to both moisture and temperature was used to reveal to thermodynamics of the wave. The root-mean-square of the MSE anomalies shows the tracks of the wave and it follows the isopleth of the climatological mean MSE. The feature indicates that the disturbance propagates in the isentropes.

Conventional studies attributed the growth and propagation of the wave to the baroclinic or barotropic instability. However, the vertical structure disagrees with the baroclinic instability. The regressions of the vertical cross-sections show an upright structure instead of eastward tilting on the top. Besides, the vorticity, moisture and precipitation are in-phase with each other. Since the baroclinic instability cannot explain the vertical features, the moisture-vortex instability was proposed as an alternative. The MVI depicts a cycle in which the strong meridional advection of MSE leads to an increase in the moisture tendency, the latent heat released by the moisture enhances the convection and the vortex grows through vortex stretching. The system that grows from MVI has an upright structure and the circulation is colocated with the precipitation and moisture.

The analysis of MSE budgets supported the idea that MLPSs grow from MVI. The major contributor to the propagation and growth is the meridional advection of mean MSE by anomalous winds. The contribution from the zonal advection is small but non-negligible to the decay of the disturbances. The vertical MSE advection is a sink to both propagation and growth but is balanced out by the longwave radiation flux. The vertical motion leads to the appearance of anvils thus suppressing the outgoing longwave radiation due to the greenhouse effect.

The analysis of the perturbation kinetic energy indicates that the major source leading to propagation is the geopotential anomalies advected by the anomalous horizontal winds. The potential energy conversion is not only a cause to propagation but also a reason for growth. It is associated with the vertical instability. The other source to the growth is the horizontal barotropic

term, indicating that the barotropic conversion plays an important role in the vortex growth. Compared to the MSE budget, the PKE budget, however, has a large residual. The residual contains frictional dissipation and other processes such as subgrid turbulence or convective waves that cannot be obtained from the reanalysis data.

This study showed that the observed features are incoherent with the baroclinic instability but instead, consistent with the MVI and barotropic instability. Also, the importance of moisture is hinted for such tropical convective disturbances.

5.1.3 Conclusion for Chapter 4

As mentioned in Chapter 3, moisture is vital to the growth of MLPSs. In Chapter 4, we used the moisture mode criteria to quantify the significance of moisture. Firstly, the precipitation induced by MLPSs is highly correlated with the column-integrated moisture. Secondly, the diabatic heating is in balance with the adiabatic cooling. Thirdly, the latent heat is taking a large portion of MSE. Moreover, the dimensionless number, N_{mode} was found to be greatly smaller than 1, indicating that the moisture instead of temperature variation is the dominant in the thermodynamics. By Satisfying these criteria, MLPSs can be regarded as moisture mode.

A two-layer mode with prognostic moisture at the bottom layer was then used to study the interactions between the wave and background when the moisture mode grows from the moisture-vortex instability. The two-layer model has two major layers and two minor layers in each major layer. The mean zonal wind at the bottom layer is $5\ m \cdot s^{-1}$. The moisture gradient at the bottom layer is $5 \times 10^{-6} kg \cdot m^{-3}$. The solution to the model shows a westward propagating wave at a phase speed of $4\ m \cdot s^{-1}$. Based on the model, the moisture mode activity was formulated. It shows that two MLPSs centers passed through the head of Bay of Bengal. The tendency of the

moisture mode activity equals to the meridional eddy moisture flux, which indicates the intensity change in the disturbances. The wave grows from day -3 to day -1, decays from day 0 and day 1, grows again on day 2 and decays again from day 3 to day 5. The variability coincides with the projections of MSE tendency to maintenance variations in Chapter 3. The quantity that shows the variations of the Indian monsoon is defined as the available latent energy. The ALE is proportional to the meridional gradient of moisture anomalies. Its tendency equals to the inverse of meridional eddy moisture flux. So ALE shows an opposite trend of the moisture mode activity. The relationship indicates that the MLPSs grow at the expense of the Indian summer monsoon through the equatorward eddy moisture flux during their growth from MVI.

5.2 Outlook for future work

In Chapter 2, we verified that the variations of the Bermuda High are associated with the precipitation anomalies near the southeastern US. A mid-latitude Rossby wave train related to the Bermuda High was discovered. The major contributor to the anomalous vertical motions is diabatic heating. The radiative heating and horizontal temperature advection are small but should not be omitted. We hypothesized that the warm temperature advection leads to isentropic lifting and thus moistens the air can cause rainfall. However, we did not investigate the moisture advection. So we cannot conclude the full processes as temperature-driven or driven by both temperature and moisture. Future work on this Chapter would focus on calculating the moisture budgets or MSE budgets.

Moreover, though the major impacts of the Rossby wave train are located over North America and the North Atlantic, a significant spot shows up over the western North Pacific. From

the T-N wave activity flux, the spot could be the upper end of the wave and the location could be potentially related to the Asian Monsoon. Future work should examine the possibility.

In Chapter 3, we compared the observed features of Indian monsoon low pressure systems to the existing instability theories: baroclinic instability, moisture-vortex instability and barotropic instability. Then we analyzed the moist static energy budget and perturbation kinetic energy budget. The budget analysis reveals that MLPSs go through MVI-like and barotropic growth. Nevertheless, the residual in the PKE budget is large and it can be caused by many reasons such as friction, sub-grid processes and numerical errors in the reanalysis products. Further investigation to the PKE residual is needed such as changing datasets and switching to numeric models.

In Chapter 4, we presented that MLPSs are consistent with the moisture mode theory. Besides, we made use of the moisture mode activity, available latent energy and the meridional eddy moisture flux to show that MLPSs weaken the Indian monsoon while they grow. During the analysis, we assumed that the climatological mean meridional moisture gradient only has subtle changes in time and space so we excluded the non-linear processes between the moisture mode activity tendency, ALE tendency and the meridional eddy moisture flux. Future study should bridge the gap by looking into the dissipation of moisture mode activity and the genesis of ALE. Terms that have smaller contributions, such as zonal moisture advection, radiation and surface fluxes, should also be included. The region that we studied in Chapter 4 has a narrower longitude than the region in Chapter 3 because of the meridional moisture gradient is smaller in the west of Bay of Bengal. When we add the non-linear processes and neglected terms back, we could potentially extend the area further to the west. So that our theory can be applied to a broader monsoonal region.

For future study, the impact from the global warming also needs to be taken into consideration. The short-term summertime rainfall variability was shown to be sensitive to the location and strength of the Bermuda High, and long-term rainfall variability was also related to the central longitude of the High in a warming climate (Schmidt and Grise 2019). Studies suggested that the intensity of the Bermuda High increased and its western ridge shifted westward in the past 30 years (Li et al. 2011). Future projections from the models also indicated an enhanced Bermuda High pattern with greenhouse gas forcing (Li et al. 2012b). With such background, it is hypothesized that the continuing enhancement and westward movement of the Bermuda High will increase the precipitation variability over the southeastern US through stronger moisture flux and leading to a worse midsummer drought. As a potential source of the Rossby wave train at mid and higher troposphere, the East Asian summer monsoon was also suggested to show a strengthened scenario (You et al. 2022; Liu et al. 2023). The modulation to the American rainfall from the Rossby wave train will be affected by such increased intensity and variability in the East Asian monsoon.

As the sea surface temperature rises, enhanced evaporation leads to more moisture entering the atmosphere. The Indian summer monsoon tends to be more devastating by creating more precipitation extremes and becoming more unstable (Wang et al. 2021). The Indian monsoon low pressure systems, are observed to be more frequent (Thomas et al. 2021). With more available latent energy from increased water vapor in the monsoon. The low pressure systems can develop into stronger depressions and bring more precipitation to adjacent area. The stirring effect, in which the disturbance weakens the monsoon, could potentially also be enhanced due to increased energy conversion. Overall, the dry/wet situation in both southeastern US and South Asia would be more erratic and unpredictable in a warming climate.

Bibliography

Adames, Á. F., 2021: Interactions between Water Vapor, Potential Vorticity, and Vertical Wind Shear in Quasi-Geostrophic Motions: Implications for Rotational Tropical Motion Systems. *Journal of the Atmospheric Sciences*, **78**, 903–923, https://doi.org/10.1175/JAS-D-20-0205.1.

——, 2022: The Basic Equations under Weak Temperature Gradient Balance: Formulation, Scaling, and Types of Convectively Coupled Motions. *Journal of the Atmospheric Sciences*, **79**, 2087–2108, https://doi.org/10.1175/JAS-D-21-0215.1.

——, and J. M. Wallace, 2014: Three-Dimensional Structure and Evolution of the MJO and Its Relation to the Mean Flow. *J. Atmos. Sci.*, **71**, 2007–2026, https://doi.org/10.1175/JAS-D-13-0254.1.

——, and D. Kim, 2016: The MJO as a Dispersive, Convectively Coupled Moisture Wave: Theory and Observations. *Journal of the Atmospheric Sciences*, **73**, 913–941, https://doi.org/10.1175/JAS-D-15-0170.1.

——, and Y. Ming, 2018a: Interactions between Water Vapor and Potential Vorticity in Synoptic-Scale Monsoonal Disturbances: Moisture Vortex Instability. *Journal of the Atmospheric Sciences*, **75**, 2083–2106, https://doi.org/10.1175/JAS-D-17-0310.1.

——, and ——, 2018b: Moisture and Moist Static Energy Budgets of South Asian Monsoon Low Pressure Systems in GFDL AM4.0. *J. Atmos. Sci.*, **75**, 2107–2123, https://doi.org/10.1175/JAS-D-17-0309.1.

——, and E. D. Maloney, 2021: Moisture Mode Theory's Contribution to Advances in our Understanding of the Madden-Julian Oscillation and Other Tropical Disturbances. *Curr Clim Change Rep*, **7**, 72–85, https://doi.org/10.1007/s40641-021-00172-4.

——, D. Kim, S. K. Clark, Y. Ming, and K. Inoue, 2019: Scale Analysis of Moist Thermodynamics in a Simple Model and the Relationship between Moisture Modes and Gravity Waves. *Journal of the Atmospheric Sciences*, **76**, 3863–3881, https://doi.org/10.1175/JAS-D-19-0121.1.

Adames Corraliza, Á. F., and V. Mayta, 2023: The Stirring Tropics. Part II: Theory of Moisture Mode−Hadley Cell Interactions.

Adler, R. F., and Coauthors, 2003: The Version-2 Global Precipitation Climatology Project (GPCP) Monthly Precipitation Analysis (1979–Present). *J. Hydrometeor.*, **4**, 1147–1167, https://doi.org/10.1175/1525-7541(2003)004<1147:TVGPCP>2.0.CO;2.

——, and Coauthors, 2018: The Global Precipitation Climatology Project (GPCP) Monthly Analysis (New Version 2.3) and a Review of 2017 Global Precipitation. *Atmosphere*, **9**, 138, https://doi.org/10.3390/atmos9040138.

Ahmed, F., and C. Schumacher, 2015: Convective and stratiform components of the precipitation-moisture relationship. *Geophysical Research Letters*, **42**, 10,453-10,462, https://doi.org/10.1002/2015GL066957.

——, J. D. Neelin, and Á. F. Adames, 2021: Quasi-Equilibrium and Weak Temperature Gradient Balances in an Equatorial Beta-Plane Model. *Journal of the Atmospheric Sciences*, **78**, 209–227, https://doi.org/10.1175/JAS-D-20-0184.1.

Ajayamohan, R. S., W. J. Merryfield, and V. V. Kharin, 2010: Increasing Trend of Synoptic Activity and Its Relationship with Extreme Rain Events over Central India. *Journal of Climate*, **23**, 1004–1013, https://doi.org/10.1175/2009JCLI2918.1.

Alaka, G. J., and E. D. Maloney, 2014: The Intraseasonal Variability of African Easterly Wave Energetics. *Journal of Climate*, **27**, 6559–6580, https://doi.org/10.1175/JCLI-D-14-00146.1.

Andersen, J. A., and Z. Kuang, 2012: Moist Static Energy Budget of MJO-like Disturbances in the Atmosphere of a Zonally Symmetric Aquaplanet. *Journal of Climate*, **25**, 2782–2804, https://doi.org/10.1175/JCLI-D-11-00168.1.

Aravéquia, J., B. Vadlamudi, and J. Bonatti, 1995: The Role of Moist Baroclinic Instability in the Growth and Structure of Monsoon Depressions. *Journal of the Atmospheric Sciences*, **52**, https://doi.org/10.1175/1520-0469(1995)052<4393:TROMBI>2.0.CO;2.

Betts, A. K., 1986: A new convective adjustment scheme. Part I: Observational and theoretical basis. *Quarterly Journal of the Royal Meteorological Society*, **112**, 677–691, https://doi.org/10.1002/qj.49711247307.

——, and M. J. Miller, 1986: A new convective adjustment scheme. Part II: Single column tests using GATE wave, BOMEX, ATEX and arctic air-mass data sets. *Quarterly Journal of the Royal Meteorological Society*, **112**, 693–709, https://doi.org/10.1002/qj.49711247308.

Boos, W. R., J. V. Hurley, and V. S. Murthy, 2015: Adiabatic westward drift of Indian monsoon depressions. *Quarterly Journal of the Royal Meteorological Society*, **141**, 1035–1048, https://doi.org/10.1002/qj.2454.

Boos, W. R., B. E. Mapes, and V. S. Murthy, 2016: Potential Vorticity Structure and Propagation Mechanism of Indian Monsoon Depressions. *The Global Monsoon System*, Vol. Volume 9 of *World Scientific Series on Asia-Pacific Weather and Climate*, World Scientific, 187–199.

Branstator, G., 1983: Horizontal Energy propagation in a Barotropic Atmosphere with Meridional and Zonal Structure. *J. Atmos. Sci.*, **40**, 1689–1708, https://doi.org/10.1175/1520-0469(1983)040<1689:HEPIAB>2.0.CO;2.

——, 2002: Circumglobal Teleconnections, the Jet Stream Waveguide, and the North Atlantic Oscillation. *Journal of Climate*, **15**, 1893–1910, https://doi.org/10.1175/1520-0442(2002)015<1893:CTTJSW>2.0.CO;2.

Bretherton, C. S., C. Smith, and J. M. Wallace, 1992: An Intercomparison of Methods for Finding Coupled Patterns in Climate Data. *J. Climate*, **5**, 541–560, https://doi.org/10.1175/1520-0442(1992)005<0541:AIOMFF>2.0.CO;2.

——, M. E. Peters, and L. E. Back, 2004: Relationships between Water Vapor Path and Precipitation over the Tropical Oceans. *Journal of Climate*, **17**, 1517–1528, https://doi.org/10.1175/1520-0442(2004)017<1517:RBWVPA>2.0.CO;2.

Chang, C.-P., 1970: Westward Propagating Cloud Patterns in the Tropical Pacific as seen from Time-Composite Satellite Photographs. *Journal of the Atmospheric Sciences*, **27**, 133–138, https://doi.org/10.1175/1520-0469(1970)027<0133:WPCPIT>2.0.CO;2.

Charney, J. G., 1947: THE DYNAMICS OF LONG WAVES IN A BAROCLINIC WESTERLY CURRENT. *Journal of the Atmospheric Sciences*, **4**, 136–162, https://doi.org/10.1175/1520-0469(1947)004<0136:TDOLWI>2.0.CO;2.

——, and M. E. Stern, 1962: On the Stability of Internal Baroclinic Jets in a Rotating Atmosphere. *Journal of the Atmospheric Sciences*, **19**, 159–172, https://doi.org/10.1175/1520-0469(1962)019<0159:OTSOIB>2.0.CO;2.

Chen, B., W. Tung, and M. Yanai, 2016: Multiscale Temporal Mean Features of Perturbation Kinetic Energy and Its Budget in the Tropics: Review and Computation. *Meteorological Monographs*, **56**, 8.1-8.23, https://doi.org/10.1175/AMSMONOGRAPHS-D-15-0017.1.

Chen, P., M. P. Hoerling, and R. M. Dole, 2001: The Origin of the Subtropical Anticyclones. *J. Atmos. Sci.*, **58**, 1827–1835, https://doi.org/10.1175/1520-0469(2001)058<1827:TOOTSA>2.0.CO;2.

Chen, W. Y., 1982: Fluctuations in Northern Hemisphere 700 mb Height Field Associated with the Southern Oscillation. *Mon. Wea. Rev.*, **110**, 808–823, https://doi.org/10.1175/1520-0493(1982)110<0808:FINHMH>2.0.CO;2.

Cherry, S., 1996: Singular Value Decomposition Analysis and Canonical Correlation Analysis. *J. Climate*, **9**, 2003–2009, https://doi.org/10.1175/1520-0442(1996)009<2003:SVDAAC>2.0.CO;2.

Clark, S. K., Y. Ming, and Á. F. Adames, 2020: Monsoon Low Pressure System–Like Variability in an Idealized Moist Model. *Journal of Climate*, **33**, 2051–2074, https://doi.org/10.1175/JCLI-D-19-0289.1.

Cohen, N. Y., and W. R. Boos, 2016: Perspectives on Moist Baroclinic Instability: Implications for the Growth of Monsoon Depressions. *Journal of the Atmospheric Sciences*, **73**, 1767–1788, https://doi.org/10.1175/JAS-D-15-0254.1.

Davis, R. E., 1976: Predictability of Sea Surface Temperature and Sea Level Pressure Anomalies over the North Pacific Ocean. *J. Phys. Oceanogr.*, **6**, 249–266, https://doi.org/10.1175/1520-0485(1976)006<0249:POSSTA>2.0.CO;2.

——, 1978: Predictability of Sea Level Pressure Anomalies Over the North Pacific Ocean. *Journal of Physical Oceanography*, **8**, 233–246, https://doi.org/10.1175/1520-0485(1978)008<0233:POSLPA>2.0.CO;2.

Davis, R. E., B. P. Hayden, D. A. Gay, W. L. Phillips, and G. V. Jones, 1997: The North Atlantic Subtropical Anticyclone. *J. Climate*, **10**, 728–744, https://doi.org/10.1175/1520-0442(1997)010<0728:TNASA>2.0.CO;2.

Diaz, M., and W. R. Boos, 2019a: Barotropic growth of monsoon depressions. *Quarterly Journal of the Royal Meteorological Society*, **145**, 824–844, https://doi.org/10.1002/qj.3467.

——, and ——, 2019b: Monsoon depression amplification by moist barotropic instability in a vertically sheared environment. *Quarterly Journal of the Royal Meteorological Society*, **145**, 2666–2684, https://doi.org/10.1002/qj.3585.

——, and ——, 2021a: Evolution of Idealized Vortices in Monsoon-Like Shears: Application to Monsoon Depressions. *Journal of the Atmospheric Sciences*, **78**, 1207–1225, https://doi.org/10.1175/JAS-D-20-0286.1.

——, and ——, 2021b: The Influence of Surface Heat Fluxes on the Growth of Idealized Monsoon Depressions. *Journal of the Atmospheric Sciences*, **78**, 2013–2027, https://doi.org/10.1175/JAS-D-20-0359.1.

Diem, J. E., 2006: Synoptic-Scale Controls of Summer Precipitation in the Southeastern United States. *J. Climate*, **19**, 613–621, https://doi.org/10.1175/JCLI3645.1.

Ditchek, S. D., W. R. Boos, S. J. Camargo, and M. K. Tippett, 2016: A Genesis Index for Monsoon Disturbances. *Journal of Climate*, **29**, 5189–5203, https://doi.org/10.1175/JCLI-D-15-0704.1.

Dong, W., Y. Lin, J. S. Wright, Y. Xie, F. Xu, W. Xu, and Y. Wang, 2017: Indian Monsoon Low-Pressure Systems Feed Up-and-Over Moisture Transport to the Southwestern Tibetan Plateau. *Journal of Geophysical Research: Atmospheres*, **122**, 12,140-12,151, https://doi.org/10.1002/2017JD027296.

Edmon, H. J., B. J. Hoskins, and M. E. McIntyre, 1980: Eliassen-Palm Cross Sections for the Troposphere. *J. Atmos. Sci.*, **37**, 2600–2616, https://doi.org/10.1175/1520-0469(1980)037<2600:EPCSFT>2.0.CO;2.

Eliot, J., 1884: Accounts of Southwest Monsoon Storms Generated in the Bay of Bengal during 1877-1888. *India Meteorological Department*, 217–448.

Francis, J. A., and S. J. Vavrus, 2012: Evidence linking Arctic amplification to extreme weather in mid-latitudes. *Geophysical Research Letters*, **39**, https://doi.org/10.1029/2012GL051000.

Fujinami, H., H. Hirata, M. Kato, and K. Tsuboki, 2019: Mesoscale precipitation systems and their role in the rapid development of a monsoon depression over the Bay of Bengal. *Quarterly Journal of the Royal Meteorological Society*, **146**, https://doi.org/10.1002/qj.3672.

Gamble, D. W., D. B. Parnell, and S. Curtis, 2008: Spatial variability of the Caribbean mid-summer drought and relation to north Atlantic high circulation. *International Journal of Climatology*, **28**, 343–350, https://doi.org/10.1002/joc.1600.

Giannini, A., Y. Kushnir, and M. A. Cane, 2000: Interannual Variability of Caribbean Rainfall, ENSO, and the Atlantic Ocean. *J. Climate*, **13**, 297–311, https://doi.org/10.1175/1520-0442(2000)013<0297:IVOCRE>2.0.CO;2.

Godbole, R. V., 1977: The composite structure of the monsoon depression. *Tellus*, **29**, 25–40, https://doi.org/10.1111/j.2153-3490.1977.tb00706.x.

Hastenrath, S., 1976: Variations in Low-Latitude Circulation and Extreme Climatic Events in the Tropical Americas. *J. Atmos. Sci.*, **33**, 202–215, https://doi.org/10.1175/1520-0469(1976)033<0202:VILLCA>2.0.CO;2.

——, 1978: On Modes of Tropical Circulation and Climate Anomalies. *J. Atmos. Sci.*, **35**, 2222–2231, https://doi.org/10.1175/1520-0469(1978)035<2222:OMOTCA>2.0.CO;2.

Hayashi, Y., 1971: Method of Resolving Disturbances into and Retrogressive Waves by Space and Time Cross-Spectral Analyses. *Journal of the Meteorological Society of Japan*, **49**, 4.

——, 1979: A Generalized Method of Resolving Transient Disturbances into Standing and Traveling Waves by Space-Time Spectral Analysis. *Journal of the Atmospheric Sciences*, **36**, 1017–1029, https://doi.org/10.1175/1520-0469(1979)036<1017:AGMORT>2.0.CO;2.

Henderson, K. G., and A. J. Vega, 1996: Regional Precipitation Variability in the Southern United States. *Physical Geography*, **17**, 93–112, https://doi.org/10.1080/02723646.1996.10642576.

Hersbach, H., and Coauthors, 2019: Global reanalysis: goodbye ERA-Interim, hello ERA5. 17–24, https://doi.org/10.21957/vf291hehd7.

Holloway, C. E., and J. D. Neelin, 2009: Moisture Vertical Structure, Column Water Vapor, and Tropical Deep Convection. *J. Atmos. Sci.*, **66**, 1665–1683, https://doi.org/10.1175/2008JAS2806.1.

Holton, J. R., and G. J. Hakim, 2013a: Chapter 6 - Quasi-geostrophic Analysis. *An Introduction to Dynamic Meteorology (Fifth Edition)*, J.R. Holton and G.J. Hakim, Eds., Academic Press, 171–211.

——, and ——, 2013b: Chapter 7 - Baroclinic Development. *An Introduction to Dynamic Meteorology (Fifth Edition)*, J.R. Holton and G.J. Hakim, Eds., Academic Press, 213–254.

Hoskins, B. J., and D. J. Karoly, 1981: The Steady Linear Response of a Spherical Atmosphere to Thermal and Orographic Forcing. *J. Atmos. Sci.*, **38**, 1179–1196, https://doi.org/10.1175/1520-0469(1981)038<1179:TSLROA>2.0.CO;2.

——, and T. Ambrizzi, 1993: Rossby Wave Propagation on a Realistic Longitudinally Varying Flow. *J. Atmos. Sci.*, **50**, 1661–1671, https://doi.org/10.1175/1520-0469(1993)050<1661:RWPOAR>2.0.CO;2.

Hu, Q., 1997: On the Uniqueness of the Singular Value Decomposition in Meteorological Applications. *J. Climate*, **10**, 1762–1766, https://doi.org/10.1175/1520-0442(1997)010<1762:OTUOTS>2.0.CO;2.

Hunt, K. M. R., and J. K. Fletcher, 2019: The relationship between Indian monsoon rainfall and low-pressure systems. *Clim Dyn*, **53**, 1859–1871, https://doi.org/10.1007/s00382-019-04744-x.

——, A. G. Turner, P. M. Inness, D. E. Parker, and R. C. Levine, 2016: On the Structure and Dynamics of Indian Monsoon Depressions. *Monthly Weather Review*, **144**, 3391–3416, https://doi.org/10.1175/MWR-D-15-0138.1.

——, ——, and L. C. Shaffrey, 2018: Extreme Daily Rainfall in Pakistan and North India: Scale Interactions, Mechanisms, and Precursors. *Monthly Weather Review*, **146**, 1005–1022, https://doi.org/10.1175/MWR-D-17-0258.1.

Inoue, K., Á. F. Adames, and K. Yasunaga, 2020: Vertical Velocity Profiles in Convectively Coupled Equatorial Waves and MJO: New Diagnoses of Vertical Velocity Profiles in the Wavenumber–Frequency Domain. *Journal of the Atmospheric Sciences*, **77**, 2139–2162, https://doi.org/10.1175/JAS-D-19-0209.1.

Kållberg, P. W., P. Berrisford, B. J. Hoskins, A. Simmons, S. Uppala, S. Lamy-Thépaut, and R. Hine, 2005: ERA-40 Atlas. [Note: Large PDF file: 68.3 MB; Revised version posted 19.01.2006]. 191.

Kasture, S. V., R. N. Keshavamurty, and V. Satyan, 1993: A model study of the growth of summer monsoon disturbances. *Current Science*, **64**, 673–679.

Katz, R. W., M. B. Parlange, and C. Tebaldi, 2003: Stochastic Modeling of the Effects of Large-Scale Circulation on Daily Weather in the Southeastern U.S. *Climatic Change*, **60**, 189–216, https://doi.org/10.1023/A:1026054330406.

Keim, B. D., 1997: Preliminary Analysis of the Temporal Patterns of Heavy Rainfall across the Southeastern United States. *The Professional Geographer*, **49**, 94–104, https://doi.org/10.1111/0033-0124.00060.

Kelly, P., and B. Mapes, 2011: Zonal mean wind, the Indian monsoon, and July drying in the western Atlantic subtropics. *Journal of Geophysical Research: Atmospheres*, **116**, https://doi.org/10.1029/2010JD015405.

——, L. R. Leung, K. Balaguru, W. Xu, B. Mapes, and B. Soden, 2018: Shape of Atlantic Tropical Cyclone Tracks and the Indian Monsoon. *Geophysical Research Letters*, **45**, 10,746-10,755, https://doi.org/10.1029/2018GL080098.

Knaff, J. A., 1997: Implications of Summertime Sea Level Pressure Anomalies in the Tropical Atlantic Region. *J. Climate*, **10**, 789–804, https://doi.org/10.1175/1520-0442(1997)010<0789:IOSSLP>2.0.CO;2.

Krishnakumar, V., R. N. Keshavamurty, and S. V. Kasture, 1992: Moist baroclinic instability and the growth of monsoon depressions— linear and nonlinear studies. *Proc. Indian Acad. Sci. (Earth Planet Sci.)*, **101**, 123–152, https://doi.org/10.1007/BF02840349.

Krishnamurthy, V., and R. S. Ajayamohan, 2010: Composite Structure of Monsoon Low Pressure Systems and Its Relation to Indian Rainfall. *Journal of Climate*, **23**, 4285–4305, https://doi.org/10.1175/2010JCLI2953.1.

Krishnamurti, T. N., 1979: *Tropical Meteorology*. Secretariat of the World Meteorological Organization, 428 pp.

Krishnamurti, T. N., M. Kanamitsu, R. Godbole, C.-B. Chang, F. Carr, and J. H. Chow, 1975: Study of a Monsoon Depression (I). *Journal of the Meteorological Society of Japan. Ser. II*, **53**, 227–240, https://doi.org/10.2151/jmsj1965.53.4_227.

——, A. Martin, R. Krishnamurti, A. Simon, A. Thomas, and V. Kumar, 2013: Impacts of enhanced CCN on the organization of convection and recent reduced counts of monsoon depressions. *Clim Dyn*, **41**, 117–134, https://doi.org/10.1007/s00382-012-1638-z.

Laing, A., and J.-L. Evans, 2011: *Introduction to Tropical Meteorology, Ch. 1: Introduction: 1.3 Defining the Tropics*.

Li, L., W. Li, and Y. Kushnir, 2012a: Variation of the North Atlantic subtropical high western ridge and its implication to Southeastern US summer precipitation. *Clim Dyn*, **39**, 1401–1412, https://doi.org/10.1007/s00382-011-1214-y.

Li, W., L. Li, R. Fu, Y. Deng, and H. Wang, 2010: Changes to the North Atlantic Subtropical High and Its Role in the Intensification of Summer Rainfall Variability in the Southeastern United States. *J. Climate*, **24**, 1499–1506, https://doi.org/10.1175/2010JCLI3829.1.

——, ——, ——, ——, and ——, 2011: Changes to the North Atlantic Subtropical High and Its Role in the Intensification of Summer Rainfall Variability in the Southeastern United States. *Journal of Climate*, **24**, 1499–1506, https://doi.org/10.1175/2010JCLI3829.1.

——, ——, M. Ting, and Y. Liu, 2012b: Intensification of Northern Hemisphere subtropical highs in a warming climate. *Nature Geosci*, **5**, 830–834, https://doi.org/10.1038/ngeo1590.

Lindzen, R. S., B. Farrell, and A. J. Rosenthal, 1983: Absolute Barotropic Instability and Monsoon Depressions. *Journal of the Atmospheric Sciences*, **40**, 1178–1184, https://doi.org/10.1175/1520-0469(1983)040<1178:ABIAMD>2.0.CO;2.

Liu, Z., S.-S. Lee, A. B. Nellikkattil, J.-Y. Lee, L. Dai, K.-J. Ha, and C. L. E. Franzke, 2023: The East Asian Summer Monsoon Response to Global Warming in a High Resolution Coupled Model: Mean and Extremes. *Asia-Pac J Atmos Sci*, **59**, 29–45, https://doi.org/10.1007/s13143-022-00285-2.

Lorenz, E., 1983: History of the Atmospheric Sciences. *Bulletin of the American Meteorological Society*, **64**, 730–769, https://doi.org/10.1175/1520-0477(1983)064<0730:AHOPIA>2.0.CO;2.

Luo, H., Á. F. Adames, and R. B. Rood, 2021: A Northern Hemispheric Wave Train Associated with Interannual Variations in the Bermuda High during Boreal Summer. *Journal of Climate*, **34**, 6163–6173, https://doi.org/10.1175/JCLI-D-20-0608.1.

——, Á. F. A. Corraliza, and R. B. Rood, 2023: Barotropic and Moisture-vortex growth of Monsoon Low Pressure Systems. *Journal of the Atmospheric Sciences*, **1**, https://doi.org/10.1175/JAS-D-22-0252.1.

Madden, R. A., and P. R. Julian, 1971: Detection of a 40–50 Day Oscillation in the Zonal Wind in the Tropical Pacific. *Journal of the Atmospheric Sciences*, **28**, 702–708, https://doi.org/10.1175/1520-0469(1971)028<0702:DOADOI>2.0.CO;2.

Magaña, V., J. A. Amador, and S. Medina, 1999: The Midsummer Drought over Mexico and Central America. *Journal of Climate*, **12**, 1577–1588, https://doi.org/10.1175/1520-0442(1999)012<1577:TMDOMA>2.0.CO;2.

Maloney, E. D., and D. L. Hartmann, 2001: The Madden–Julian Oscillation, Barotropic Dynamics, and North Pacific Tropical Cyclone Formation. Part I: Observations. *Journal of the Atmospheric Sciences*, **58**, 2545–2558, https://doi.org/10.1175/1520-0469(2001)058<2545:TMJOBD>2.0.CO;2.

——, A. H. Sobel, and W. M. Hannah, 2010: Intraseasonal Variability in an Aquaplanet General Circulation Model. *Journal of Advances in Modeling Earth Systems*, **2**, https://doi.org/10.3894/JAMES.2010.2.5.

Manabe, S., J. Smagorinsky, and R. F. Strickler, 1965: SIMULATED CLIMATOLOGY OF A GENERAL CIRCULATION MODEL WITH A HYDROLOGIC CYCLE. *Monthly*

Weather Review, **93**, 769–798, https://doi.org/10.1175/1520-0493(1965)093<0769:SCOAGC>2.3.CO;2.

Mayta, V., and Á. F. A. Adames Corraliza, 2023: The Stirring Tropics. Part I: The Ubiquity of Moisture Modes and Moisture-Vortex.

Mayta, V. C., Á. F. Adames, and F. Ahmed, 2022: Westward-Propagating Moisture Mode Over the Tropical Western Hemisphere. *Geophysical Research Letters*, **49**, e2022GL097799, https://doi.org/10.1029/2022GL097799.

Miyasaka, T., and H. Nakamura, 2005: Structure and Formation Mechanisms of the Northern Hemisphere Summertime Subtropical Highs. *J. Climate*, **18**, 5046–5065, https://doi.org/10.1175/JCLI3599.1.

Mooley, D. A., 1973: Some Aspects of Indian Monsoon Depressions and the Associated Rainfall. *Monthly Weather Review*, **101**, 271–280, https://doi.org/10.1175/1520-0493(1973)101<0271:SAOIMD>2.3.CO;2.

Moorthi, S., and A. Arakawa, 1985: Baroclinic Instability with Cumulus Heating. *Journal of the Atmospheric Sciences*, **42**, 2007–2031, https://doi.org/10.1175/1520-0469(1985)042<2007:BIWCH>2.0.CO;2.

Neelin, J. D., and J.-Y. Yu, 1994: Modes of Tropical Variability under Convective Adjustment and the Madden–Julian Oscillation. Part I: Analytical Theory. *Journal of the Atmospheric Sciences*, **51**, 1876–1894, https://doi.org/10.1175/1520-0469(1994)051<1876:MOTVUC>2.0.CO;2.

Newman, M., and P. D. Sardeshmukh, 1995: A Caveat Concerning Singular Value Decomposition. *J. Climate*, **8**, 352–360, https://doi.org/10.1175/1520-0442(1995)008<0352:ACCSVD>2.0.CO;2.

Nie, J., and A. H. Sobel, 2016: Modeling the Interaction between Quasigeostrophic Vertical Motion and Convection in a Single Column. *Journal of Atmospheric Sciences*, **73**, 1101–1117, https://doi.org/10.1175/JAS-D-15-0205.1.

Nitta, T., and K. Masuda, 1981: Observational Study of a Monsoon Depression Developed Over the Bay of Bengal during Summer MONEX. *Journal of the Meteorological Society of Japan. Ser. II*, **59**, 672–682, https://doi.org/10.2151/jmsj1965.59.5_672.

North, G. R., T. L. Bell, R. F. Cahalan, and F. J. Moeng, 1982: Sampling Errors in the Estimation of Empirical Orthogonal Functions. *Mon. Wea. Rev.*, **110**, 699–706, https://doi.org/10.1175/1520-0493(1982)110<0699:SEITEO>2.0.CO;2.

——, J. A. Pyle, and F. Zhang, 2014: *Encyclopedia of Atmospheric Sciences*. Elsevier, 2874 pp.

Ortegren, J. T., P. A. Knapp, J. T. Maxwell, W. P. Tyminski, and P. T. Soulé, 2011: Ocean–Atmosphere Influences on Low-Frequency Warm-Season Drought Variability in the Gulf

Coast and Southeastern United States. *Journal of Applied Meteorology and Climatology*, **50**, 1177–1186, https://doi.org/10.1175/2010JAMC2566.1.

Petoukhov, V., S. Rahmstorf, S. Petri, and H. J. Schellnhuber, 2013: Quasiresonant amplification of planetary waves and recent Northern Hemisphere weather extremes. *Proc. Natl. Acad. Sci. U.S.A.*, **110**, 5336–5341, https://doi.org/10.1073/pnas.1222000110.

Pritchard, M. S., and C. S. Bretherton, 2014: Causal Evidence that Rotational Moisture Advection is Critical to the Superparameterized Madden–Julian Oscillation. *Journal of the Atmospheric Sciences*, **71**, 800–815, https://doi.org/10.1175/JAS-D-13-0119.1.

Rao, K. V., and S. Rajamani, 1970: Diagnostic study of a monsoon depression by Geostrophic Baroclinic Model. *MAUSAM*, **21**, 187–194, https://doi.org/10.54302/mausam.v21i2.5366.

Riehl, H., 1954: *Tropical meteorology*.

Rodwell, M. J., and B. J. Hoskins, 2001: Subtropical Anticyclones and Summer Monsoons. *J. Climate*, **14**, 3192–3211, https://doi.org/10.1175/1520-0442(2001)014<3192:SAASM>2.0.CO;2.

Ropelewski, C. F., and M. S. Halpert, 1987: Global and Regional Scale Precipitation Patterns Associated with the El Niño/Southern Oscillation. *Monthly Weather Review*, **115**, 1606–1626, https://doi.org/10.1175/1520-0493(1987)115<1606:GARSPP>2.0.CO;2.

Ruppert, J. H., and C. Hohenegger, 2018: Diurnal Circulation Adjustment and Organized Deep Convection. *Journal of Climate*, **31**, 4899–4916, https://doi.org/10.1175/JCLI-D-17-0693.1.

Rushley, S. S., D. Kim, C. S. Bretherton, and M.-S. Ahn, 2018: Reexamining the Nonlinear Moisture-Precipitation Relationship Over the Tropical Oceans. *Geophysical Research Letters*, **45**, 1133–1140, https://doi.org/10.1002/2017GL076296.

Saha, K., and C.-P. Chang, 1983: The Baroclinic Processes of Monsoon Depressions. *Monthly Weather Review*, **111**, 1506–1514, https://doi.org/10.1175/1520-0493(1983)111<1506:TBPOMD>2.0.CO;2.

——, F. Sanders, and J. Shukla, 1981: Westward Propagating Predecessors of Monsoon Depressions. *Monthly Weather Review*, **109**, 330–343, https://doi.org/10.1175/1520-0493(1981)109<0330:WPPOMD>2.0.CO;2.

Schmidt, D. F., and K. M. Grise, 2019: Impacts of Subtropical Highs on Summertime Precipitation in North America. *Journal of Geophysical Research: Atmospheres*, **124**, 11188–11204, https://doi.org/10.1029/2019JD031282.

Scott, D. W., 1979: On optimal and data-based histograms. *Biometrika*, **66**, 605–610, https://doi.org/10.1093/biomet/66.3.605.

Screen, J. A., and I. Simmonds, 2014: Amplified mid-latitude planetary waves favour particular regional weather extremes. *Nature Clim Change*, **4**, 704–709, https://doi.org/10.1038/nclimate2271.

Seager, R., R. Murtugudde, N. Naik, A. Clement, N. Gordon, and J. Miller, 2003: Air–Sea Interaction and the Seasonal Cycle of the Subtropical Anticyclones. *J. Climate*, **16**, 1948–1966, https://doi.org/10.1175/1520-0442(2003)016<1948:AIATSC>2.0.CO;2.

Sherwood, S. C., P. Minnis, and M. McGill, 2004: Deep convective cloud-top heights and their thermodynamic control during CRYSTAL-FACE. *Journal of Geophysical Research: Atmospheres*, **109**, https://doi.org/10.1029/2004JD004811.

Sikka, D. R., 1977: Some aspects of the life history, structure and movement of monsoon depressions. *PAGEOPH*, **115**, 1501–1529, https://doi.org/10.1007/BF00874421.

Small, R. J. O., S. P. de Szoeke, and S.-P. Xie, 2007: The Central American Midsummer Drought: Regional Aspects and Large-Scale Forcing. *J. Climate*, **20**, 4853–4873, https://doi.org/10.1175/JCLI4261.1.

Sobel, A., and E. Maloney, 2012: An Idealized Semi-Empirical Framework for Modeling the Madden–Julian Oscillation. *Journal of the Atmospheric Sciences*, **69**, 1691–1705, https://doi.org/10.1175/JAS-D-11-0118.1.

——, and ——, 2013: Moisture Modes and the Eastward Propagation of the MJO. *Journal of the Atmospheric Sciences*, **70**, 187–192, https://doi.org/10.1175/JAS-D-12-0189.1.

Sobel, A. H., 2002: Water vapor as an active scalar in tropical atmospheric dynamics. *Chaos: An Interdisciplinary Journal of Nonlinear Science*, **12**, 451–459, https://doi.org/10.1063/1.1480795.

——, and C. S. Bretherton, 2000: Modeling Tropical Precipitation in a Single Column. *Journal of Climate*, **13**, 4378–4392, https://doi.org/10.1175/1520-0442(2000)013<4378:MTPIAS>2.0.CO;2.

——, and ——, 2003: Large-scale waves interacting with deep convection in idealized mesoscale model simulations. **55**, 45, https://doi.org/10.3402/tellusa.v55i1.12084.

——, J. Nilsson, and L. M. Polvani, 2001: The Weak Temperature Gradient Approximation and Balanced Tropical Moisture Waves. *Journal of the Atmospheric Sciences*, **58**, 3650–3665, https://doi.org/10.1175/1520-0469(2001)058<3650:TWTGAA>2.0.CO;2.

Stahle, D. W., and M. K. Cleaveland, 1992: Reconstruction and Analysis of Spring Rainfall over the Southeastern U.S. for the Past 1000 Years. *Bull. Amer. Meteor. Soc.*, **73**, 1947–1961, https://doi.org/10.1175/1520-0477(1992)073<1947:RAAOSR>2.0.CO;2.

Takaya, K., and H. Nakamura, 1997: A formulation of a wave-activity flux for stationary Rossby waves on a zonally varying basic flow. *Geophysical Research Letters*, **24**, 2985–2988, https://doi.org/10.1029/97GL03094.

——, and ——, 2001: A Formulation of a Phase-Independent Wave-Activity Flux for Stationary and Migratory Quasigeostrophic Eddies on a Zonally Varying Basic Flow. *Journal of the Atmospheric Sciences*, **58**, 608–627, https://doi.org/10.1175/1520-0469(2001)058<0608:AFOAPI>2.0.CO;2.

Thomas, T. M., G. Bala, and V. V. Srinivas, 2021: Characteristics of the monsoon low pressure systems in the Indian subcontinent and the associated extreme precipitation events. *Clim Dyn*, **56**, 1859–1878, https://doi.org/10.1007/s00382-020-05562-2.

——, ——, and S. V. Vemavarapu, 2022: CESM simulation of monsoon low pressure systems over India. *International Journal of Climatology*, **42**, 5964–5984, https://doi.org/10.1002/joc.7571.

Wang, B., and Coauthors, 2021: Monsoons Climate Change Assessment. *Bulletin of the American Meteorological Society*, **102**, E1–E19, https://doi.org/10.1175/BAMS-D-19-0335.1.

Wheeler, M., and G. N. Kiladis, 1999: Convectively Coupled Equatorial Waves: Analysis of Clouds and Temperature in the Wavenumber–Frequency Domain. *J. Atmos. Sci.*, **56**, 374–399, https://doi.org/10.1175/1520-0469(1999)056<0374:CCEWAO>2.0.CO;2.

——, ——, and P. J. Webster, 2000: Large-Scale Dynamical Fields Associated with Convectively Coupled Equatorial Waves. *Journal of the Atmospheric Sciences*, **57**, 613–640, https://doi.org/10.1175/1520-0469(2000)057<0613:LSDFAW>2.0.CO;2.

Wills, R. C. J., R. H. White, and X. J. Levine, 2019: Northern Hemisphere Stationary Waves in a Changing Climate. *Curr Clim Change Rep*, **5**, 372–389, https://doi.org/10.1007/s40641-019-00147-6.

Wirth, V., M. Riemer, E. K. M. Chang, and O. Martius, 2018: Rossby Wave Packets on the Midlatitude Waveguide—A Review. *Mon. Wea. Rev.*, **146**, 1965–2001, https://doi.org/10.1175/MWR-D-16-0483.1.

Wolding, B. O., E. D. Maloney, and M. Branson, 2016: Vertically resolved weak temperature gradient analysis of the Madden-Julian Oscillation in SP-CESM. *Journal of Advances in Modeling Earth Systems*, **8**, 1586–1619, https://doi.org/10.1002/2016MS000724.

Yanai, M., S. Esbensen, and J.-H. Chu, 1973: Determination of Bulk Properties of Tropical Cloud Clusters from Large-Scale Heat and Moisture Budgets. *Journal of Atmospheric Sciences*, **30**, 611–627, https://doi.org/10.1175/1520-0469(1973)030<0611:DOBPOT>2.0.CO;2.

Yasunaga, K., S. Yokoi, K. Inoue, and B. E. Mapes, 2019: Space–Time Spectral Analysis of the Moist Static Energy Budget Equation. *Journal of Climate*, **32**, 501–529, https://doi.org/10.1175/JCLI-D-18-0334.1.

Yoon, J.-H., and T.-C. Chen, 2005: Water vapor budget of the Indian monsoon depression. *Tellus A: Dynamic Meteorology and Oceanography*, **57**, 770–782, https://doi.org/10.3402/tellusa.v57i5.14737.

——, and W.-R. Huang, 2012: Indian Monsoon Depression: Climatology and Variability.

You, Q., and Coauthors, 2022: Recent frontiers of climate changes in East Asia at global warming of 1.5°C and 2°C. *npj Clim Atmos Sci*, **5**, 1–17, https://doi.org/10.1038/s41612-022-00303-0.

Yu, J.-Y., and J. D. Neelin, 1994: Modes of Tropical Variability under Convective Adjustment and the Madden–Julian Oscillation. Part II: Numerical Results. *Journal of the Atmospheric Sciences*, **51**, 1895–1914, https://doi.org/10.1175/1520-0469(1994)051<1895:MOTVUC>2.0.CO;2.

Zhu, J., and X.-Z. Liang, 2012: Impacts of the Bermuda High on Regional Climate and Ozone over the United States. *J. Climate*, **26**, 1018–1032, https://doi.org/10.1175/JCLI-D-12-00168.1.

Zishka, K. M., and P. J. Smith, 1980: The Climatology of Cyclones and Anticyclones over North America and Surrounding Ocean Environs for January and July, 1950–77. *Mon. Wea. Rev.*, **108**, 387–401, https://doi.org/10.1175/1520-0493(1980)108<0387:TCOCAA>2.0.CO;2.